In-Situ Monitoring of Reactive Ion Etching Using a Surface Micromachined Integrated Resonant Sensor

A Ph.D. Thesis

By

Bryan George Oneal Morris

Submitted to the Ph.D. Thesis Examination Committee in
Partial Fulfillment of the Requirement for the
Degree of Doctor of Philosophy in Electrical Engineering

Georgia Institute of Technology
School of Electrical and Computer Engineering
Atlanta, GA 30332

December 2009

TABLE OF CONTENTS

ACKNOWLEDGEMENT

I thank God for his love and his presence in my life. He allowed me to experience this valuable learning opportunity and complete this thesis.

For his patience, encouragement and support to my advisor Dr. Gary May I give both my gratitude and my respect. I am indebted to many of my former professors and colleagues who directly or indirectly helped me. I wish to thank Dr. Hasler for his ideas and advice. In addition I am thankful to Dr. Brand, Dr. Kohl and Dr. Shamma, the other members of my dissertation committee, for their time and effort spent in reviewing this thesis.

I wish to express my appreciation to the NSF-IGERT and Applied Materials Fellowship Foundations. I am grateful for the assistance of the Steve Chaddick Chair for helping to fund and facilitate this research. This work would have never been completed had it not been for the guidance of many people at different stages in the process. A special thanks to Paul Joseph for all our discussions and his help with processing. I am thankfully to the staff of the MIRC cleanroom, for the use of the facilities, especially to Vinh Nguyen and Gary Spinner, for access to the PlasmaTherm SLR RIE to ultimately realize and test the operation of the RIE sensor.

Finally, I wish to thank my family for their love and support, and for their motivation and prayers.

LIST OF TABLES

LIST OF FIGURES

SUMMARY

This research explores a novel *in-situ* technique for monitoring film thickness in the reactive etching process that incorporates a micromachined sensor. The sensor correlates film thickness with changes in resonant frequency that occurs in the micromachined platform during etching. The sensor consists of a platform that is suspended over drive and sense electrodes on the surface of the substrate. As material is etched from the platform, its resonant vibrational frequency shifts by an amount that is proportional to the amount of material etched, allowing etch rate to be inferred.

This RIE monitoring methodology exploits the accuracy of resonant micromechanical structures, whereby shifts in the fundamental resonant frequency measure a physical parameter. A majority of these systems require free-standing mechanical movement and utilize a sacrificial layer process as the key technique to develop and release the structure on a substrate. A sacrificial layer technique that incorporates a low temperature sacrificial polymer was utilized to develop and release the suspended RIE sensor with excellent performance and is capable of fabricating other low cost, high performance and reliable suspended MEMS devices.

The integration of sensors and electronic circuitry is a dominant trend in the semiconductor industry, and much work and research has been devoted to this effort. The RIE sensor relies on capacitive transduction to detect small capacitance changes and the resulting change in resonant frequency during the RIE process. The RIE sensor's overall performance is limited by the interface circuit, and integration with the proper circuit allows the RIE sensor to function as a highly sensitive measure of etch rate during the RIE process. A capacitive

feedback charge amplifier interface circuit, when configured with the RIE senor at the input achieves very low noise sensing of capacitance changes and offers the potential for wide dynamic range and high sensitivity. As an application vehicle, process control was demonstrated in the PlasmaTherm SLR series RIE system located in the Georgia Tech Microelectronics Research Center.

The integration of the RIE sensor with the charge amplifier interface circuitry provides an accurate cost effective alternative to direct in-situ measurements of substrate conditions, and is expected to further facilitate more sophisticated RIE process monitoring instrumentation subsystems.

CHAPTER 1

1.1 INTRODUCTION

State-of-the-art integrated circuits currently employ upwards of 60 million transistors, six layers of metal, and operate at clock frequencies over 1 GHz. As device dimensions continue to shrink and the speed of computing and communications systems increases, the effect of fluctuations in the manufacturing process becomes critical. Achieving tight specifications, given the continuing trend toward even further miniaturization, represents a major challenge in process control, an issue of critical importance to the semiconductor industry [1].

Semiconductor fabrication consists of hundreds of processing steps, including cleaning routines, oxidation, diffusion, photolithography, etching and deposition. Process steps are typically performed in sequence, and yield loss may occur at every step. Maintaining product quality requires the control of thousands of variables and requires not only advances in device fabrication process, but also advances in process monitoring and control. Improved process monitoring and control method ensures device manufacturability, minimizes parameter deviations and increases yields. Monitoring process variables from pre- and post-process measurements as well as real time measurements enable the process to remain “centered” within the desired manufacturing tolerance [2–4].

1.2 SEMICONDUCTOR PROCESS CONTROL

Traditionally, control of semiconductor processes has been addressed in an aggregate manner by statistical process control (SPC) techniques [5]. SPC is performed off-line and measurements are obtained after several batches of wafers are processed. SPC relies on *ex-situ* measurements and information on the status of the wafer and the equipment. This introduces a delay in determining whether out of tolerance condition exists and the corrective measurements that should be initiated. The delay inherent in SPC and the lack of on-line sensing and closed-loop corrective action in this approach allows a large volume of defective materials to be processed before they are detected, resulting in significant waste and low yield [6].

1.2.1 *In-situ* Process Control

It has been reported that device requirements in fabrication processes are forcing the transition to *in-situ* sensing and real time process control protocols. There is an ever-increasing restriction on material property specifications that are permissible in the different component of thin films, being used to build ultra large scale integrated (USLI) devices [7–8]. As device geometries continue to shrink, the window on allowable process variations for producing materials with acceptable electrical properties gets even smaller. This requires that all fabrication processes - and especially the etch processes used to form and pattern thin films - adopt even more restrictive process control limits. The required degree of control for device fabrication can only be achieved by using *in-situ* sensing to provide data for real-time feedback control [2–7].

It is anticipated that in the future, there will be an increase in the level of chemical

complexity of the thin film processes used in device fabrication. This is partly due to new technology demands, changes in the basic material used in the construction of advanced devices, and the use of novel poly- and organic chemicals and materials. These types of material will undoubtedly have rich gas phase chemistries that will influence both the process and the film's material properties, requiring even tighter control during the device fabrication process. Ultimately many processes will be forced to migrate towards much higher-pressures or plasma-enhanced reaction protocols to achieve production quality devices. It is believed that acceptable yields in device fabrication, when using these complex materials, will only be achieved with improved understanding of the plasma chemistries, while employing advanced monitoring and controlling approaches for the depositions and etching processes [2–7].

1.2.2 Advanced Process Control

Advanced process control (APC), particularly trends from offline to inline to *in-situ* techniques enables a richer more powerful spectrum of process control strategies [8]. Advances in APC have been driven primarily by successes in run-to-run (R2R) control and in fault detection and classification (FDC). APC has demonstrated major value to the semiconductor industry and has been adopted by most manufacturers, to some extent, since its introduction into the 1994 International Technology Roadmap for Semiconductors [4–7].

Sensors and associated metrology to support APC are available today for key process areas such as chemical mechanical planarization (CMP), chemical vapor deposition (CVD) and lithography [9–10]. A comprehensive APC manufacturing strategy is not yet a reality, nor is a portfolio of sensors and metrology tools to support complete factory-wide deployment, given the

changes in materials, processes, and device structures expected for future technology needs. The benefits already realized from APC are driving development of new sensor technologies and associated control software, which will allow comprehensive solutions to be realized in the near future [4–8].

APC comprises two different areas. The first involves course corrections aimed at adjustments of process parameters in order to compensate for systematic drifts in equipment and process behavior. In this instance, inline metrology is employed for feedback or feed-forward control, either on a wafer-to-wafer or batch-to batch basis to maintain product quality in the presence of process variation and to reduce waste. Real time control, based on in situ and real time sensors during the process requires further development of more process specific sensors with sufficient metrology precision. Fault management, the second APC area, is directed at rapid identification and response to equipment problems. *In-situ* and real-time sensors are used to identify common equipment faults, initiate repairs and reduce product scrap [10,11]. Additional benefit is envisioned as sensor and metrology data are combined with information, enabling more sophisticated classification of more subtle fault sources, along with fault prognosis and maintenance rescheduling consisting with overall tool and factory efficiency. Building on the confidence for R2R and FDC, while incorporating real time control, is an ongoing challenge for the industry.

Today, integrated metrology is prevalent only in CMP (film thickness), but it is beginning to appear in etch and lithography processes. In-line metrology will improve throughput, reduce cycle time, allow for increased sampling (number of wafer as well as points per wafer), and reduce control feed forward and feedback lag times. Difficult challenges must be overcome before integrated metrology is accepted on a large scale. These challenges are in the

areas of: 1) performance and cost metrics for integrated metrology, which must be comparable for stand-alone metrology; 2) impact on tool throughput, which should approach zero; 3) integration; 4) data management; 5) setup (including calibration and training) and configuration time and management; 6) cost and difficulty of impact on tool up-time, and 7) accuracy equivalence with stand alone metrology [7–11].

1.3 *IN-SITU* SENSOR TECHNOLOGY

Real-time *in-situ* sensors, if quantitative and precise, will add to the capability for real-time course correction that compensates for short-term, random process variability. This will also enable a true real-time APC, in which in situ sensors and real-time response drive both course correction and fault detection at the tool level, tightening unit process variability and enhancing run-to-run control [5, 10].

In-situ sensors technology remains far from complete. A group of sensors based on optical, chemical, and electrical signals from processes are available, but their development and demonstration as quantitative metrology techniques for course correction has been limited. *In-situ* sensors that measure across-wafer uniformity and vertical profiles are necessary. *In- situ* sensors where possible, should be accompanied by equipment designs that enable control action that directly compensate for non-uniformities. While *in-situ* real time sensors are broadly deployed for detection and response to key failure modes, they have yet to be coordinated and integrated to enable causal identification of more subtle failure modes. This is an important challenge given the economic consequences of downtime for preventive or emergency equipment maintenance.

In-situ sensors face additional challenges in the wealth of complex materials, processes, and device structures anticipated for future technology nodes. Measuring the composition, thickness, and uniformity of ultrathin gate dielectrics or metallic barrier layers presents a significant challenge, even with the adoption of atomic layer deposition (ALP). Nanoporous low-κ materials, particularly their interfaces with barrier layers, present an equal challenge for in situ sensors. In-situ chemical identification is increasingly critical where surface chemistry plays a key role in product quality.

1.4 *IN-SITU* PLASMA SENSORS

Semiconductor manufacturers rely on process control methods and analysis of tool sensor outputs to improve yields, increase tool productivity, and reduce manufacturing costs. The behavior of process tool, specifically plasma etch tools, is difficult to control because small variations in the equipment and process setup can have an unpredictable impact on the etch quality. The quality of the etch process is driven by the condition of the plasma and many parameters have a small margin of deviation before yields decline.

Sensor based technologies for real-time monitoring and detection of the RIE etching process are being explored. Challenges exist for real-time sensing systems, given the wealth of data provided by RIE plasma etch tools, and because the output signals change continuously during the etch process. Real-time sensing systems are typically sensitive to secondary variables such as temperature, in addition to the primary parameter for which the sensor was intended. Since virtually all such parameters is eventually processed by computer, the final sensor output signal, ideally, should be in a digital format, so that any secondary-variable sensitivity (e.g., to

temperature) is eliminated along with any nonlinearity problems. Finally, there should be some way of checking the sensor in its operating system to see if the device is still giving correct data (the device should be self-testing over at least a portion of its operating range). Controlling critical plasma etching process and plasma equipment on the basis of devices that are not testable is clearly undesirable. Thus, a well developed, accurate noninvasive plasma sensor and its interface circuitry performs an essential role in any complete real-time sensing system.

A novel, nonintrusive plasma impedance sensor was reported, that measures the fundamental and harmonic voltage and phase of the radio-frequency power in the plasma chamber [17]. The data acquired from the sensor provides information that can be used for process control. A real-time controller checks the data against a fault library, and adjusts the plasma index based on the variations. In general, when a fault is detected, it is not necessarily the parameter control device but the chamber system that is determined to be the source of the problem. This sensor is reportedly immune to drifts and deterioration in the sensor parameters caused by plasma chamber environment.

The specialized nature of the different types of plasma sensors under development, and complexity of *in-situ* plasma process control makes cost-effective development and fabrication an issue for low to moderate volume application. High reliability and stability in the real operating environment are critical requirements for these types of sensors, and questions of cost, reliability, and performance go beyond the basic sensor element itself. These requirements are difficult to achieve and continued development is required for many of these applications and sensors.

1.5 INTEGRATED SENSORS

The integration of sensors with electronic interface circuitry, into more sophisticated instrumentation subsystem, is very important and an increasing trend. However, the advantages of integrating the sensors as part of a smart sensing module containing additional electronics makes sense only if it buys increased system performance. Therefore, the sensor must be considered as a system element in order to justify making it smart. The integrated "smart" sensors can provide compensation, linearization, two-way communication and other functions.

Integrated sensors typically produce outputs extending down to the microvolt range, and can resolve changes in resistance or capacitance of milliohms or femtofarads, or less. From a systems point of view, it is preferable to deal with signals in the range of tenths of volts to volts, which are robust in the face of environmental factors such as humidity and electromagnetic noise. The need for amplification and multiplexing with sensors is the current principal driver of sensor-circuit integration, and such circuitry has been added either in monolithic or hybrid form to a great many devices. Sensor readout itself is also becoming an important research focus, with traditional difference amplifiers, capacitive oscillators, and switched-capacitor integrators being joined with efforts involving force-balanced feedback schemes or the use of tunneling or atomic force feedback to detect microstructure motion with extreme sensitivity.

Thus, the interface circuitry performs an essential role in any complete system. However, the technology levels needed to focus on sensor-circuit integration are clearly very high. New integration schemes give rise to new applications and productive solutions. The possible future advances will further the development of real time integrated sensors for controlling critical semiconductor processes and equipment. Applications related to plasma etch community include high-k dielectric and source-drain etch endpoint detection, process gas purity monitoring, radical

density measurements in the plasma chamber and emission monitoring. Beyond that, the emergence of micro-actuators "instruments on a chip" promises the ability to exert significant measures of control and information gathering.

1.6 THESIS ORGANIZATION

This thesis deals with the design, fabrication and realization of an integrated resonant sensor for *in-situ* monitoring of the RIE process. Due to the large number of RIE etch rate monitoring principles and techniques, an overview of this area is presented in Chapter 2. Chapter 3 discusses surface micromachining technology which is the key technology to achieving the sensor being developed for the *in-situ* RIE process monitoring application. The second part of this chapter focuses on the mechanical and electrical behavior of the resonant RIE sensor structure. The RIE sensor's overall performance is limited by the interface circuit, and integration with the proper circuit allows the RIE sensor to function as a highly sensitive measure of etch rate during the RIE process. This building block for the capacitive feedback charge amplifier interface circuit is discussed in Chapter 4. In Chapter 5 finite element simulations are introduced in order to verify the RIE sensor design and theoretical model presented in Chapter 3. Chapter 6 focuses on the fabrication process of the RIE sensor which is a structured sequence of thin film deposition, photolithography, and selectively etching using surface machined techniques. The performance analysis and electrical measurement of the RIE sensor is presented in Chapter 7. This work focuses on electrostatic excitation and capacitive detection of the RIE sensor and the measurement setup and results are presented in Chapter 8. Finally, the dissertation ends with suggestions for future work and conclusions.

CHAPTER 2

2.1 ETCH PROCESSES

To develop functional devices, structures or features (e.g., gates, interconnects, and vias) on the wafer substrate, it is necessary to etch (i.e., selectively remove) materials using imaged photoresist as a masking template. The pattern can be etched directly into the substrate or into thin films previously deposited, which may be used as a mask for subsequent etches. For a successful etch, there must be sufficient selectivity (etch-rate ratio) between the material being etched and the masking material.

In general, there are two classes of etching processes: (1) wet etching, where the material is dissolved when immersed in a chemical solution; and (2) dry etching where the material is sputtered or dissolved using reactive ions or a vapor phase etchant. Distinctions are made on the basis of isotropy, etch medium, and selectivity of the etch to the other materials. Isotropic etchants etch uniformly in all directions, resulting in rounded cross-sectional features. By contrast, anisotropic etchants etch in some direction preferentially over others, resulting in trenches or cavities delineated by flat and well-defined surfaces (illustrated in Figure 2.1). The etch medium (wet versus dry) plays a role in selecting a suitable etch method.

2.1.1 Wet Etching

Wet etching in aqueous solutions is the simpler technology and offers the advantage of low-cost batch fabrication (e.g., 25 to 50 *100-nm* wafers etched simultaneously) and can be either of the isotropic or anisotropic type. Wet etching works very well for etching thin films on substrates, and can also be used to etch the substrate itself.

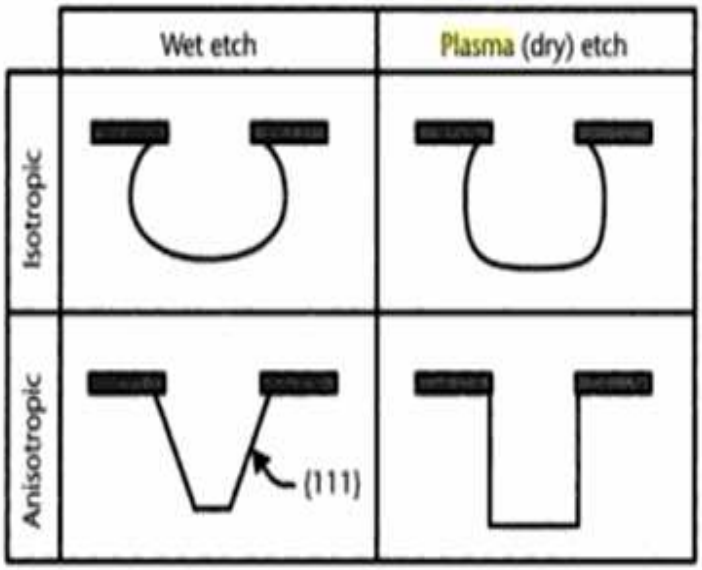

Figure 2.1: Cross-sectional trench profiles resulting from different etch methods [18].

The most common group of silicon isotropic wet etchants is HNA, also known as *iso-etch* and *poly-etch*. This mixture of hydrofluoric (HF), nitric (HNO_3), and acetic (CH_3COOH) acids has been in use since the early days of integrated circuits. The etch rate vary from 0.1 to > 100-µm/min depending on the proportion of the acids in the mixture. Etch uniformity and undercutting of the mask layer is normally difficult to control but is improved by agitation during

etching.

Anisotropic wet etchants are known as orientation-dependent etchants (ODEs), because their etch rates depend on the crystallographic direction, allowing the etching to stop on certain crystal planes in the substrate. Anisotropic wet etching results in three-dimensional faceted structures formed by intersecting crystallographic planes (Figure 2.2).

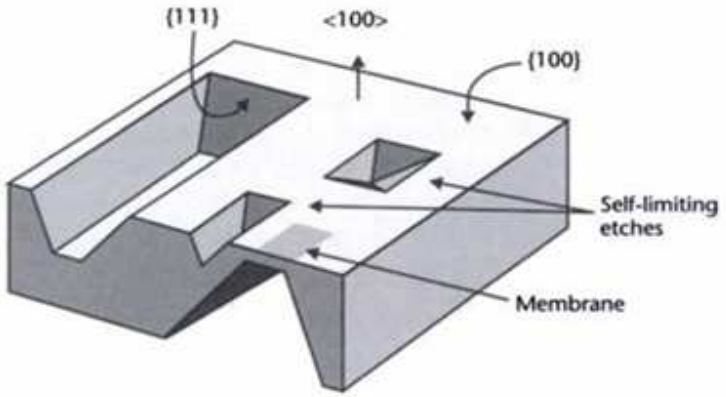

Figure 2.2: Anisotropic etching of cavities in (100)-oriented silicon [18].

Wet processing is commonly used to remove gold seed layers from MEMS and compound semiconductor devices. However, while wet processing can remove seed layers, it undercuts the plated gold line (possibly reducing its mechanical integrity), does not remove the layer uniformly, causes excessive loss of plated metal, raises environmental and safety issues related to the use of wet-etch chemistries, and is expensive. An alternative is to use EDP which is another selective wet etchant. EDP is extremely hazardous and its vapors are carcinogenic,

necessitating the use of completely enclosed processing facilities.

2.1.2 Electrochemical Etching

The relatively large etch rates of anisotropic wet etchants (> 0.5um/min) make it difficult to achieve uniform and controlled etch depths using timed etching. Some applications, such as bulk micromachined sensors, demand thin membranes with dimensional thickness and uniformity of better than 0.2 um. Thickness control can be obtained by using a precisely grown epitaxial layer and controlling the etch reaction with an externally applied electrical potential.

This method is referred to as electrochemical etching (ECE). An n-type epitaxial layer is grown on a p-type wafer forming a p-n junction diode that allows electrical conduction only if the p-type side is at a voltage above the n-type. During ECE, the applied potential is such that the p-n junction is reverse biased, and the p-type substrate is electrically floated, so it is etched. The etch reaction terminates when the p-type substrate is completely removed, leaving a layer of n-type material with precise thickness. In one example of a standard electrochemical process, sodium hydroxide reacts with the tungsten, etching the tungsten away. Precise etch relies on a fast electronic current shutoff device that senses when the etching process is complete [19].

2.1.3 Plasma Etching

Over the last several decades, plasma assisted “dry” etching has emerged as an indispensable tool for the manufacture of microelectronic circuits, replacing traditional wet chemistry for etching and pattern transfer. Plasma is a partially ionized gas mixture consisting

of ions, free radicals, neutral byproducts, and photons. There are two key mechanisms in plasma processing: a physical mechanism performed by ion bombardment and a chemical mechanism performed by free radicals and byproducts.

Plasma etching involves the generation of chemically reactive neutrals (e.g., F, Cl), and ions (e.g., SF_x^+) that are accelerated under the effect of an electric field towards the substrate. The reactive species (neutrals and ions) are formed by the collision of molecules in the reactant gas (e.g., SF_6, CF_4, Cl_2, NF_3).with electrons excited by the RF electric field. Plasma etching using various gas species, such as, CH_xF_y, is a relatively fast process, with etch rates on the order of 20 nm/min. When the etch process is purely chemical, powered by reactions of neutrals with the substrate, it is referred to as plasma etching. When ion bombardment of the wafer substrate plays a role in the chemical etch reaction, the process is then referred to as reactive ion etching (RIE).

In RIE, ion (e.g., SF_x^+) motion towards the substrate is nearly vertical, which gives RIE vertical anisotropy. Asymmetric electrodes and low chamber pressure ($5\ Pa$) are characteristic of RIE operation. Inductively coupled plasma reactive ion etching (ICP-RIE) provides greater excitation to the electron cloud by means of an externally applied RF electromagnetic field. Inductively coupled plasma (ICP) increases the density of ions and neutrals resulting in higher etch rates.

Vapor phase etching is another dry etching method, which utilizes less complex equipment required for RIE. The wafer to be etched is placed inside a chamber, in which one or more gases are introduced. The etched material is dissolved at the surface in a chemical reaction with the gas molecules. The two most common vapor phase etching technologies are silicon dioxide etching using hydrogen fluoride (HF) and silicon etching using xenon difluoride (XeF_2), both of which are isotropic in nature. Care must be taken in the design of a vapor phase process

to not have bi-products form in the chemical reaction that condense on the surface and interfere with the etching process.

Plasma-assisted “dry” etching, has allowed for the production of smaller and more complex devices, improved the capabilities of producing fine line geometries, enabled more devices per single chip, and is used in many technologies. It is most critical in ultra large scale integrated (ULSI) circuit fabrication and is used many times during the processing of a single wafer. Other areas that rely heavily on plasma-assisted etching include micro-electrical-mechanical (MEMS) structure fabrication, many so-called nano-science processes, micro-optical and photonic activities and numerous other material processing where near room temperature chemical reactions are required. Plasma “dry” etching is an enabling technology with clear advantages when compared to wet etching, with the exception of the expense associated with dry etching equipment and operation costs [18−19].

The remainder of this chapter focuses on RIE, the current methods for RIE monitoring and a novel in situ method of monitoring the RIE process using a micromachined MEMS device will be discussed in subsequent chapters.

2.2 REACTIVE ION ETCHING

Device specialization in the IC industry and increasing complexity of device integration to keep pace with Moore’s law are changing plasma etching. Applications are becoming more diverse and specific to each customer. The focus is now, more than ever, on a fundamental understanding of etch mechanisms and its application to process development. Each etch step has to be characterized not only by its etch characteristics like etch rate, profile, selectivity and

uniformity across wafer, but also by its fundamental properties such as sidewall passivation layer composition and thickness, chamber wall deposition composition, depth of the etch front mixing layer, microloading, macroloading and final line edge roughness generated by the sequence of process steps. A better understanding of the underlying etch mechanisms allows one to choose the best opportunity for process optimization for any new structure.

RIE has emerged as a critical process step in production of integrated circuits. RIE offers high etch directionality, enabling accurate pattern transfer not obtainable with wet etching. The physical and chemical mechanisms involved in RIE are complex due to the nature of the physics and chemistry of plasma environment. As an example, consider the chemical reactions that occur when SiO_2 is etched in chloroform plasma [20]:

$$4CF_3 + 3SiO \rightarrow 2CO + 2CO_2 + 3SiF_4$$
$$2CF_3 + SiO_2 \rightarrow CO + COF_2 + SiF_4$$
$$2CF_3 + 3SiO_2 \rightarrow O_2 + 2CO_2 + 3SiF_2$$
$$2CF_3 + 2SiO_2 \rightarrow COF_2 + CO + O_2 + 2SiF_2$$
$$2CHF_3 + SiO_2 \rightarrow 2CO + H_2 + SiF_4$$
$$2CF_2 + SiO_2 \rightarrow 2CO + SiF_4$$

The quality of the etch is characterized by its etch rate, anisotropy, selectivity and uniformity. Etch rate is the quantity of material removed from the substrate per unit time/ Selectivity is a relative measure of the etching rates of the plasma. Anisotropy is the ability to etch vertically while minimizing horizontal etching and etch undercut. Uniformity implies a constant etch rate across the wafer surface and is an important parameter for single wafer processors. As devices approach the 65- and 45-nm design rules, maintaining good etch selectivity between Si, SiO_2, Si_3N_4 and other films will become increasingly critical to the

integrity of the finished product.

Etching certain films, such as silicon nitride (Si_3N_4) films on semiconductor wafers is and will continue to be an essential part of microelectronics manufacturing for the foreseeable future. The properties of Si_3N_4 are desirable for a variety of well- known reasons, including its ease of deposition, etch-masking properties, and stability. The stability of Si_3N_4 films allows the material to be used for such elements as gate spacers, etch and CMP stops, antireflective coatings, barriers, and hard masks [21−23].

RIE is a proven method for Si_3N_4 etching in addition to popular wet etching. Using gas species such as CH_xF_y produce etch rates on the order of 20 nm/min. RIE has the advantage of isotropy (it produces nearly vertical etch profiles). However, the selectivity is generally inferior to that of wet etching [21−23]. The RIE process generally creates a passivation polymer to reduce lateral etching, which requires a wet clean to remove the polymer. The high energies of RIE plasma etching can increase local temperatures, consuming thermal budget, and cause device damage from the impact of high-energy particles or charging [24−26].

A special subclass of RIE which continues to grow rapidly in popularity is deep RIE (DRIE). DRIE evolved in the 1990s from the need for an etch process capable of vertically etching high-aspect-ratio trenches at rates larger than the 0.1 to 0.5 $\mu m/mn$ typical of traditional plasma and RIE etchers. In this process, etch depths of hundreds of microns can be achieved with almost vertical sidewalls. The primary technology is based on the so-called "Bosch process", named after the German company Robert Bosch which filed the original patent, where two different gas compositions are alternated in the reactor. The first gas composition creates a polymer on the surface of the substrate, and the second gas composition etches the substrate (see Figure 2.3).

The etch step has both vertical and isotropic character, resulting in a slight mask undercut, as a result, etching aspect ratios of $50\ to\ 1$ can be achieved. The process can easily be used to etch completely through a silicon substrate, and etch rates are 3-4 times higher than wet etching. A limitation of DRIE is the dependence of the etch rates on the aspect ratio (ratio of height to width) of the trenches. The effect is known as lag or aspect-ratio-dependent etching (ARDE). Process development is required for each mask pattern and depth to optimize for low ARDE [18].

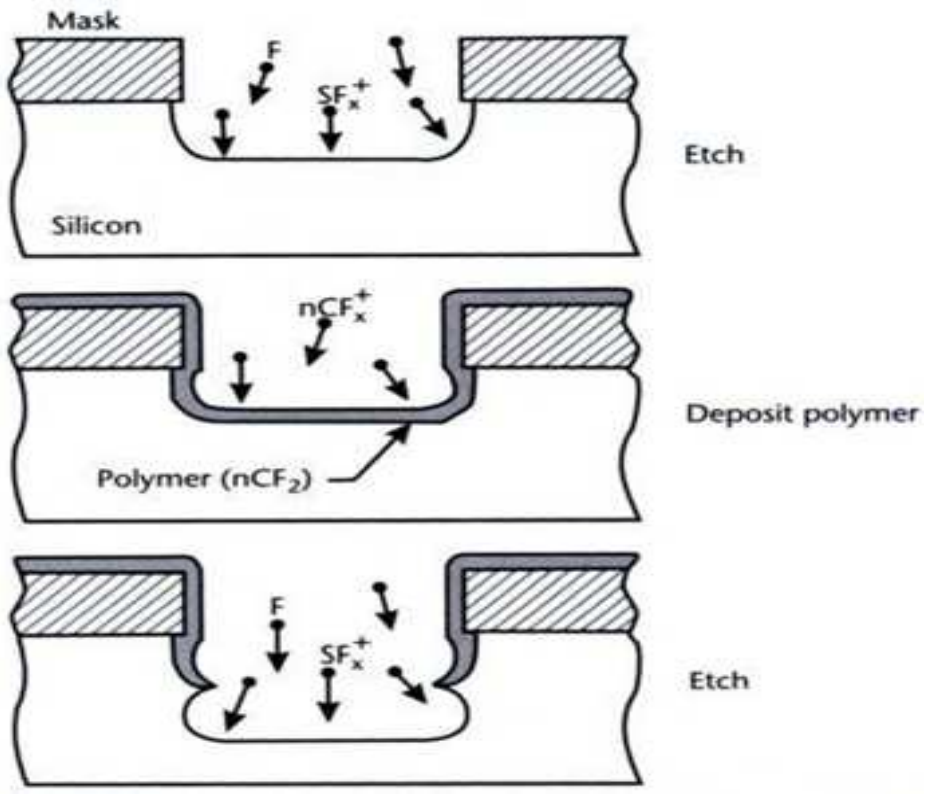

Figure 2.3: Profile of a DRIE trench using the Bosch process [18].

Bosch deep silicon etching is widely used on inductive coupled plasma equipment. Most inductive plasma sources in the field consist of a coil of one or several turns wound around a dielectric vessel, which is powered by radio frequency to generate a high density plasma. A major drawback of this kind of plasma source is its limited uniformity, which lowers the yield in critical MEMS applications.

With RIE, the plasma is generated by the application of a RF power source across two electrodes (Figure 2.4) separated in a reactive, gaseous chemical mixture of electrons, ions, and free radicals which produce the distinct plasma glow. Initially, the plasma consists of an equal number of positive and negative charges. Depletion of the charges in the plasma due to diffusion results in a layer of surface charge at the boundary of the plasma. Positive ions are accelerated within the chamber environment and aid in the etching process. The ion bombardment energy is controlled by the plasma potential. This quantity is difficult to monitor and quantify. Instead, the DC potential of the electrodes is measured.

The wafer substrate on the lower electrode is exposed to the reactive neutrals and charge species. These species combine with the substrate material and create volatile products that etch the wafer. Since electrons are more mobile that ions, a DC self bias voltage develops across the electrodes during the etch process to achieve the necessary current continuity. The self bias voltage accelerates ions towards the wafer surface where they are react, cause various compounds to be desorbed, aid in the formation of polymers and help to facilitate the anisotropic etching. Etching can be attributed to two distinct mechanisms: chemical etching cause by free radicals and physical etching cause by ion bombardment.

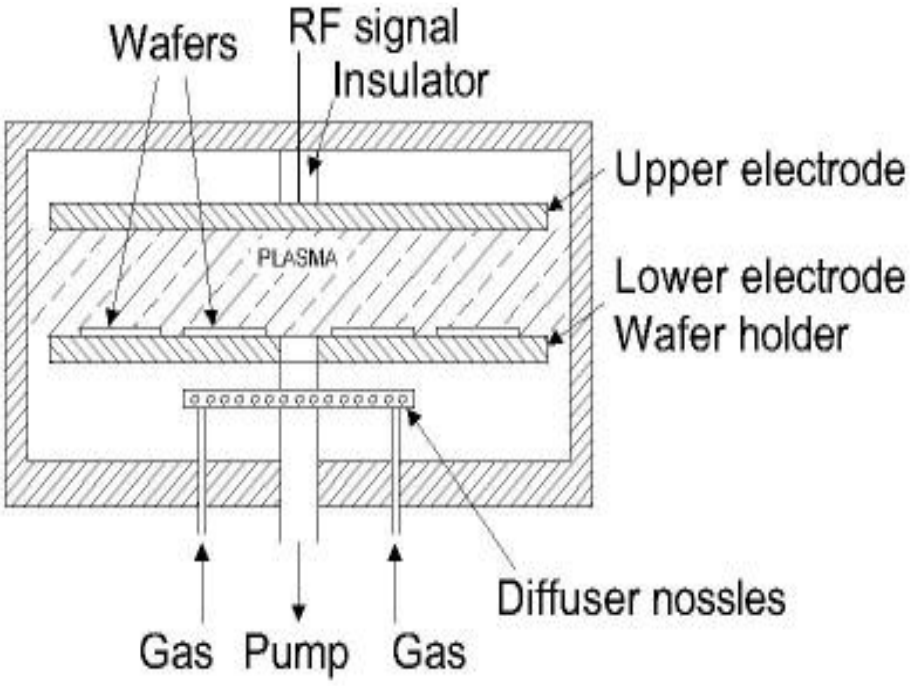

Figure 2.4: Typical parallel-plate reactive ion etching system.

Despite its widespread use in the semiconductor manufacturing industry, process control techniques for RIE are inhibited by the inadequacy of existing process sensor technology. Although real-time monitoring techniques exist for the regulation of process conditions such as gas flow, RF power, and chamber pressure, extant process monitoring methods are unable to provide direct, real-time measurements of the actual wafer state during the etch [27–30].

2.3 RIE PROCESS CONTROL

Real-time process monitoring and diagnosis of RIE is essential for process control. Ideally, semiconductor manufacturers would like to monitor the RIE process *in-situ* ad use process control methods and tool sensor analysis to control outputs such as etch rate, uniformity, and anisotropy directly. These parameters are crucial to the fabrication process because they can be directly correlated with process yield. In addition process monitoring increases tool productivity and reduce manufacturing costs.

The behavior of RIE plasma etch tools is difficult to control because small variations in equipment and process setup can have an unpredictable impact on etch quality. Many parameters have a very small margin of deviation (<1%) before yields decline. Historically, methods to control etch processes have relied on end-of-line metrology and short-loop test wafers. While these methods have been used to detect process chamber faults, they are slow and sometimes provide an unrealistic picture of etch chamber behavior [20–32]. Determining the root cause of chamber faults has relied on engineer experience and interpretations of tool data—clearly not the most efficient way to detect and remedy tool faults.

Given the wealth of data provided by RIE plasma etch tools, more-sophisticated methods for process control are needed. However, a complete array of *in-situ* technologies to measure the plasma etch parameters is not available. Conventional techniques for RIE process monitoring are typically performed off-line through pre- and post-process measurements. The techniques may be characterized as either direct, implying that film measurements are made on the wafer surface; or indirect, implying that measurements are determined from the plasma properties or process environment.

2.4 EXISTING METHODS OF RIE MONITORING

Among the few existing in-situ monitoring techniques are optical emission spectroscopy (OES), residual gas analysis (RGA), and interferometry. More recently acoustic composition measurements and ellipsometry techniques have been explored. The following is a review of existing methods and emerging techniques for RIE monitoring and control.

2.4.1 Optical Emission Spectroscopy

Optical emission spectroscopy (OES) has been established as a powerful and versatile method for *in-situ* monitoring and endpoint detection in plasma etching. OES is based on monitoring the light emitted from the plasma during the wafer processing and is used to gain information about the state of the tool and the process. It exploits the fact that the excited plasma emits light at discrete wavelengths, which are characteristic of the chemical species present in the plasma. The intensity of light at a particular wavelength is generally proportional to both the concentration of the associated chemical species and the degree of plasma excitation [31−35].

An OES system consist of a viewport to the plasma chamber, an optical coupling system, an optical detector incorporating some means of isolating the wavelengths of interest, and a computer or processor to acquire and analyze the spectral image. The viewport is either a window in the reactor or a direct optical feed-through into the chamber. The OES requires a direct view of the position of the plasma immediately above the wafer, but not the wafer itself, so the placement of the viewport can be restrictive. If ultraviolet wavelengths are to be monitored, the window must be of fused silica and not ordinary glass.

A number of OES sensor systems are commercially available and most plasma tool come

with their own on-board OES system. The typical configuration is shown in Figure 2.5. There are several types of optical detectors for OES systems. Simple systems use fixed bandpass filters for wavelength discrimination. The light that is passed by the filter is converted to an electrical signal either by a photodiode or by a photomultiplier tube (PMT). The advantages of these systems are low cost and high optical throughput. Disadvantages are the limited spectral information and mechanical complexity involved in changing the wavelength being monitored [30–35].

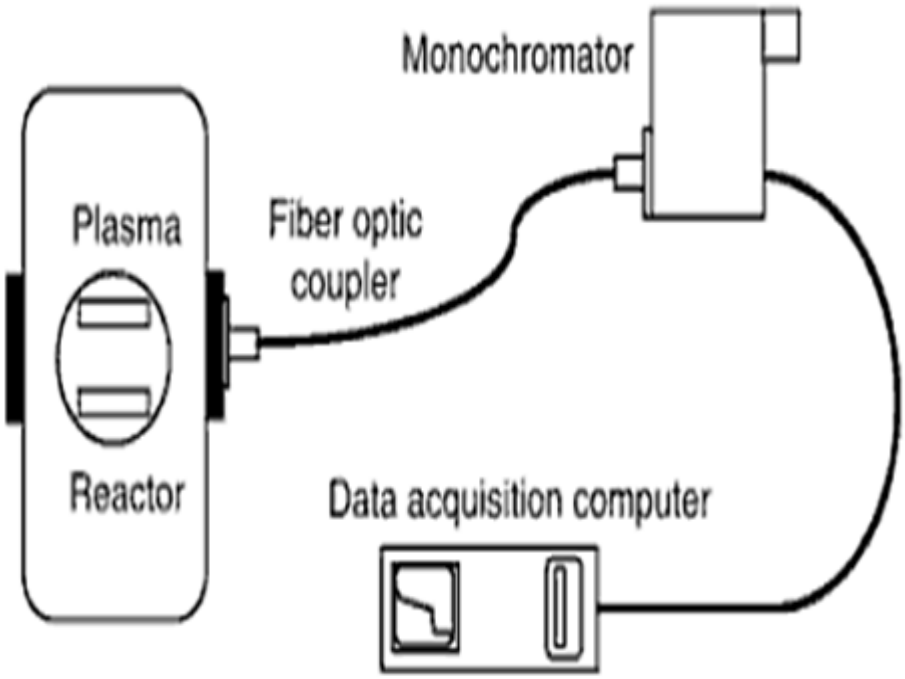

Figure 2.5: An optical emission spectroscopy sensor configuration.

More flexibility is afforded by OES systems that incorporate a monochromator. A monochromator consists of a narrow entrance slit, a diffraction grating, and an exit slit. Light falling on the grating is dispersed into a spectrum. The light is reimaged onto another slit, which provides wavelength discrimination. The throughput of a monochromator is much lower than that of a bandpass filter; hence PMTs are normally used for light detection in these systems. A variant of the monochromator is the spectrograph. It uses a fixed grating, and a solid state detector array instead of an exit slit and PMT. The advantage is that many wavelengths can be monitored at once. This is significant for situations where information has to be based on an entire spectral scan, not from only a single spectral peak [33 –35].

OES is a bulk measure of the optical radiation of the plasma species. Since emissions come from reactants and products, OES measurements are most often used to obtain the average optical intensity at a particular wavelength above the wafer. By setting an optical spectrometer to monitor the intensity at a wavelength associated with a particular reactant or by-product species, OES serves as an effective etch endpoint detector [30−34].

The fundamental principle behind endpoint detection is that the etch proceeds from one layer (the primary layer being etched) to the underlying layer (the substrate), the gas phase composition of the plasma changes. For example when etching *Ti/Al/TiN* stack on an oxide substrate with *Cl*-containing chemistry, there is significant decrease in the *Al* product species with a corresponding increase in the *Cl*-reactant species, as the etch transitions from the bulk Al to the *TiN* and oxide layers. Monitoring of the 261-nm *Al* emission line intensity will show a decrease during the time when the *Al* film disappears. Beside the endpoint indication, which is by far the most commonly generated information from this data, the slope of the endpoint signal (at the endpoint) can be used as an indicator of the nonuniformity of the etch process.

Despite its popularity and utility, the applicability of OES measurements for direct observation of wafer state and/or real-time control remains a challenge. This is because light generated by the plasma is rich in emissions from many species that cover a wide spectral range. For some etch chemistries, it is difficult to separate a characteristic line from the intensity background, evident from Figure 2.6. Nevertheless, there has been recent progress in using newer generation OES tools that have higher spectral resolution and higher sensitivity to estimate in situ wafer condition during etching [34–35].

2.4.2 Mass Spectroscopy/Residual Gas Analysis

In addition to the optical methods previously described, gases can also be analyzed by mass spectroscopy of the molecular species and their fragmented parts. The *in-situ* mass spectrometric sensor for gas analysis is commonly known as residual gas analyzer.

By far, the most widely used application of RGAs in semiconductor manufacturing is for maintenance and troubleshooting of process tools. RGAs are routinely used for leak checking, testing for gas contamination or moisture, and for tool qualification. In other applications, RGA are used to establish a correlation between the wafer quality and measure contamination in the process chamber. Recently, RGAs have been used for *in-situ* monitoring to reduce wafer-to-wafer variability. To be most effective, RGAs have to be able to directly monitor both tool baseline pressure and process chemistries in a nonintrusive way [36].

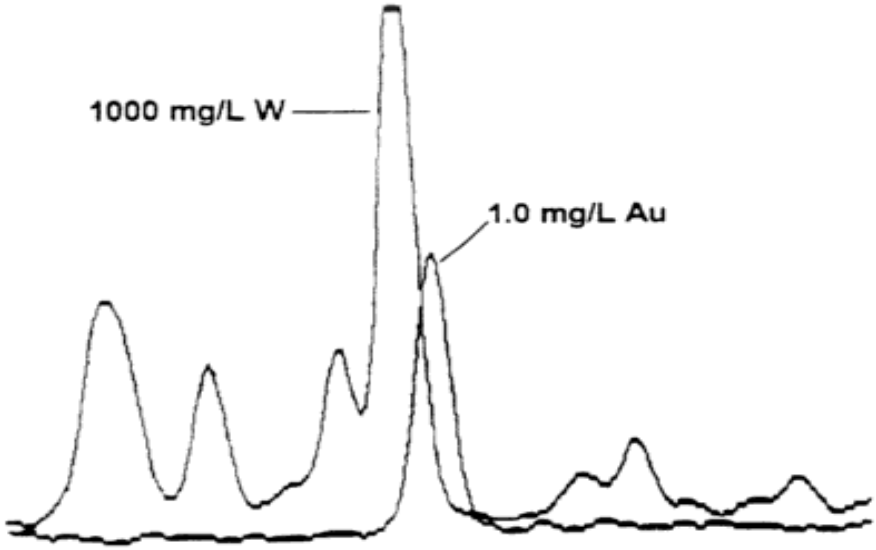

Figure 2.6: Complex emission wavelength identification [35].

Conventional RGAs operate by sampling the gases of interest through an orifice between the container for the gases (e.g., the RIE processing chamber or exhaust duct) and the residual gas analyzer (shown in Figure 2.7). In a conventional RGA, the pressure must be reduced below typical processing chamber pressures prior to ionization. This requires differential pumping and sampling of the process gases, making conventional RGAs a relatively bulky and expensive package [36]. The three basic component of a quadrupole mass spectrometer gas analyzer are the ionizer, the mass filter, and the detector.

During operation, beams of positive ions that have masses corresponding to the original molecules pass from the source to the mass analyzer where they are separated into the appropriate mass charge groups. This is achieved by the application of an electric or magnetic field or a combination of the two. These ions are then projected to a detector, or screen. Ideally,

the ions travel from the source to the detector without suffering any collision with any other ions or molecules. Determination of the gas constituents is based on the atomic mass of ions incident on the deflector. For example, a mass line at 1 and 16 would imply a chamber mixture of hydrogen and oxygen respectively.

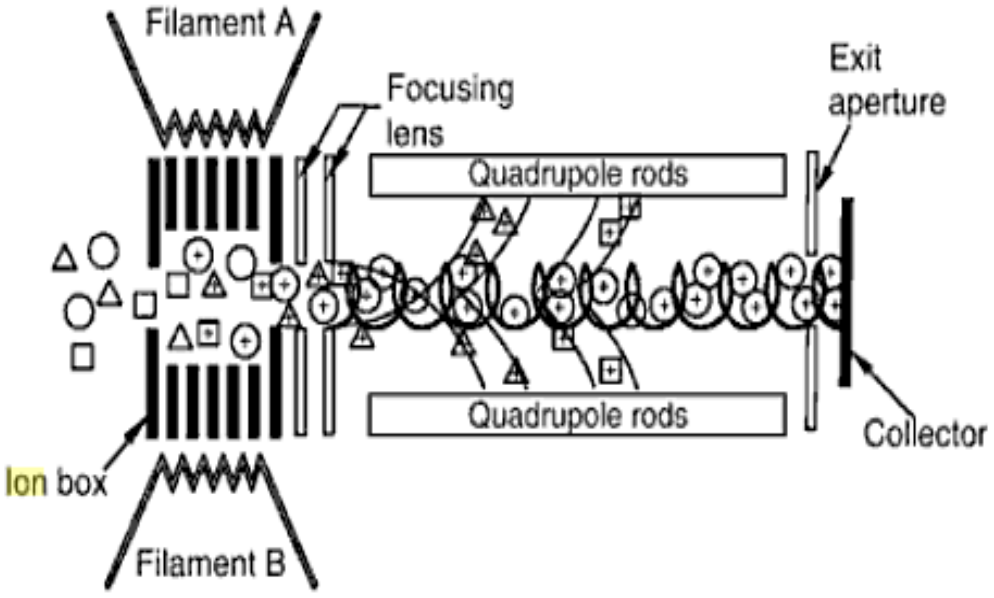

Figure 2.7: Quadrupole residual gas analyzer [37].

The RIE chamber is continuously depleted of gas; hence during the etch, the RIE chamber will consist of a mixture of process gases that results from the etch. Towards the end of the etch, the gas in the chamber will resemble its mixture prior to etching. By analyzing the residual gases it is possible to detect when the etch process is complete. As an *in-situ*

monitoring technique, RGA is considered indirect since it monitors process conditions that are related to the substrate etch [38–42].

Most RGAs function best when sensor elements are operated at pressures below $10^{-5}\ torr$, because this permits direct ionization of gases taken from the process chamber [37]. At high operating temperature, the RGA filament reacts strongly with the ambient process gases. This leads to different failure mechanism depending on the pressure and chemical nature of these gases. Certain types of filaments are volatile in oxidizing atmospheres (i.e., tungsten filament in oxygen), other volatile in reducing atmosphere (i.e., indium filament in hydrogen). Corrosive gases, such as chlorine and fluorine, reduce filament lifetime drastically.

Since both the process tool and the RGA are vacuum devices, the integrity of the pressure connections between the devices are critical. The source of the sensor should be in good pneumatic communication with the gases to be measured. Care must be taken to avoid condensation in the RGA of species from the process, which may require that the sensor and its mounting hardware be heated externally. Temperatures as high as 150°C are common. Additionally, quadrupole RGAs operate internally at very high RF voltages and therefore may radiate in the RIE process chamber or to the ambient outside the chamber. Higher temperatures may require separating the process system from the sensor, which may deteriorate the system performance and add to the cost [36–42].

Compared to other techniques used for in-situ monitoring, RGAs are very bulky and require a relatively large work space for mounting. Although new miniature RGA technologies have addressed the size issue, they are still difficult to mount and restrict access to the process chamber, and their small size imposes limits on their ability to separate species with different mass/charge ratios. RGAs generate large amount of 3D data (mass, pressure, time) in a very

short time. This data from RGAs and other equipment operating data are transmitted on command line by serial link, making efficient use of the data by the tool controller and viability as a truly integrated in-situ sensor a major challenge.

2.4.3 Ellipsometry

Ellipsometric measurement of film thickness is based on the change in polarization of light after reflection from a dielectric on the wafer surface. If the optical constant of the dielectric are known, the thickness can be determined using a model of the optical structure of the dielectric film on a silicon wafer. A brief discussion of elliptically polarized light and the phenomena of reflection and refraction facilitates the discussion of ellipsometry. In Figure 2.8, a beam of light is incident on a sample at some arbitrary angle of incidence, θ_i. At the boundary of the medium, part of the light will be reflected at angle θ_r while the other part will be transmitted through the sample at angle, θ_t. Snell's law requires that all three beams be in the plane of incidence. The plane of incidence is defined as that plane which contains the input beam, the output beam, and the direction normal to the sample surface.

The transmission and reflection measurements acquire the intensity ratios, T and R, respectively, over a given range of wavelengths. *T* and *R* are defined as the ratio of the light intensity being transmitted I_t or reflected I_r over the incident light intensity I_i on the sample, as shown in the following,

$$T = \frac{I_t}{I_i} \tag{2.1}$$

$$R = \frac{I_r}{I_i} \tag{2.2}$$

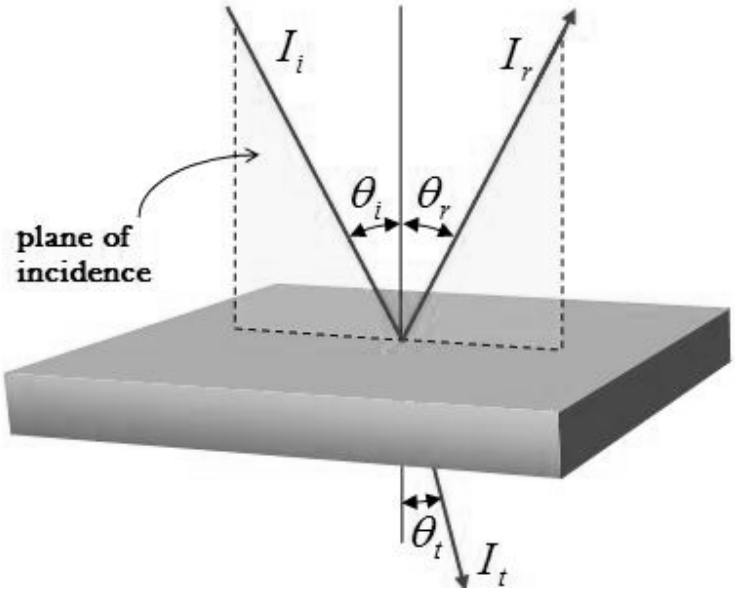

Figure 2.8: Incident, reflected, and transmitted light on the wafer surface.

Ellipsometry measures the change in polarization state of light reflected from the surface of a sample. The measured values are expressed as ψ and Δ. These values are related to the ratio of Fresnel reflection coefficients, R_p and R_s for p and s-polarized light, respectively,

$$\tan(\psi)\, e^{i\Delta} = \frac{R_p}{R_s} \tag{2.3}$$

Because ellipsometry measures the ratio of two values, it can be highly accurate and very reproducible. From Eq. (2.3), the ratio is seen to be a complex number. Thus it contains "phase"

information in Δ, which makes the measurement very sensitive.

Ellipsometric measurements are sensitive to the presence of thin films and to changes in their thickness. Measurements are highly accurate and reproducible (even in low light levels). No reference samples are needed, and the measurement is not susceptible to scatter, lamp or purge fluctuation. Additionally, the surfaces being measured may be immersed in any optically transparent medium. In microelectronics, ellipsometry has been established as a direct film thickness measurement method because it is non-destructive and non-invasive. Ellipsometry offers good resolution, increased sensitivity, especially to ultrathin films (<10nm), and provides two values at each wavelength (more information about sample) [44-45].

Ellipsometry is adaptable to both deposition and etch processing and has prospects for *in-situ* film thickness measurements. Although the principles of ellipsometry are well established, the technique was impractical for adaptive process control until the development of both fast acquisition techniques and inexpensive data processors.

Data acquisition (for ψ and Δ) versus wavelength and angle of incidence have been facilitated with the advent of fast inexpensive computers. To implement an adaptive control scheme, optical models are built that describe the sample structure using as much information about the sample as possible. It is important to account for all layers in the sample structure. This can be accomplished by means of “spectroscopic” ellipsometry.

In this technique, theoretical data from the optical model that corresponds to the experimental data is generated and compared with experimental data. Unknown parameters in the optical model, such as thin film thickness or optical constants or both, are varied to try and produce a "best fit" to experimental data. Regression algorithms are used to vary unknown parameters and minimize the difference between the generated and experimental data. Physical

parameters of the sample such as film thickness, optical constants, composition, surface roughness, etc. are obtained once a good "fit" to the experimental data is achieved [44].

Ellipsometers are frequently used off-line for film thickness measurements. The use of spectral ellipsometers for *in-situ* monitoring and control has been limited by the cost of the units. An additional constraint has been the complexity of the integration of the optics into standard processing tools. The cost issue has slowly improved through the development of lower cost ellipsometers. As processing complexity and the inherent cost of misprocessing wafer continue to increase, spectral ellipsometers may find more opportunity for traction into processing tools for *in-situ* monitoring and control.

In one example [45], an *in-situ* ellipsometer was used to provide real-time thickness measurements and control of process end-point during plasma etching of SiO_2. Thickness values were obtained at intervals of 0.15 seconds. The oxide was etched and the ellipsometer was able to control the etch stop to the desired thickness of 3 Å. In another example, the use of *in-situ* ellipsometry at a wavelength of 1300 nm for etch depth measurement and endpoint detection during RIE of InGaAs(P)/InP heterostructures was reported [43]. Etch depth monitoring and endpoint detection was performed to as low as $0.1\mu m$. The method was also used for in-situ measurement of the wafer temperature during the plasma exposure.

2.4.5 Laser Interferometry

Among the techniques commonly employed to monitor the etch rates of polyimide films are laser interferometry, profilometry of a patterned etch step, and measurement of weight loss with time. Laser interferometry (Figure 2.9) offers the advantage of *in-situ*, nearly real-time

detection of etching rates. The laser interferometer gives direct etch rate measurements at the wafer surface by exploiting interference patterns of monochromatic light rays.

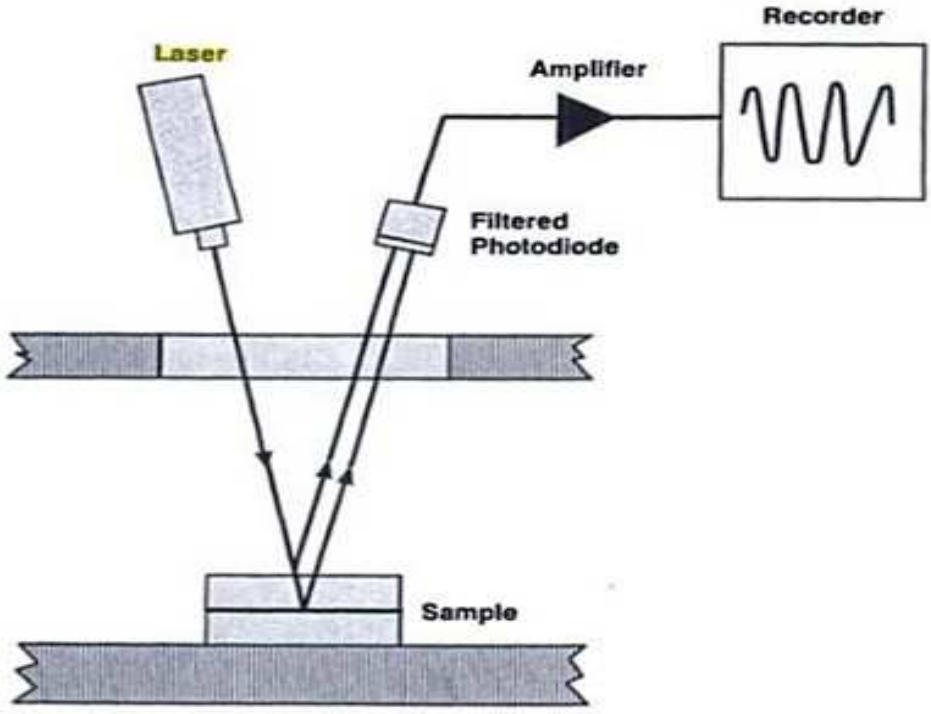

Figure 2.9: Schematic of a laser interferometry apparatus used for in-situ measurement of polyimide etch rates [46].

When monochromatic light is reflected from the front surface and underlying interface, the incident light is partially reflected and partially transmitted by the ambient surface and film. The reflected intensity is a periodic function of the film's thickness and may be appropriately modeled by a sinusoid. The etch rate is directly proportional to the frequency of the periodic signal, according to [46]:

$$\delta = i\lambda[4(n^2 - sin^2\Phi)]^{-1/2} \quad (2.4)$$

where δ is the change in film thickness for i periodic oscillation, λ is the wavelength of the laser, n is the index of refraction of the film being etched, and Φ is the angle of incidence of the laser beam as measured from normal to the surface. For example, at normal incidence, $\delta = i\lambda/2n$, for PMDA-ODA polyimide, n is about 1.76 at 632.8 nm, which is the primary wavelength emitted by an He-Ne laser [46].

Commercially available laser interferometry can be used to monitor etching rates of smooth, partially transparent thin film on smooth reflecting substrates. The "single beam" or "double beam" laser interferometer is recommended for *in-situ* rate/depth measurements. Interferometers are often used in the "reflectance mode", where they monitor changes in the surface reflection. It can also be used in the "interferometric mode", where interference signals from two interfaces (e.g., the top of a transparent layer and its bottom or the bottom of an etch and the coated substrate backside) are used.

The "single beam" laser interferometer is capable of *in-situ* etch rate monitoring and etch endpoint tracing within the layer once etch rate has been established. The standard wavelength for laser interferometry is 675 nm. However, for certain III-V applications (e.g. InP-related materials), 905 nm is often more suitable, since the index contrast between InP-related materials is greater (and absorption is lower) at 905nm. A 905 nm laser endpoint system with high gain amplification of endpoint signal is available more demanding endpoint applications.

Although interferometry works well for endpoint detection, it is limited since it covers only a small spot on the surface of the wafer [46-47]. This technique also only works for

translucent films. Alignment, calibration, and mounting of the interferometer are also concerns and require frequent maintenance. The interferometer must be mounted directly above the sample which might be infeasible for some RIE configurations. Additionally, interferometers, like RGAs, are relatively expensive.

New techniques for monitoring RIE are emerging. In one approach a CCD camera and an optical band pass filter are used to image the wafer and monitor the interference of the plasma emission from a thin film on the wafer surface during the etch. Spatial and temporal variations from the etch can be determined from the CCD images. The acquired data is processed and can be incorporated into a control loop. The initial application of this technique is in run-by-run control of the RIE etch endpoint based on across wafer metrics [48]. The technique has merit but, hardware alignment and data filtering might constrain this application for RIE systems that require this equipment to be mounted on the top of the chamber.

Equipment leader Applied Materials offers a state of the art in-situ OES and interferometric endpoint (IEP) detection solution with their EyeD product (Figure 2.10). The EyeD is mounted over the RIE chamber and monitors the etching process. The EyeD system software allows the user to choose between either interferometer EyeD-IEP endpoint, or optical emission endpoint EyeD-OES.

The EyeD device uses thin film interferometry to detect approaching gate oxide interfaces, enables in situ measurement of nitride thickness, enables depth control for hard mask STI structures, and depth control for trench DRAM recess applications. The EyeD software provides data over the entire spectrum from 200 to 800nm. The user typically defines the spectral range and chooses the wavelength to monitor, and in some configuration, the user can choose one or at most two wavelengths to monitor during the etch [49].

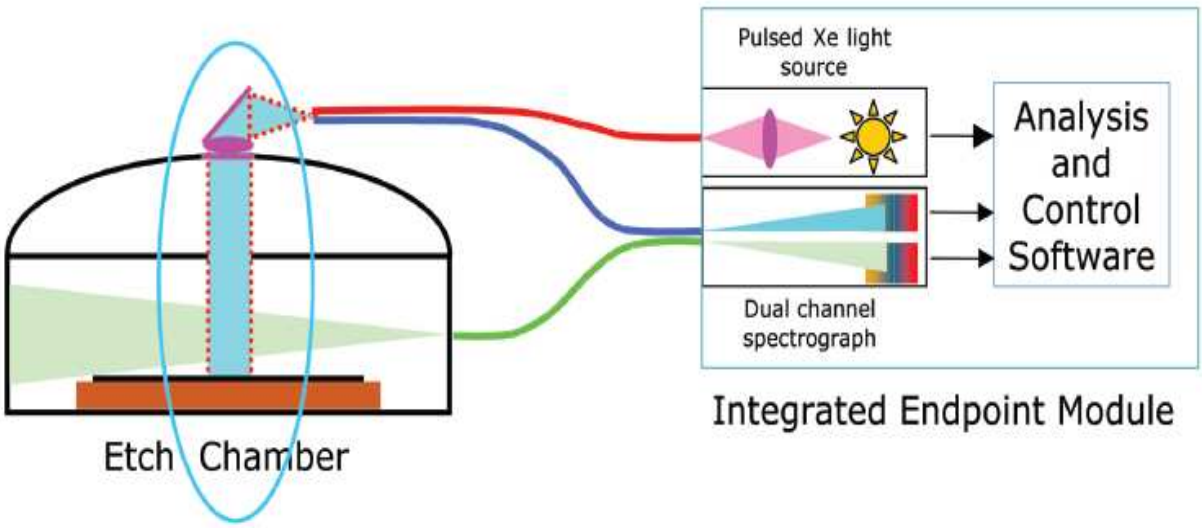

Figure 2.10: EyeD Single-endpoint in-situ metrology data system.

The EyeD product is simple to use and does not require knowledge about film stack, pattern density, or the material optical properties. Some shortcomings of the product are: the setup can be complicated, the structure on the wafer must produce reflected light spectrum that has enough features to ensure stable and accurate results, variations in film thickness and etch rate will cause a distortion of the IEP traces; and reference spectrum taken from bare silicon wafers is required.

Identification of etchant species by wavelength is a difficult process. Species are grouped by etchant species (e.g., *F, Cl, HBr*, etc) and etch byproduct species (e.g., *SiFx*, *SiClx*, etc), with relative intensities. More prominent species require further comparison and characterization of unknown species [33–36]. The availability of the molecular and atomic emission database is considered inadequate. Some spectral data is available from literature that includes data

collected from multiple sources. Commercially available spectral libraries are available but range in prices ($100s - $1K). The information that is contained in these libraries tend to duplicate data that is readily available from other databases (e.g. NIST), or in some cases require additional propriety interfaces [40–48].

2.4.6 Acoustic Time Domain Reflectometry

Acoustic time domain reflectometry (TDR) has been developed as a novel technique for thickness measurement. Acoustic TDR offers the ability to make direct wafer measurements of opaque films deposited on wafers. Acoustic reflection coefficient phase measurements also allow opaque film measurements with the benefit of wafer backside measurements.

The basic setup for acoustic TDR is shown in Figure 2.11 and consists of a pulse-echo set-up in which a short longitudinal acoustic pulse is generated by a ZnO transducer, and the reflected echoes from the sapphire-metal and metal-Si interfaces are analyzed. The thickness, d, of the metal film is determined be measuring the time separation Δt between the reflected pulses,

$$d = \frac{1}{2} V_0 \Delta t \tag{2.5}$$

where V_0 is the acoustic propagation velocity in the metal film. Another technique is in-situ acoustic reflection coefficient phase measurements, where the same basic configuration in Figure 2.10, except the contact is made from the backside of the wafer, and there is no contact with the film being deposited.

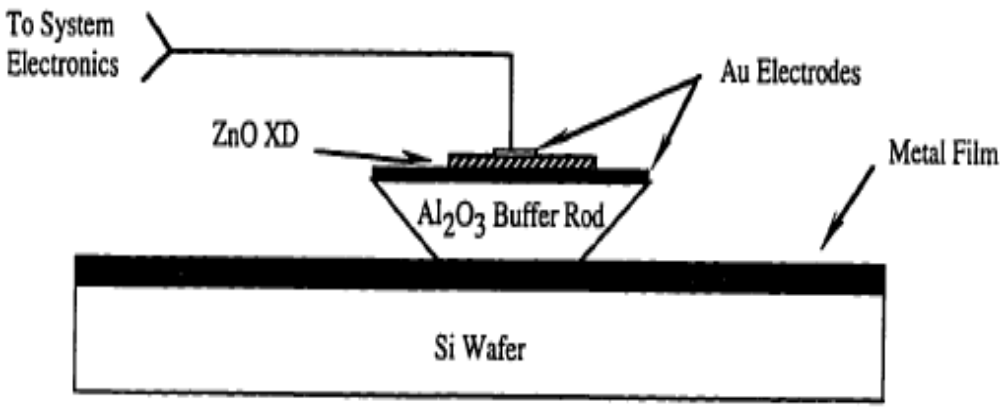

Figure 2.11: Basic diagram of acoustic TDR [20]

This film measurement technique has the advantage of being able to monitor metal films. A disadvantage is that only thickness information can be extracted from the reflected acoustic pulses, unlike optical techniques where several characterizing parameters such as temperature and index or refraction can be determined from the reflected signal [50].

Although generally not recognized, the composition of a known mixture of gases can be determined be measuring the speed of sound in the mixture. Very high sensitivity ($\sim 1\ ppm$) and consistent accuracy is available with acoustic gas composition measurements. There are no components that wear and the energy levels imparted to the chamber gases are low and do not induce any unintended reactions. This feature makes this technique ideal monitoring for chemical vapor deposition and reactive ion etching processes [50–53].

The speed of sound, C, in a pure gas is related to the gas's fundamental thermodynamic property as follows,

$$C = \sqrt{\gamma RT/M} \tag{2.6}$$

where γ, is the specific heat ratio, R, the universal gas constant, T is the temperature in Kelvin, and M is the molecular weight.

Two distinct gas composite measurement devices based on this fundamental thermal principle have been devised [52]. The first implementation measures the transit time for an ultrasonic ($\sim 15\ kHz$) pulse through the gas. The time-of-flight only requires a high resolution timer to measure the time between when a second pulse is generated, and its arrival at a receiver a distance, L, away.

The second implementation measures the resonant frequency of the chamber filled with the target gas mixture (Figure 2.12). A precisely controlled frequency generator is used to stimulate the gas at one end of the chamber, and the intensity of the transmitted sound is measure at another end. The acoustic gas composition chamber's length is fixed, and its temperature is carefully controlled. Hence the speed of sound, C, is related to the resonant frequency, F, as $C = 2FL$, where L is the effective distance between the sending and receiving elements. It is possible to resolve a gas resonant frequency. For example the process gas in RIE chamber that enters the acoustic gas composition chamber,and therefore the speed of sound of the gas to less than 1 part in 50,000 using the resonant technique.

A typical installation of an acoustic composition measuring and control system will have

little effect on the gas supply dynamics of the RIE process chamber, as either implementation adds little volume ($< 25cm^3$) to the RIE gas delivery system. The sensitivity of this technique is strongly influenced by the difference in mass between the species and the range of composition of interest. The technique is most sensitive for low concentrations (less than 5 mol%) of high molecular weight species. Acoustic analysis is stable and reproducible over long periods of operation, and is further improved with routine calibration of the measurement device [52].

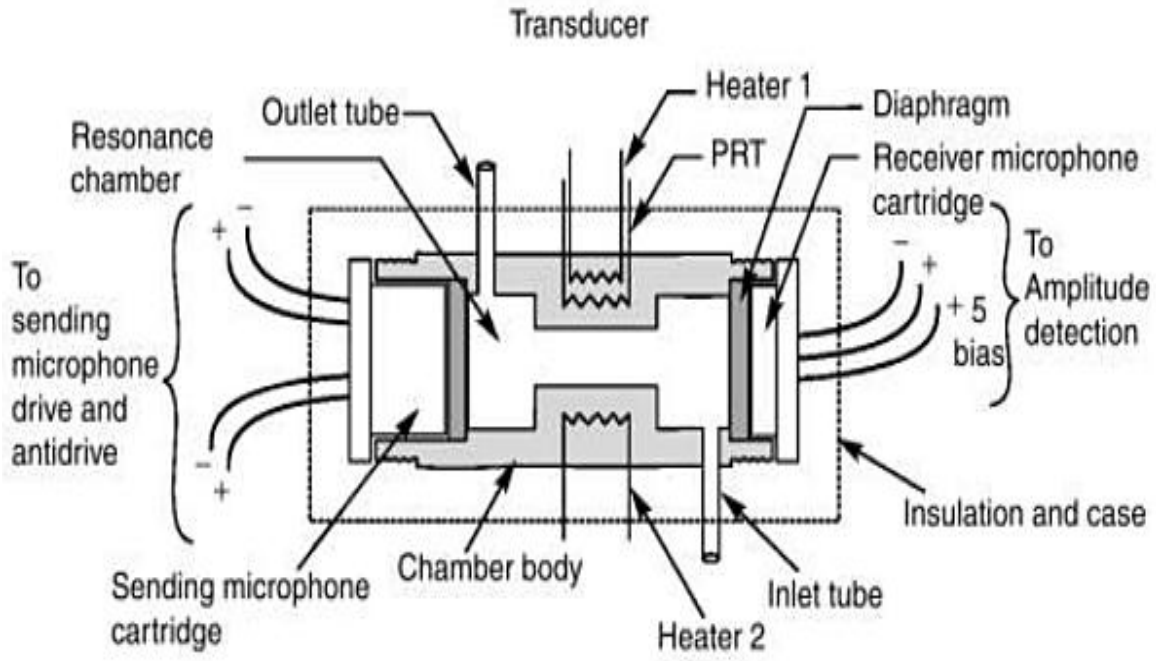

Figure 2.12: **L**ow frequency resonance type acoustic gas analyzer [52].

2.4.7 Emerging Software Techniques

During RIE processes where the material being etched is a significant percentage of the wafer surface area (e.g., metal etch), there is a large change in the plasma chemistry when this material is etched off. Hence the etch rates is more controllable and endpoint signal is very strong and easily detected. The latest challenge for RIE monitoring is low-exposed areas endpoint detection, such as oxide etch in contact holes where the exposed area of the oxide is less than 1% of the wafer area. This type of RIE processing creates a very small chemistry change at the etch endpoint, which generates a very small change in the emission signal intensity. A novel software method for detecting the small chemistry changes based on single wavelength endpoint curves or on full spectral involves neural networks.

The shape of the typical single wavelength endpoint curve is a natural by-product of the processing tool and process chamber conditions. The RIE process exhibits a statistical variation derived from the numerous preceding processes that affect the state of the wafer supplied to the tool, which presents a challenge for both etch rate control and endpoint detection. It is difficult to devise a practical control algorithm that is unique enough to recognize the endpoint, but also general enough to understand the pattern variability (which is a consequence of the tool change and product mix). This challenge can require lengthy empirical evaluation of numerous etch rate data files in an attempt to achieve the correct recipe, which accurately and reliably identifies endpoint for the full suite of endpoint pattern variation [28−30, 54−56].

One approach to this problem is a neural network-based etch rate and endpoint detection algorithm [28−30, 54]. It utilizes a fast training neural network pattern recognition algorithm scheme to determine the endpoint signature. Unlike traditional feed forward neural networks, which require many pattern samples to build an effective network, the methodology employed

with this approach minimizes the number of representative sample data files required for training to typically less than 10. The following three-step procedure outlines the technique.

1. Acquire representative data files exhibiting a full range of endpoints patterns (new patterns can be later introduced into the data set).

2. Tag the endpoint patterns in the collected data files (i.e., identify the region in each data set that contains the endpoint).

3. Train the network – an automatic procedure completed in a few minutes.

This technology has been successfully demonstrated and used in etching oxide with as low as 0.1% open area. The ultimate limits for any specific application are tied to a number of variables. These include the type of tool, process, optical detector, and appropriate selection of emission wavelength(s) being monitored.

2.5 SUMMARY

Several methods exist for etching. The quality of the etch is characterized by its etch rate, anisotropy, selectivity and uniformity. RIE has the advantage of high etch directionality, enabling accurate pattern transfer not obtainable with wet etching. Despite its widespread use, the RIE process mechanism is complex and difficult to monitor and quantify. Real-time monitoring enables the RIE process to remain "centered" within the desired manufacturing tolerance. Precision matching of chamber conditions is also required to meet the increasing demands in process repeatability, partly due to new technology demands, changes in the basic material used in the construction of advanced devices, and the use of novel poly- and organic chemicals and materials. These types of material have rich gas phase chemistries that will influence both the RIE process and the film's material properties, requiring even tighter control during the device fabrication process. The required degree of control for RIE can only be achieved by using in situ sensing to provide data for real time feedback control.

Research has intensified to meet the new challenges in RIE to improve the level of fundamental understanding of the plasma chemistry for new emerging structures when using these complex materials, while employing advanced monitoring and controlling approaches.

This thesis will develop a micromachined resonant sensor that may be placed into the RIE chamber as an alternative to provide direct in-situ measurements of the substrate conditions. This approach will advance the current state-of-the-art due to: 1) non-invasive sensing capability based on microsensor technology; and 2) a simplified detection scheme that relies on the correlation between resonance frequency and the film thickness on the surface of the substrate.

CHAPTER 3

3.1 MICROELECTROMECHANICAL SYSTEMS

The invention of the monolithic integrated circuit (IC) by Jack Kirby and Robert Noyce in 1958 forever changed the way electronic systems were designed. This groundbreaking technology placed previously separated transistors, resistors, capacitors and all the connecting wiring onto a single crystal (or 'chip') made of semiconductor material. IC technologies are usually tailored to digital or analog designs. The trend toward system-on-chip (SoC) solutions makes off-chip components undesirable because of their impact on production quality, cost and size [1, 57, 61−64]. Microelectromechanical systems (MEMS) is an emerging technology which uses the tools and techniques that were developed for the integrated circuit industry to build and integrate many microscopic machines and high frequency components on-chip, that have traditionally been implemented off-chip.

The integration of miniature electromechanical machines, sensors, actuators, and electronics occurs on a common substrate through micro-fabrication technology. While the electronics are fabricated using IC process sequences (e.g., CMOS processes), the micromechanical components are fabricated using compatible "micromachining" processes that selectively etch away parts of the silicon wafer or add new structural layers to form the mechanical and electromechanical devices. The real power of this technology is that many machines can be built at the same time across the surface of the wafer, with no assembly required [57−60].

There is great a diversity of MEMS types and development, primarily driven by existing

and potential high-volume applications in automotive, medical, commercial, and consumer products, where the requirements are typically for moderate performance at very low cost. Accelerometers, pressure sensors and ink-jet printers are the most manufactured MEMS devices. However, these tiny machines are quickly finding their way into a variety of commercial and defense applications, such as miniature inertial measurement units, biochemical analysis on a chip, optical displays, and micro-probes for neural recording. Current and continued success of MEMS stems from the promise of better performance, low manufacturing cost, and the capacity for integration with electronic circuits. Integrated MEMS circuits typically cost less. For example Analog Devices' MEMS accelerometer which is used extensively in airbag systems, sells for about $3-$5 a unit compared to a $1000 accelerometer from a competing technology.

The smaller size and reduced mass of MEMS structures also allows for higher operating frequencies and lower power consumption. These properties make MEMS ideal for portable and remote applications. MEMS-based pressure sensors, used for monitoring truck tire pressure in order to extend tire life, and optical gratings developed for heads-up color displays are examples of the applicability of MEMS. The ability to use the same manufacturing technology to integrate MEMS and electronic systems adds another dimension of utility. Single chip systems of electronics and mechanical sensors are being developed and envisioned for a variety of applications [62-64]. Two examples are the Texas Instruments micro-mirror projection system that is controlled by on-chip RAM cells and the Analog Devices' ADXL202 integrated MEMS accelerometer, which achieves sufficiently high accuracy a requirement for vehicle and personal navigational systems.

This thesis will develop a micromachined sensor using MEMS technology. The sensor may be inserted into an RIE process chamber as an accurate cost effective alternative to direct *in-*

situ measurements of substrate conditions. MEMS technology is the key to achieving the required functionality and performance of the RIE sensor. The device uses a surface micromachined platform that correlates film thickness with changes in resonant frequency that occurs in the micromachined platform during etching, causing a capacitance change with respect to an underlying micromachined electrode. High sensitivity is obtained in the device through improved performance with enhanced Q-factors, better filtering and lower activation power, with the potential for integration with electronics.

In this chapter, conventional MEMS micromachining processes are reviewed, along with their potential for MEMS implementation. Some basic MEMS structures, specifically MEMS resonators, are described in detail. These devices employ a miniature beam driven into mechanical resonance by applying on them mechanical forces at specific frequencies. The resonant frequency is a sensitive measure of strain, but is relatively insensitive to temperature or to the electrical properties of the device. The mechanical complexity and very small size required is made possible only by advances in MEMS technology.

3.2 BULK AND SURFACE MICROMACHINING

Micromachining refers to the fabrication of 3D MEMS structures with the aid of advanced lithography and etching techniques. Lithography patterns the structures, whereas etching removes the selective portion of the substrate of thin film already deposited. In general, the micromachining process either can use the material to form microstructures by etching directly into the material or can use structural sacrificial layers to produce the same.

Bulk micromachining is a fabrication technique which builds mechanical elements by

starting with a silicon wafer, and then etching away unwanted parts, leaving the mechanical devices. Typically, the wafer is photo patterned and the materials are removed by different etching techniques (described in Chapter 2). This is a relatively simple and inexpensive fabrication technology, and it is well suited to applications that do not require much complexity and are price-sensitive.

Surface micromachining creates micromechanical structures from deposited thin films typically composed of materials such as low-pressure chemical-vapor-deposition polycrystalline silicon, silicon nitride, and silicon dioxides. The films are sequentially deposited and selectively removed to build or "machine" three-dimensional integrated circuits structures. Surface micromachining requires more fabrication steps than bulk micromachining, and hence is more expensive. Surface micromachining is suitable for applications requiring more complicated devices, sophisticated elements, and mechanical functionality..

Bulk and surface micromachining have sub-processes in common. Both methods employ photolithography, oxidation, diffusion and ion implantation techniques. There utilize some of the same common materials, like polysilicon, Al, Au, Ti. However the processes differ in many ways, like in the use of anisotropic etchants, anodic and fusion bonding, etch stops, use of Si <100> as a starting material, double-sided processing and electrochemical etching in bulk micromachining, and the use of dry etching in patterning and isotropic etchants in release steps in surface micromachining.

Today, almost all pressure sensors are built with bulk micromachining. Bulk micromachined pressure sensors offer several advantages over traditional pressure sensors. They cost less, are highly reliable, manufacturable, and there is very good repeatability between devices. All new cars on the market today have several micromachined pressure sensors,

typically used to measure manifold pressure in the engine [65-66]. The small size and high reliability of micromachined pressure sensors make them ideal for a variety of medical applications as well [57-64].

While bulk micromachined silicon diaphragm pressure sensors have been commonplace for many years, recent developments are resulting in significantly smaller and potentially less expensive devices. These devices are more suitable for low-to-moderate performance applications, where cost and perhaps size are critical, such as disposable medical sensors and consumer products. One technique developed at the University of Wisconsin uses thin film polysilicon for the sensor diaphragm [67]. Because the polysilicon diaphragm is only about one-tenth the thickness of conventional silicon pressure sensor diaphragms, the polysilicon devices are correspondingly smaller. Another technique employs high temperature fusion bonding of silicon wafers to form inward tapering cavities under single crystal silicon diaphragms [68]. This technique can also result in much smaller sensor dies than standard bulk micromachining techniques. These devices are used in medical catheters, where size and cost are critical.

Surface micromachining is a relatively simple method as compared to bulk micromachining. Surface micromachining fabrication process began in the 1960's, and has rapidly expanded over the past few decades. The application of surface micromachining to batch fabrication in MEMS device was first demonstrated with a resonant gate transistor device by Nathanson and Wickstrom in 1965 [58]. Since then, many other mechanical and optical components and devices composed of microscale movable parts like pistons, spring and gears have been developed.

3.3 MICROMECHANICAL RESONATORS

Micromechanical resonators are structures that can be used for filtering of frequency synthesis applications, due to their high level of frequency selectivity. Every mechanical structure, such as a beam or a disk, has several natural modes of resonance. At macroscale, these occur at very low frequencies – typically lower than a few kilo-hertz. By shrinking the dimension into microscale, higher resonance frequencies can be attained. The mechanical structures are excited into resonance by applying a mechanical force at specific frequencies, known as the resonant frequencies.

To provide the mechanical forces necessary to drive the MEMS structure into resonance, transducers are used to convert energy in one domain to another. Many different types of transducers exist. Usually an electrical signal is produced as a result of the presence of the measurand. This electrical signal can then be modified (e.g., amplified, filtered) in order to meet further requirements. As an example, Figure 3.1 shows the functional block diagram of a MEMS resonator actuated by an electrostatic transducer. A voltage source applied to the input of the resonator, converts it to the mechanical domain as a force, which stimulates the resonant structure by inducing displacement. This filters out the force by attenuating components that are not at the structure's resonant frequency, f_0. The time derivative of the displacement is sensed by the transducer and converted back into the electrical domain as an output current.

MEMS resonators utilizing other types of transduction mechanisms that operate on different physical types exist, but their general block diagram remains the same. For example, piezoelectric crystals which rely on physical stresses, displacement MEMS sensing device having a capacitance transduction element, and magnetic field resonators based on the magnetostriction (change of the length of a magnetic bar in a longitudinal field), or

magnetoelastic (change of Young's modulus of ferromagnetic materials) effects exist [68-74].

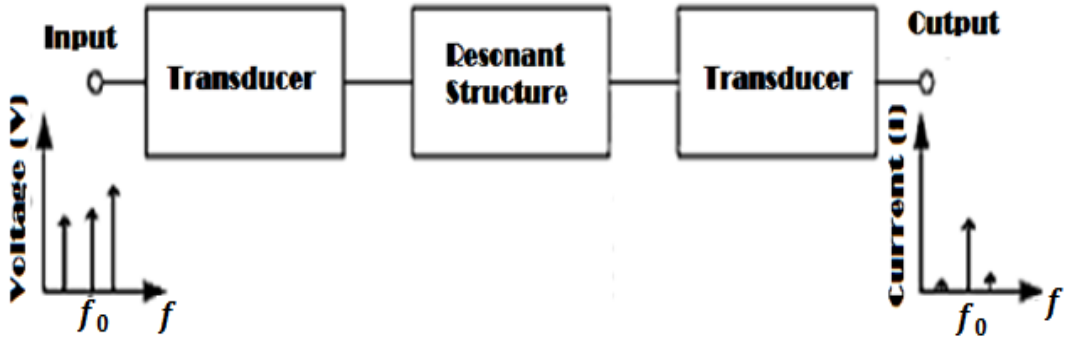

Figure 3.1: Functional block diagram of an electrostatically actuated MEM resonator [63].

3.3.1 Resonant Frequency MEMS Systems

Resonant frequency MEMS systems have generated much interest in the physical measurement and the pharmaceutical industry due to their numerous areas of application. They have been used as filters for signal processing, as chemical and biological sensors, as mass flow sensors, and as pressure sensors [68 - 74]. In addition, there has been much work published on the characterization and fabrication techniques of these resonant frequency MEMS systems.

The resonant behavior (eigenfrequencies and eigenvectors) of the MEMS system is defined by its geometry and mechanical properties. The characteristics associated with the resonant behavior are the resonant frequency, quality factor, vibrational amplitude and phase. The resonant MEMS system relies on a shift in its fundamental mechanical resonant frequency

mode to measure a variety of physical parameters in its surrounding environment. The conversion from the measured quantity to the change of in frequency can be accomplished by the means of change in stress, mass, etc. of the resonator. In general, a resonant frequency MEMS structure consist of a thin film plate that has a microactuator to drive the plate into resonance and a microsensor to determine the resonant frequency of the structure.

The simplest and most often used resonator structures are the beam, the bridge, and the diaphragm, which are illustrated in Figure 3.2. The beam, for instance, may vibrate in a flexural, longitudinal or in a torsional mode as illustrated in Figure 3.3. More complex structures can be envisioned, and when realized, can be used to enhance a specific mode of vibration or to increase the intrinsic Q-factor.

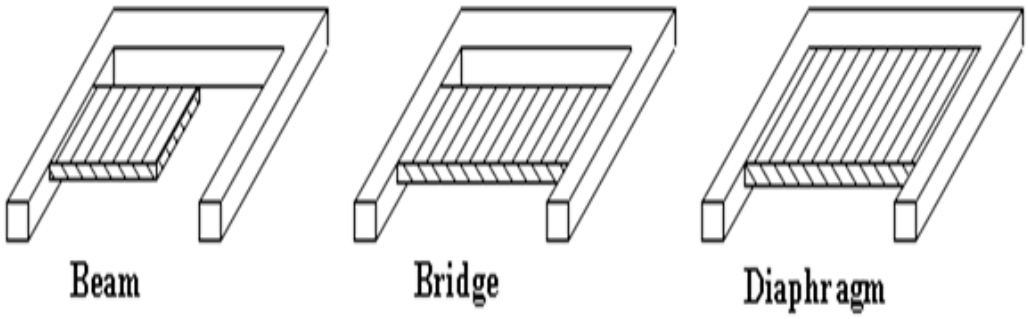

Figure 3.2: Basic mechanical resonator structures

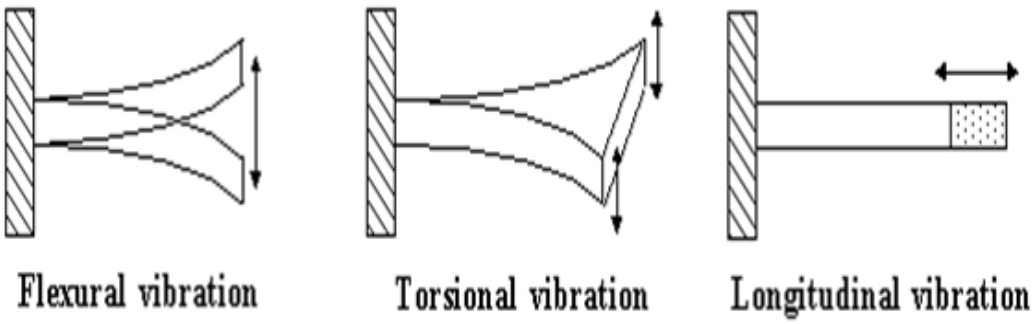

Figure 3.3: Cantilever beams in flexural, torsional and longitudinal vibration modes

Clamped-clamped MEMS resonators has been demonstrated with frequencies of 8 MHz, and have the distinction of being able to attain large stiffness-to-mass ratios [63]. Large stiffness enables large dynamic range and power handling, which was an important design consideration for developing the resonant sensor for the *in-situ* RIE process monitoring application. One drawback of the clamped-clamped topology is that attaining high resonance frequencies would entail scaling down their dimension. This would result in very small sizes and difficulty in achieving a consistent set of useful properties (e.g., Q, dynamic range, power handling) that would meet the need of RIE etch rate monitoring applications.

3.3.2 Resonant MEMS Sensors

MEMS sensor technology is already well advanced, largely based on silicon microfabrication and considerable commercial application. Resonant MEMS sensors have established themselves in the marketplace, usually in applications that require high accuracy.

The key advantage is that the output is essentially digital, and therefore easy to interface to systems without the added measurement error associated with analog to digital conversion. Other benefits are that the measurement principle is usually based on mechanical properties of materials rather than electronic properties, and these can be shown to offer sensors with good stable performance [78-83].

The most popular and dominant resonant sensor is the pressure sensor [68-73]. An early pressure sensor (shown in Figure 3.4(a)) was made from a beam which is attached at both ends to a pressure sensitive diaphragm and pillars. The beam is driven into resonance optically and the two supporting pillars move as a result of the deflection of the diaphragm, which generates stress in the beam and influence the vibrational frequency. The resonant accelerometer (Figure 3.4 (b)) is another popular resonant device which is in high demand and used in large quantities in the automotive industry.

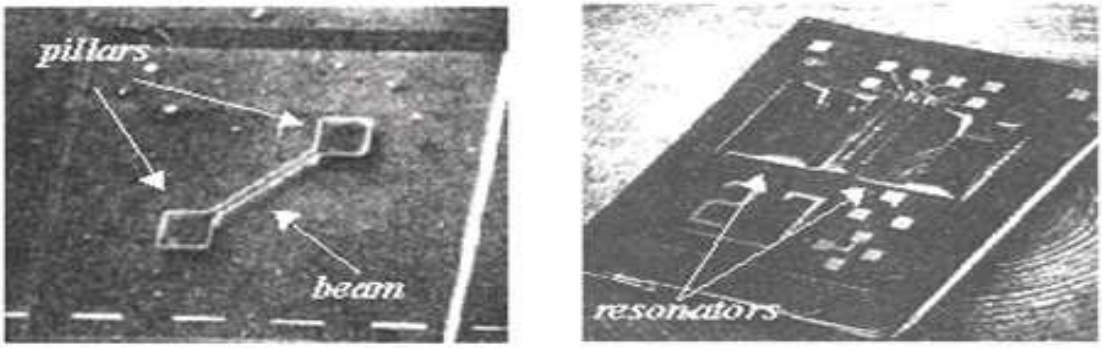

Figure 3.4: Resonant sensors: a) Pressure sensor; b) Accelerometer

Chemical sensors have gained interest continuously in several fields, such as homeland security, to detect biohazard and explosive materials [74]. With the increasing demand, there are many active research projects on chemical sensors based on micro/nano fabrication [74-78]. The devices detect changes in material properties such as resistivity, permeability, and loaded mass, when volatile analyte is absorbed. One example of a resonant chemical MEM sensor is a micro-cantilever that is coated with a material which has an affinity for a specific type of material. If that material is present in the environment, the molecules will be absorbed on the cantilever causing a change in the effective mass of the device, resulting in a shift in the resonant frequency. If the substance is not present, the mass of the cantilever remains unchanged along with its resonant frequency.

Capacitive micromachined ultrasonic transducers (CMUTs) have also been investigated as flexural mode resonators. In one example, a single CMUT cell comprised of a circular membrane is actuated by electrostatic force. Due to the vacuum sealed cavity under the membrane, the CMUT dissipates energy only on one side of the membrane exposed to air. Thus, the CMUT achieves a higher quality factor than that of resonant structures exposed to air from all sides. In addition, multiple membranes were connected in parallel to achieve design flexibility and robustness [81].

3.4. Q-FACTOR CHARACTERIZATION

The quality factor of MEMS resonators is an important figure of merit for improving frequency noise, and hence resolution, especially for selective filtering applications where resonant frequency is determined based on mass loading of the device. The quality factor (Q) of

a MEMS resonator is a metric that characterizes its level of selectivity in the frequency domain and is defined as

$$Q = \frac{f}{f_{BW}} \tag{3.1}$$

where f_{BW} is the $3dB$ bandwidth, f, the center frequency at resonance.

A high Q-factor is important for the electrostatically actuated RIE sensor because it simplifies the feed-back control electronics, minimizes the perturbing effect of the drive electronics, and gives a high resolution. It also implies a very low mechanical coupling, which gives high accuracy and long term stability. In the physical domain, quality factor is defined as [63]:

$$Q = \frac{\Delta E_{stored}}{\Delta E_{loss}} \tag{3.2}$$

where E_{stored} is the stored energy in the resonating structure and E_{loss} is the energy dissipated during the single resonating cycle. Thus to maximize the Q-factor, all sources of energy losses must be minimized. In the case of the RIE sensor, maximizing the device's Q-factor is related to increasing its stiffness (the stored energy) and minimizing the damping mechanisms (energy loss). The Q-factor for the RIE sensor in air, determined from the frequency spectrum is ≈ 12 (Figure 3.5).

The Q-factor is inversely proportional to the rate of energy dissipation. For a vibrating

MEMS structure, several loss mechanisms are present, such as air loss, support loss, thermoelastic (TED) and surface loss. It can be estimated theoretically using the following [63]:

$$\frac{1}{Q} = \frac{1}{Q_{air}} + \frac{1}{Q_{support}} + \frac{1}{Q_{TED}} + \frac{1}{Q_{others}} \tag{3.3}$$

where Q_{air}, $Q_{support}$, Q_{TED} are the air damping, support loss and thermoelastic loss Q-factors respectively. The Q-factor of all other energy losses (e.g. surface loss) is denoted by Q_{others}.

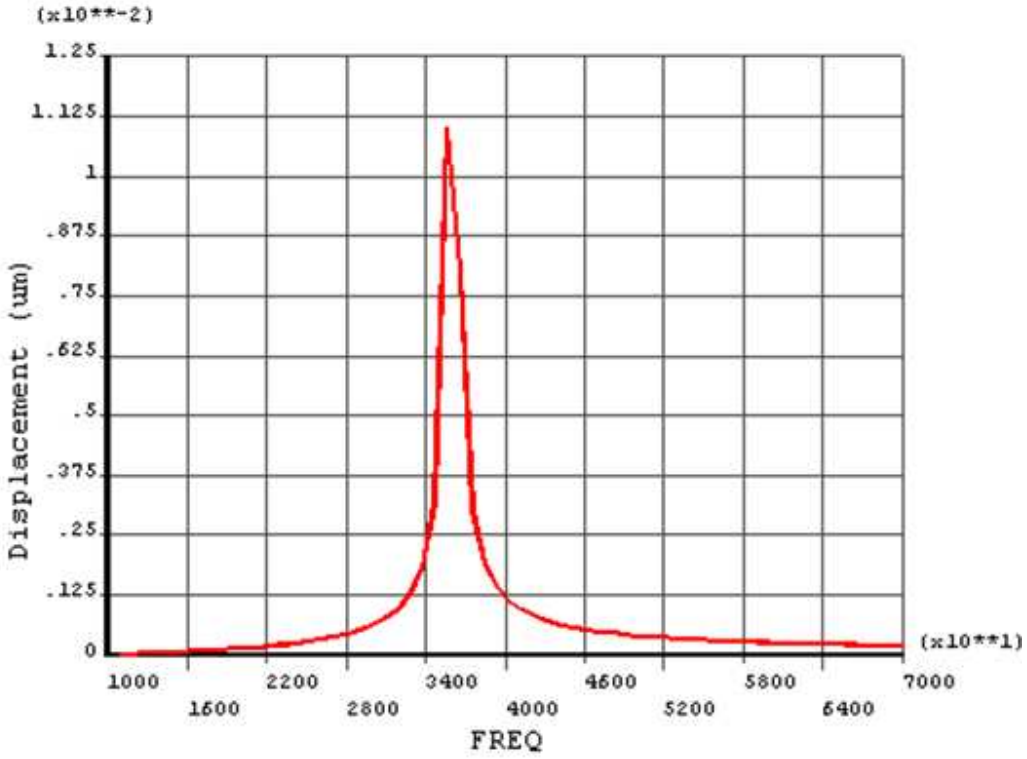

Figure 3.5: Frequency spectrum of the RIE sensor where f is approximately 36 kHz and the Q-factor is 12

When the MEMS resonator structure vibrates, it dissipated energy to the surrounding media (e.g., RIE process chamber). The two main loss mechanisms are air loss and support loss, because the effects of all other losses are minimal, typically in the range of 10^4 to 10^6. The Q_{air} loss is the most dominant Q-factor for flexural mode resonators. Based on analytical fluidic solutions, Q_{air} of a vibrating cantilever with thickness, h, and density ρ can be calculated as [63]:

$$Q_{air} = \frac{2\pi f h \rho}{Z_{air}} \propto \frac{hf}{P} \tag{3.4}$$

where P is the pressure of air and Z_{air} is the acoustic impedance of air. The acoustic impedance of air (Z_{air}) at room temperature is about 420 Pa·s/m, assuming the acoustic impedance is resistive. Based on (3.4), Q_{air}/f depends on the MEMS resonator design parameters as:

$$\frac{Q_{air}}{f} = \frac{2\pi h \rho}{Z_{air}} \tag{3.5}$$

For the RIE MEMS sensor composed of 6.5 um thick polyimide beam, with $\rho = 1400\, kg/m^3$ and $f = 35.3kHz$ the air damping, $Q_{air} \sim 4.8$.

As the RIE sensor vibrates, energy is transferred to the substrate support in the form of acoustic waves. $Q_{support}$ can be expressed as follows

$$Q_{support} = \gamma \left(\frac{L}{h}\right)^3 \tag{3.6}$$

where γ is proportionality constant. The relation is valid for both clamped-free and clamped-clamped MEMS resonators. *Hao et. al.*, analytically calculated $Q_{support}$ for a clamped-clamped beam structure, in [63] as follows

$$Q_{support} = 0.638\left(\frac{L}{h}\right)^3 \tag{3.6}$$

To illustrate, the micromachined RIE sensor with aspect ratio, (L/h) of 108, corresponding to a platform length $L = 700\,um$ and thickness, $h = 6.5\,um$, has a $Q_{support}$ loss = 796,847. Considering only the contribution from both the air damping and the support contact dissipation, the overall quality factor for the RIE sensor satisfies, $1/Q = 1/Q_{air} + 1/Q_{support}$ and the overall Q-factor is ~ 4.8.

In a vacuum, the contribution due to air damping is negligible, and the contact support loss dominates the Q-factor. Therefore, inside the RIE chamber where the pressure is less than atmospheric pressure, and the sensor is expected to operate with higher Q-factors.

3.5 THE RIE RESONANT SENSOR

A schematic of the RIE sensor for *in-situ* etch rate monitoring is shown in Figure 3.6. The sensor is composed of a micromachined platform with length L, width W, and thickness h, $(700um \times 140um \times 6.5um)$, and is made up of layers of polyimide and gold, with Young's modulus E and mass density ρ. The platform is anchored to the substrate and suspended by a gap d, $(4um)$ over drive and sense electrodes with width W_e. The sensor is driven into

resonance electrostatically as material is etched from the platform. As the mass loading of the platform decreases, its resonant vibrational frequency shifts by an amount proportional to the amount of material remaining. The shift in resonance is detected by monitoring the change in impedance between the drive electrodes and the platform. The micromachined platform presents a high acoustic impedance at the point of attachment to the substrate, which means that very little acoustic energy will propagate through the platform to the anchors/substrate, and as a result, maintain a high Q-factor.

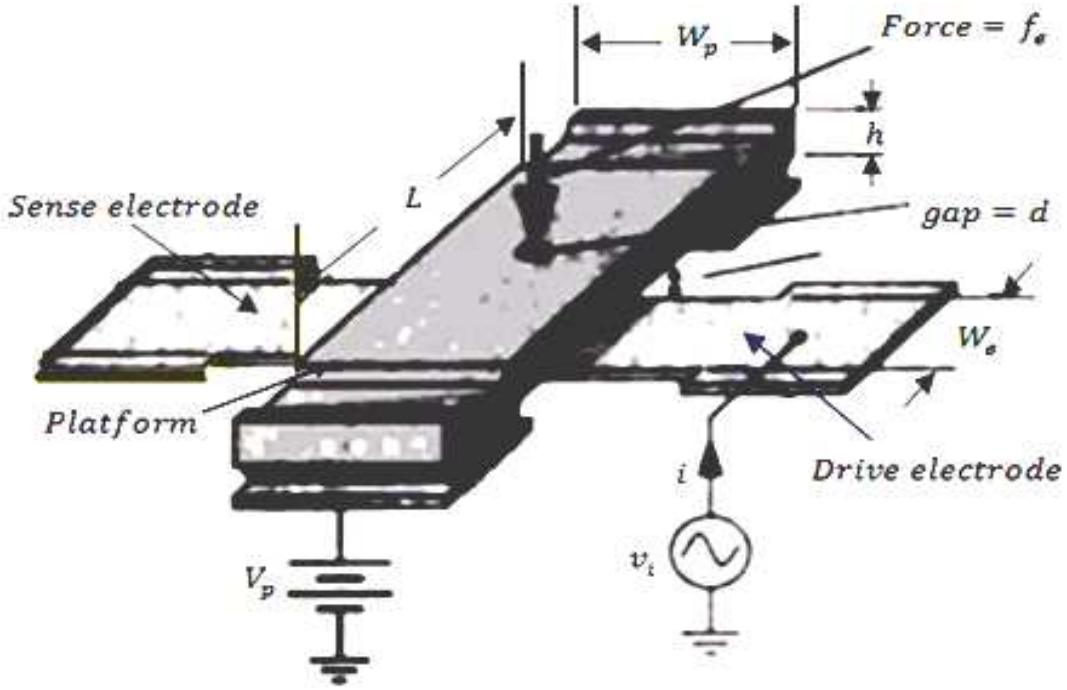

Figure 3.6: Perspective view of micromachined resonant RIE sensor

3.5.1 Theory of Operation

In operation, a dc voltage V_p and an input ac voltage v_i applied across the capacitor, $C = \varepsilon_0 A/d_0$, defined by the area ($W_p W_e$) of overlap between the beam and the bottom electrodes, induce an electrostatic force f_e on the platform, given by

$$f_e = V_p \frac{\partial C}{\partial x} v_i \tag{3.7}$$

that cause it to vibrate vertically exhibiting displacement x_i. In this expression, the derivative $\partial C/\partial x$ represents the change in electrode-to-platform capacitance per unit displacement of the platform and is given by:

$$\frac{\partial C}{\partial x} = \frac{W_p W_e}{d_0^2} \tag{3.8}$$

Where d_0 is the unbiased platform-to-electrode gap. The displacement of the platform in response to v_i induces a capacitive current given by

$$i_z = V_p \frac{\partial C}{\partial x} \times \frac{\partial x}{\partial z} \tag{3.9}$$

and is largest when the excitation frequency is close to the mechanical resonance frequency of

the platform.

The RIE sensor structure is not readily described by the simple parallel plate capacitor configuration. A natural consequence of surface micromachining fabrication techniques (patterning and stacking of layers), is that the movable part of the RIE sensor (the platform) consists of thin films of flexible materials, floating above the electrodes and clamped on both sides. A more accurate description requires the theory of the bending of plates and beams when subjected to a certain load.

3.5.2 Vibrational Analysis

The equation of motion that describes the small deflection of the platform can generally be described by the 1-D homogeneous Euler-Bernoulli equation [60]:

$$\bar{E}I\frac{\partial^4 w(x,t)}{\partial x^4} + \rho A\frac{\partial^2 w(x,t)}{\partial t^2} = 0 \tag{3.10}$$

With apparent Young's modulus $\bar{E}$, A is the cross-sectional area, I is the moment of inertia and ρ is the material density. The apparent Young's modulus is a function of the Poisson's ratio v, when the platform width, W is much larger that the platform thickness, h. For the RIE sensor $W \gg h$ and the apparent Young's modulus, $\bar{E} = E/(1 - v^2)$.

The moment of moment of inertia of the sensor platform is given as:

$$I = \int_0^W \int_{-h/2}^{h/2} z^2 \partial z \partial y = \frac{1}{12} W h^3 \tag{3.11}$$

Assuming harmonic solution, the separation of variables technique may be used to isolate the time and space parts of Equation 3.10. Separation of variables yields:

$$\frac{\bar{E}I}{\rho A} \frac{\partial^4 w(x)/\partial x^4}{w(x)} = \omega_0^2 = const. \tag{3.12}$$

The general solution of the DE has four roots and is given as:

$$w(x) = C_1 \cos\left[\frac{\lambda}{L}x\right] + C_2 \sin\left[\frac{\lambda}{L}x\right] + C_3 \cosh\left[\frac{\lambda}{L}x\right] + C_4 \sinh\left[\frac{\lambda}{L}x\right] \tag{3.13}$$

The dimensionless parameter λ results from

$$\left(\frac{\lambda}{L}\right)^4 = \frac{\rho A \omega^2}{\bar{E}I} \tag{3.14}$$

We can find the constants by applying the following boundary conditions for the clamped-clamped beam:

$$w(0) = w'(0) = w(L) = w'(L) = 0 \tag{3.15}$$

The value of λ_n that satisfies the characteristic equation, $\cos\lambda \cosh\lambda$ may be determined from a trigonometric table. For the RIE sensor λ_1 = 4.730 for the fundamental mode of vibration (which is of primary interest). The other mode shapes for a clamped-clamped beam are λ_2 = 7.853 and λ_3 = 11.0. We can now write the general expression for the resonance frequencies of the RIE sensor platform [60]:

$$\omega_n = 2\pi f_n = \frac{\lambda_n^2}{\sqrt{12}}\frac{h}{L^2}\sqrt{\frac{\bar{E}}{\rho}} \tag{3.16}$$

To illustrate, for the RIE sensor with Young's modulus $E = 8.3GPa$, density $\rho = 1400\, kg/m^3$, Poisson's ratio $v = 0.34$, length $L = 700\mu m$ and platform thickness $h = 6.5\mu m$. The calculated fundamental resonance frequency $f_1 = 35.3kHz$. Estimates of the first three resonance frequencies are summarized in Table 3.1.

Table 3.1: Calculated resonance frequencies of the RIE sensor

Mode	***Resonance Frequency***
$\lambda_1 = 4.73$	$f_1 = 35.3kHz.$
$\lambda_2 = 7.853$	$f_2 = 97.4kHz.$
$\lambda_3 = 11$	$f_3 = 191.2kHz.$

The physical model presented above describes both the relationship between the resonant frequency and the RIE sensor platform, and the behavior of the RIE sensor. The various modes of the platform's vibration are more sensitive to variation in the platform's height than the platform's length (Figure 3.7). In operation, the RIE sensor's platform is coated with material that is etched. As the height of the platform (including film thickness) decreases, the resonant frequency decreases by an amount that is proportional to the amount of material etched.

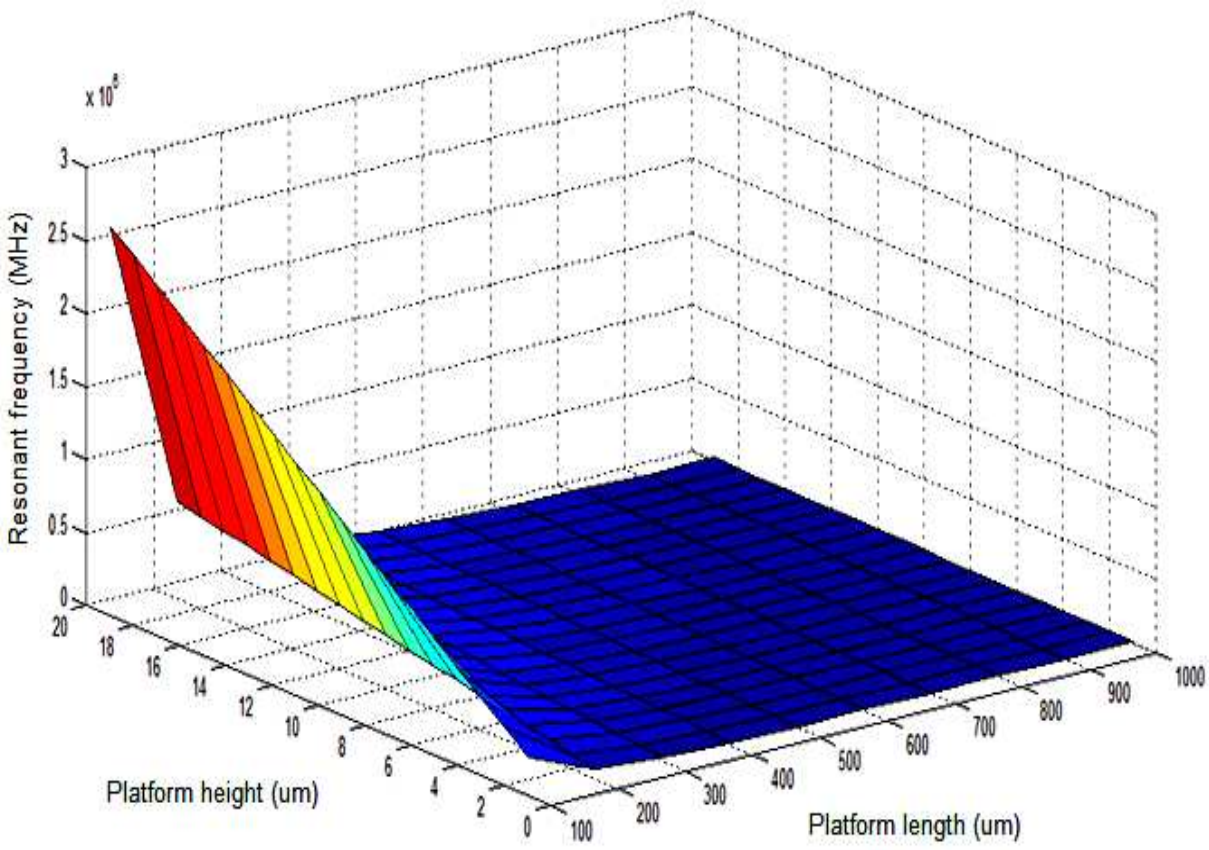

Figure 3.7: Resonance frequency of the RIE sensor as a function of the platform height and length

3.5.3 Electrical Circuit Model

The RIE sensor can be treated as an electrostatically driven one-port resonator, shown in Figure 3.8. In this configuration, the polarization voltage, V_p, and the ac signal v_i, are superimposed at the drive electrodes. The resulting electrostatic force will cause the beam to vibrate. The resonance of the platform will be reflected in the current $i(t)$, and at resonance, the impedance of the air gap changes.

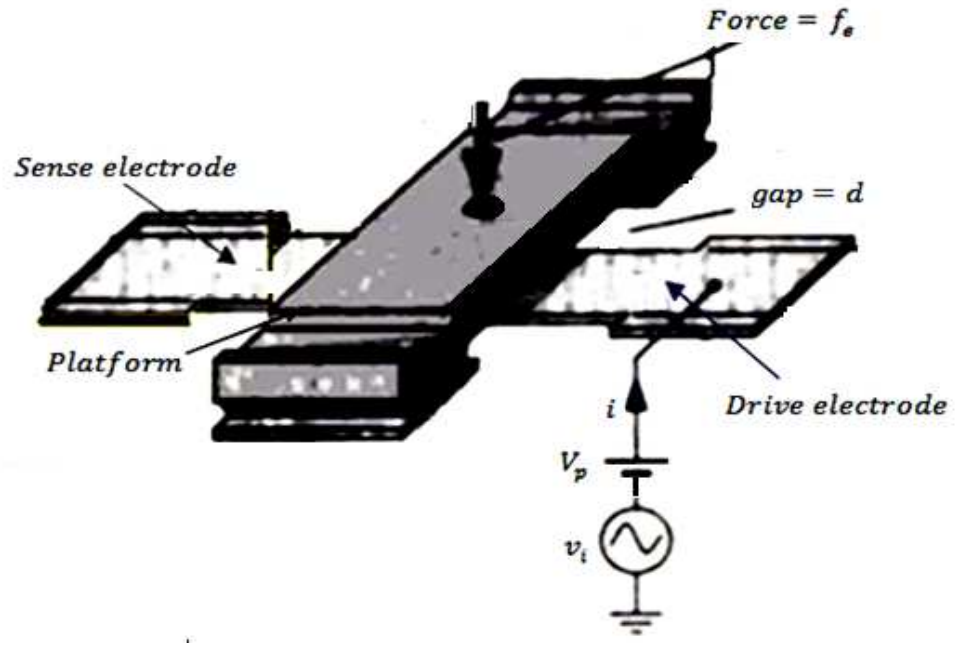

Figure 3.8: The RIE sensor configured as an electrostatic one port resonator

The electrical circuit model is carried out with the help of electromechanical analogies shown in Table 3.2. The analogies enable a path back to the mechanical world where the physical realization of the device lies.

Table 3.2: Mechanical-to-Electrical Current Analogy [68]

Mechanical Variable	Electrical Variable
Damping, c	Resistance, R
Stiffness^{-1}, k^{-1}	Capacitance, C
Mass, m	Inductance, L
Force, f	Voltage, V
Velocity, v	Current, I

In the vicinity of the fundamental mode of resonance, the dynamic small signal behavior of the RIE sensor can be represented by a simplified equivalent circuit shown in Figure 3.9.

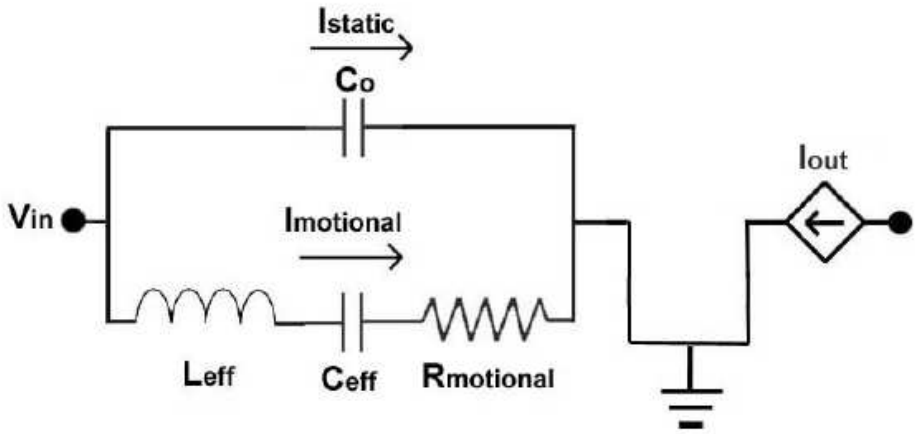

Figure 3.9: Equivalent circuit model for RIE sensor excited at one port

The static capacitance C_0 represents the capacitance of the air gap. The $R_{motional}L_{eff}C_{eff}$ series branch represents the motional behavior associated with the fundamental mode. In developing the electrical model, the effects of the electrical bias on the platform must be considered.

The "pull-in" voltage V_p, is defined as the largest polarizing voltage (DC bias) that can be applied to the RIE sensor before the platform collapses. It is given by:

$$V_{PL} \approx 3.48 \frac{1}{L^2} \sqrt{\frac{\bar{E} h^3 d^3}{\varepsilon_0}} \tag{3.17}$$

Here, E, d, h are the Young's modulus, air gap, and platform thickness, respectively, and ε_0 is the permittivity of free space. For the RIE sensor, the calculated pull-in voltage $V_P = 31V$.

The resonance frequency of the RIE sensor is affected by the DC offset "bias" voltage. As the polarization "bias" voltage increase, the resonant frequency decreases (Figure 3.10). This relationship is described by:

$$\omega_s \approx \omega_1 \sqrt{1 - 0.29 \left(\frac{V_p}{V_{pl}}\right)^2} \tag{3.18}$$

where ω_1 is the fundamental resonance frequency derived previously.

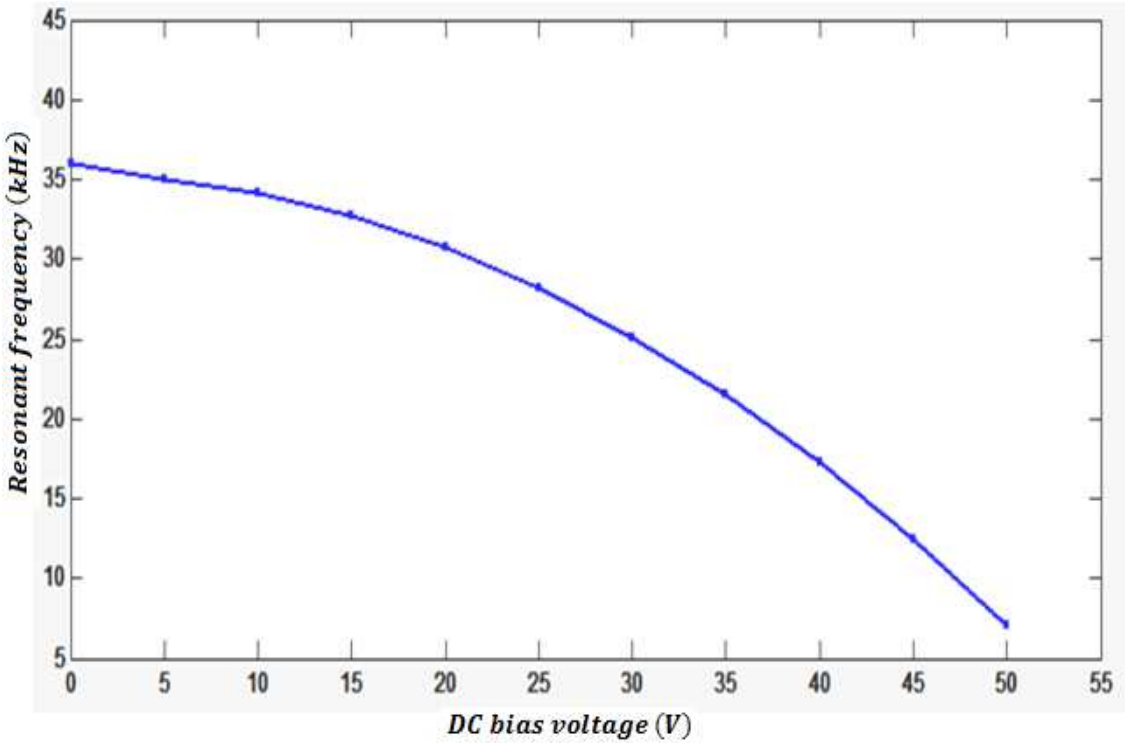

Figure 3.10: The resonance frequency dependence on the applied dc bias voltage V_p

The bias voltage plays a crucial part in the analysis of resonant behavior of the RIE sensor. In the first place, it determines how mass, stiffness and damping are to be translated in the equivalent lumped elements, L_{eff}, C_{eff} and $R_{motional}$, and is essential for the coupling between the electric and mechanical domain. Secondly, it is easy to understand that tuning the bias voltage will affect the resonance frequency.

Note that this equivalent circuit applies only at the fundamental resonance mode, and contributions of higher order resonances are assumed negligible. Higher resonance modes can be incorporated by adding appropriate RLC branches in parallel to the first one, which introduces more impedance than the first mode.

The capacitive circuit element C_{eff} is defined as:

$$C_{eff} \approx 0.2 \frac{\varepsilon_0 WL}{d} \frac{\left(\frac{V_p}{V_{pl}}\right)^2}{\left(\frac{\omega_S}{\omega_1}\right)^2} \tag{3.19}$$

and the inductance L_{eff} is expressed as

$$L_{eff} = \frac{1}{\omega_S^2 C_{eff}} \tag{3.20}$$

The motional resistance $R_{motional}$ is related to the mechanical Q-factor of the structure and is expressed as

$$R_{motional} = \frac{1}{Q_S \omega_S C_{eff}} \tag{3.21}$$

It should be noted that $\omega_1 = 1/\sqrt{L_{eff} C_{eff}}$ and also $Q = \omega_1 L_{eff}/R_{motional}$ [75].

It is desirable to reduce the motional resistance and increase the electromechanical coupling between the RIE sensor's platform and the electrodes. Two ways to increase the coupling factor are to increase the applied bias voltage and increase the coupling capacitance. The coupling capacitance can be increased by decreasing the gap spacing. In operation, as the RIE sensor platform is etched the mass loading decreases and gap between the platform and electrodes increases which reduces the coupling capacitance. The implications and effect of the wider gap can also be seen by examining the motional resistances. Table 3.3 summarizes the calculated effective gap impedance values with varying gap spacing.

Table 3.3: Calculated equivalent circuit and effective impedance values for the RIE sensor with varying gap width. The Q-factor is estimated at 1000 and the DC bias is 10 volts

$Gap\ Width\ (\mu m)$	$C_0\ (pF)$	$R_{motional}\ (\Omega)$	$C_{eff}\ (fF)$	$L_{eff}\ (H)$
4.0	0.217	967,958	4.81	4510
3.5	0.247	846,023	5.53	3934
3.0	0.289	725,710	6.44	3366

3.6 SUMMARY

As described above, there are many significant developments under way for improved sensors and sensors for new variables, with new structures and operating principles, with improved performance, and reduced cost. The specialized nature of MEMS fabrication processes makes cost-effective fabrication an issue for low to moderate volume applications. High reliability and stability in the real operating environment are critical requirements for many sensors. These requirements are difficult to achieve, and continued development is required for many applications and products.

MEMS technology is the key to achieving the sensor being developed for the *in-situ* RIE process monitoring application. The device uses a surface micromachined platform that correlates film thickness with changes in resonant frequency that occurs in the micromachined platform during etching. The vibrational and electrical behavior of the clamped-clamped structure was investigated, which is the basis of the RIE sensor functionality and performance.

A high Q-factor is important for the electrostatically actuated RIE sensor because it simplifies the feed-back control electronics. The Q-factor for the RIE sensor in air, determined from the frequency spectrum is ≈ 12. In a vacuum, the contribution due to air damping is negligible, and therefore, inside the RIE chamber where the pressure is less than atmospheric pressure, and the sensor is expected to operate with higher Q-factors.

The RIE sensor is composed of a micromachined platform that is suspended above the drive and sense electrodes on the surface of the substrate. The physical model presented describes both the relationship between the resonance frequency and the RIE sensor platform, and the behavior of the RIE sensor. The various modes of the platform's vibration are more sensitive to variations in the platform’s height. In operation, the RIE sensor’s platform is coated

with material that is etched. The resonant frequency decreases by an amount that is proportional to the amount of material etched, allowing etch rate to be inferred.

CHAPTER 4

4.1 CAPACITIVE SENSING

The physical structure of the capacitive RIE sensor, described in the Chapter 3, is relatively simple. However, the simple parallel plate equation for capacitance only provides a crude estimate of the expected capacitance change. Measuring capacitance changes with the RIE sensor relies on capacitive transduction, which is one of the most important and widely used techniques, in micro systems. The capacitance changes are extremely small (in the range of femto- to atto farads), and the parasitic capacitance, together with the RIE sensor capacitance, are usually larger than the varying capacitance to be sensed. Small capacitance changes, along with the additional noise from the RIE process chamber, makes *in-situ* film thickness monitoring challenging. The technique nevertheless, provides a precise way of sensing the changes in capacitance and resonant frequency that occurs during etching.

In general, the sensor's overall performance is often limited by the interface circuit. The main challenge of the interface circuit is to sense the small capacitance variance with huge parasitic capacitances. The variety of different types of interface circuits include the impedance bridge, the charge amplifier (often used with piezoelectric devices), charge balance techniques, and various oscillator configurations. These circuits are shown in Figure 4.1. There are also a variety of commercially available ICs that can be used to measure capacitance changes of a few femtofarads in stray capacitance up to several hundred picofarads.

The impedance bridge uses a high-frequency (HF) oscillator which drives an RC bridge. The bridge contains the sensor and a reference capacitor. As soon as there is an imbalance in the bridge due to a change in the sensor capacitance, an output occurs. This bridge configuration is very simple, but has a limited dynamic range. Such a measurement setup is very sensitive to parasitic effects, which are always present in capacitive micro-mechanical structures. Moreover, these parasitic capacitors quite often have a comparable value to the sensing capacitor, making read-out difficult.

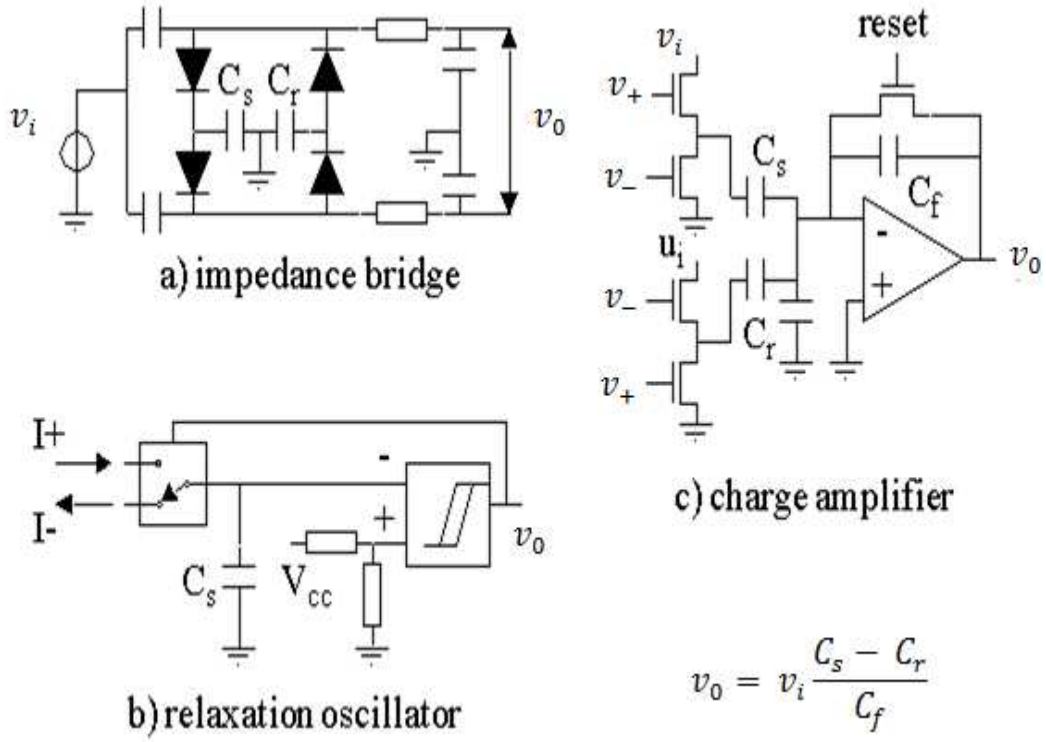

Figure 4.1: Circuits that can be used to interface with the capacitive RIE sensor

The RIE sensor is similar in operation to a variable capacitor and can also be used to control the frequency of a relaxation oscillator. The oscillation period for example in a Schmitt trigger oscillator is determined by the charging time of the measured capacitor. Since the oscillator links the time varying capacitance with a frequency output, it is quite attractive to use if A/D conversion or a digital output is needed. The simplicity of this type of circuit configuration is routinely implemented using CMOS technology for applications requiring capacitive read-out of mechanical sensors.

DC and AC-operated charge amplifiers can also be used to measure capacitance changes. The schematic shown in Figure 4.2 is a practical capacitive sensing circuit.

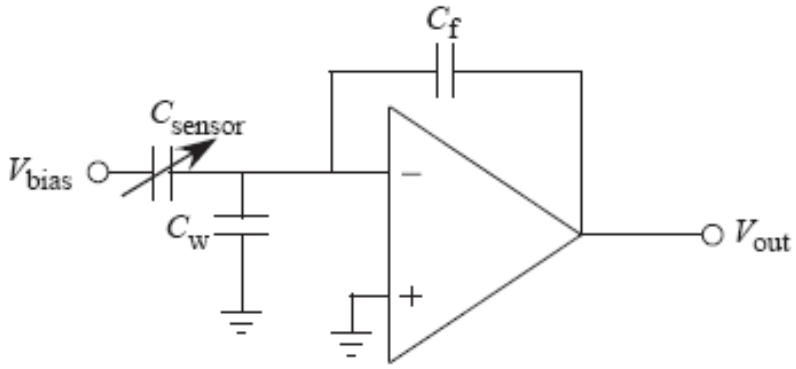

Figure 4.2: Charge amplifier capacitive sensing circuit configuration [90].

Capacitance to voltage conversion is achieved using a capacitive feedback loop. A sinusoidal bias voltage applied to the RIE sensor capacitance C_{sensor}, will cause a sinusoidal current. The parasitic capacitance from the floating node to ground is modeled by C_w. The feedback capacitor

C_f, converts the capacitive current into a voltage which is proportional to the value of the RIE sensor capacitance [84]. If one assumes an ideal op-amp characteristic the output signal is

$$V_{out} = -\frac{C_{sensor}}{C_f} V_{bias} \tag{4.1}$$

The response is a linear function of RIE sensor capacitance. In the RIE monitoring application, we are concerned in the change of the sensing capacitance rather than the absolute value.

Figure 4.3 shows the small-signal model of the circuit in Figure 4.2 above. The amplifier is modeled as a first order system by the transconductance, G_m and output impedance, R_o. The sensing amplifier is followed by an output buffer with load capacitance C_L.

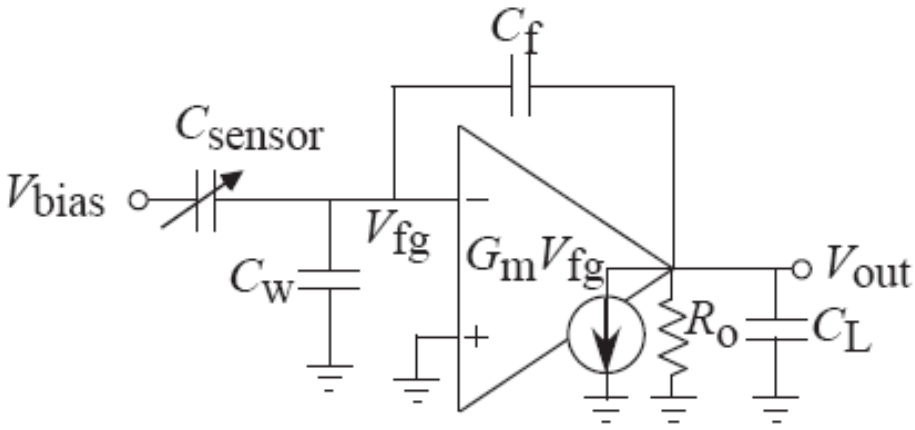

Figure 4.3: The small-signal model of the capacitive sensing circuit [90].

The DC output voltage can be expressed as [90]:

$$V_{out} = -\frac{V_{bias}C_{sensor} + Q}{C_f + C_T/A_V} \tag{4.2}$$

Where Q is the charge on the floating node, $A_V = G_m R_o$ and $C_T = C_{sensor} + C_w + C_f$. By tuning the charge on the floating node, the DC level of V_{out} can be adjusted to the mid-rail and the output dynamic range can be rail-to-rail. If there is some variance in C_{sensor}, and assuming the amplifier gain is high enough $(A_V \gg C_T/C_f)$, the output voltage variance of the RIE sensor capacitance can be expressed as

$$\Delta V_{out} = -\frac{V_{bias}}{C_f} \cdot \Delta C_{sensor} \tag{4.3}$$

It can be seen from (4.2) and (4.3) that this circuit amplifies the changes in sensor capacitance while decreasing constant capacitances at the floating node by the amplifier gain. The amplitude of the output signal will be proportional to the variance of C_{sensor} with the transducer gain of $-V_{bias}/C_f$. The circuit can achieve high sensitivity by choosing a large value of V_{bias} and a small value of C_f.

The capacitive feedback charge amplifier topology has been used for decades. However, when it is used in capacitive sensing applications, large resistors or switches are inserted to provide the DC path for the floating node. The additional component deteriorates the performance of the charge amplifier and consumes more power. Recent advances in programming and adapting floating gate circuits, for example the auto-zeroing floating gate

amplifier (AFGA) [78−80] capacitive sensing interface, provide high signal-to-noise (SNR) with very low power consumption.

The floating node or floating gate was previously introduced in the discussion of the capacitive charge amplifier sensing circuit. The AFGA is an example of a large class of adaptive floating-gate MOS circuits. These circuits use tunneling and hot-electron injection to adapt the charge on floating gates to return the circuit to a baseline condition on a slow time scale. In Section 4.2, the discussion will explore floating gates before continuing with further analysis of the capacitive sensing interface circuit in Section 4.3.

4.2 FLOATING-GATE CIRCUITS

Floating-gate devices, circuits and systems utilize floating-gate MOS transistors circuits and are found in many common devices, including EPROMs, EEPROMs, and flash memories. A floating gate is a polysilicon gate of a MOS transistor that is surrounded by SiO_2. Charge on the floating gate is stored permanently, providing a long-term memory, because it is completely surrounded by a high quality insulator. The charge on the floating gate can be modified by applying a large voltage charge, by projection of UV light source on the chip, or by adding electrons using hot electron injection. The first report of floating-gate devices was in 1967 and the technology has matured significantly since to where floating gate devices are now found in every personal computer today [85−86].

Floating-gate devices and circuits are divided into three major application areas. They are used: 1) as analog memory elements; 2) as parts of capacitive based circuits; and 3) as adaptive circuit elements. Floating-gate technology is used to eliminate off-chip biasing voltages

in analog and mixed mode VLSI systems by providing voltages on-chip with array of programmable floating-gate voltages. In a CMOS application, ultraviolet light was applied to a floating-gate device to tune the threshold voltage for optimal performance [85−89].

A floating gate occurs when there is no dc path to a fixed potential. The floating-gate voltage can modulate a channel between a source and drain and can therefore be used in computation. Capacitive coupling into the floating gate becomes an effective gate for the transistor, where the gate strength depends on the capacitor size. The floating gate can compute a range of translinear functions by capacitive couplings into floating gate devices with an exponential current-voltage relationship.

Floating gate circuits have an inherent ability to adapt to outgoing and incoming signals by continuously enabling various programming mechanisms. The development of single floating gate FETs that emulate the computational and adaptive properties of biological synoptic elements was motivated by floating gates adaptive properties. A spectrum of continuous-time adaptation dynamics of floating gates and methods to take advantage of these floating gate devices was illustrated by Hasler [84−90]. Reports on systems using floating gate adaptive systems include schemes for adaptive gain correction in photovoltaic camera systems and methods for weighing different frequency bands with analog weights stored on floating gates.

One example of a continuously adapting floating gate pFET circuit is the autozeroing floating gate amplifier (AFGA). The AFGA is a high-gain amplifier with two key features due to the use of floating gate MOSFETs: (1) capacitors used in ways resistors are traditionally used in discrete amplifiers; and (2) hot-electron injection and electron tunneling used to generate small continuous currents.

Figure 4.4 shows the AFGA, for which the open-loop amplifier consists of a pFET input transistor and an nFET current source.

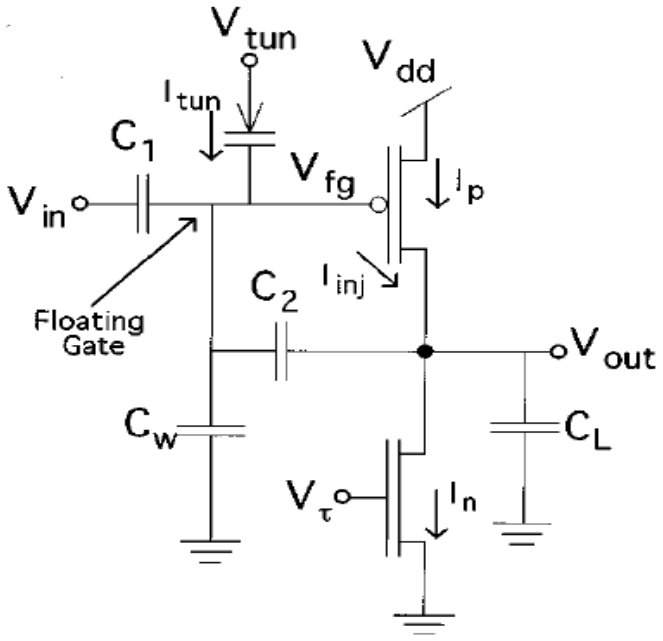

Figure 4.4: An autozeroing floating-gate amplifier (AFGA) that uses tunneling and pFET hot-electron injection [88].

The AFGA uses tunneling and pFET hot-electron injection to adaptively set its DC operating point. The complementary tunneling and hot-electron injection processes adjust the floating gate charge so that the amplifier output voltage returns to steady-state on a slow time scale. The bias current I_0 is set by the nFET current source. Since the output capacitances are charged or discharged by currents on the scale of I_0, the cutoff frequency will be directly dependent on the bias current. Furthermore, with capacitive feedback, the input signal is

amplified by a closed-loop gain approximately equal to C_1/C_2, and for usual operating conditions the AFGA's open-loop gain also is large (~ 1000) and nearly constant [88].

Figure 4.5 shows the response of the autozeroing floating gate amplifier to a 1-Hz sine wave superimposed on an input pulse. If the input changes on a time-scale that is much shorter than the adaptation, then the output is an amplified version of the input signal. The amplifier adapts to the pulse input after an initial transient while preserving the 1-Hz sine wave. The AFGA has a closed-loop gain of 11.2 and a low frequency cutoff at 100 MHz [90].

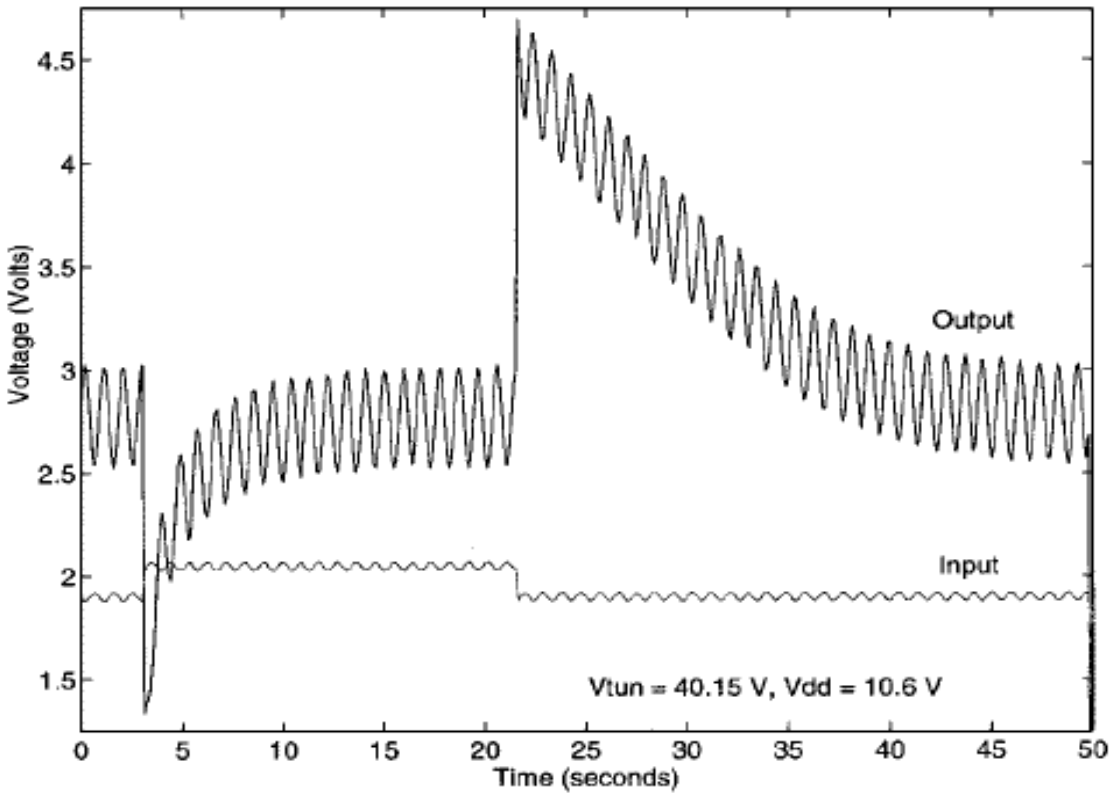

Figure 4.5: Response of the AFGA to a 1-Hz sine wave superimposed on a 19-s voltage pulse [90]

The combination of electron tunneling and pFET hot-electron injection applies the appropriate negative feedback to stabilize the output voltage. If the output voltage is below its equilibrium value, then the injection current exceeds the tunneling current, decreasing the charge on the floating gate. That, in turn, increases the output voltage back toward its equilibrium value. If the output voltage is above its equilibrium value, then the tunneling current exceeds the injection current, increasing the charge on the floating gate, which decreases the output [90].

At high frequencies, the autozeroing floating gate amplifier is a low-pass filter. In this regime, the tunneling and injection currents are negligible. At extremely high frequencies, the transistor channel currents are negligible compared to the capacitive currents. The behavior of the AFGA results from the floating gate voltage settling back to its equilibrium condition. The AFGA frequency response was derived in [84] and is given for all frequencies as

$$\frac{V_{out}(s)}{V_{in}(s)} = -\frac{C_1}{C_2} \cdot \frac{1 - \tau_{h2} s}{1 + \tau_h s + \frac{1}{\tau_l s}} \tag{4.4}$$

where the time constants, $\tau_{h2} = C_1 C_o U_T / \kappa C_2 I_\tau$ is the time constant that marks the onset of capacitive feedthrough. The high-frequency time constant cut-off, $\tau_h = (C_T C_o - C_2^2) U_T / \kappa C_2 I_\tau$ and τ_l, the low-frequency cutoff, is equal to $C_2 V_{inj} / I_{tun0}$. The AFGA has four operating regimes based on the operating frequency behaving as either a high-pass filter, as a low-pass filter, an amplifier and at the highest operating frequency in a capacitive feedthrough manner.

The AFGA is stable and its noise performance is similar in thermal characteristics to standard MOS amplifiers. The tunneling and injection do not add noise to the amplifier, and

when the appropriate feedback is applied to the floating gate, no additional control circuitry is required.

The schematic in Figure 4.6 is of an integrated auto-zeroing capacitive sensing amplifier, where the tunneling junction and an indirect injection p-MOS transistor are integrated with the amplifier. A comparator is used to provide the drain voltage of the injection transistor so that the injection current can be adjusted to balance out the tunneling and leakage current. The output adapts to the changes on the floating node so that it can return to the mid of the rail slowly.

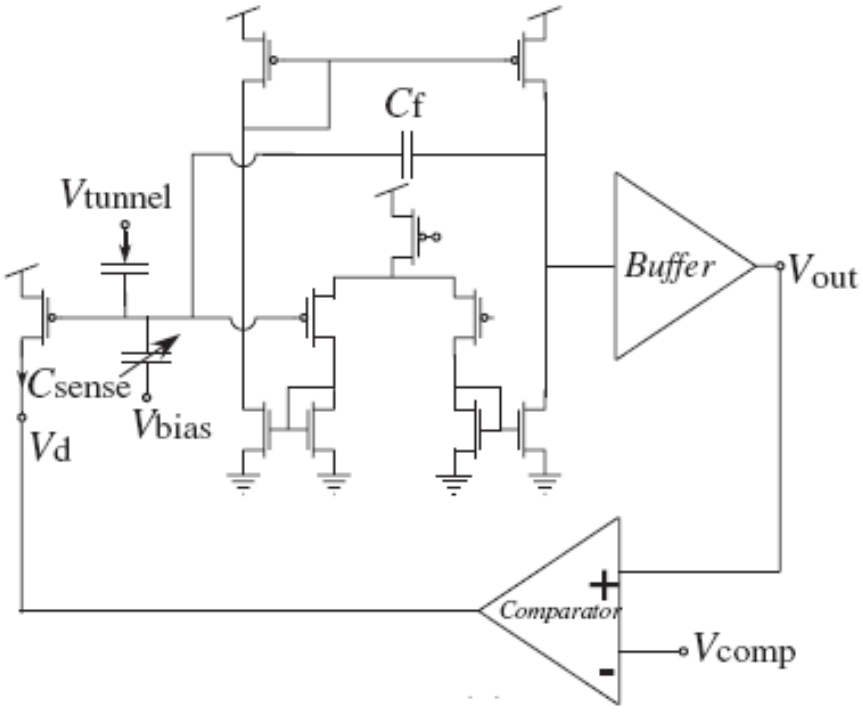

Figure 4.6: Integrated auto-zeroing capacitive sensing amplifier [90].

This adaptation scheme was used with a capacitive micromachined ultrasonic transducer (CMUT) in [90]. Comparison of the noise spectrum with the CMUT sensor showed no significant degradation in the noise performance due to the tunneling and injection mechanism. Additionally, the power consumption from the comparator and the injection transistor is in the µW range. Unlike many charge amplifier circuits where output noise and SNR is set by the load capacitance (kT/C thermal noise), this scheme allows for lower drawn capacitance for a given noise floor. Improving the linear range of this amplifier, simultaneously improves the SNR of the amplifier.

4.3 CHARGE AMPLIFIER NOISE ANALYSIS

The output-referred noise power for the capacitive charge amplifier circuit in Section 4.1 can be calculated from its small signal model for noise analysis as shown in Figure 4.7.

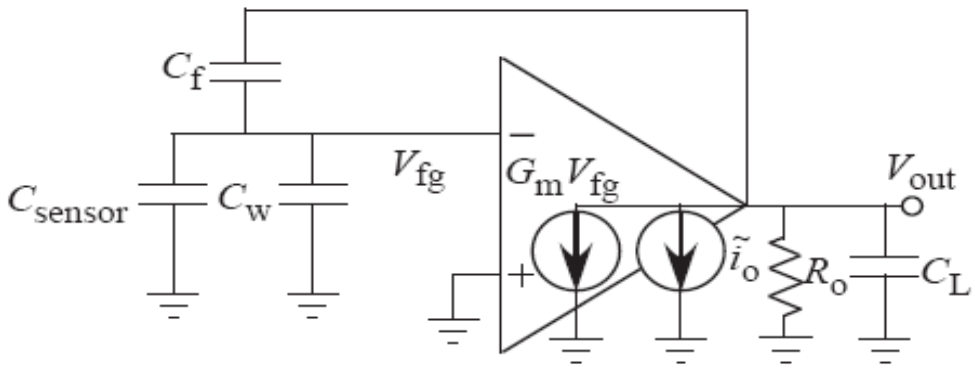

Figure 4.7: The small-signal model of (Figure 4.3) for noise analysis [90]

In terms of the amplifier output current noise $\bar{i}_o$, the thermal noise component can be modeled as [90]:

$$\frac{\bar{i}_o^2}{\Delta f} = \frac{2}{\kappa} nqU_T g_m \tag{4.5}$$

where κ is the subthreshold slope coefficient of the transistor, n is the effective number of noisy transistors, q is the charge of an electron, U_T is the thermal voltage, and g_m is the transconductance of the transistors. The total output voltage noise power can be expressed as

$$\hat{V}_{out,total}^2 = \frac{nqU_T}{2\kappa} \cdot \frac{C_{sensor} + C_w}{C_L C_f} \tag{4.6}$$

The expression for the SNR is given as

$$SNR = \frac{8U_T}{\kappa nq} \cdot \frac{(C_{sensor} + C_w)C_L}{C_f} \tag{4.7}$$

Based on (4.7), increasing C_w improves to the linear range of the capacitive sensing amplifier, while increasing C_w or C_L affects the dynamic range. By using a floating node in the capacitor feedback amplifier scheme, the circuit is more sensitive and the SNR is improved by the product of the load and the sum of the input and parasitic capacitors.

The gain of the amplifier and the bandwidth of the circuit are both infinite. In reality, the amplifier has a finite gain, and to save power, the operating frequency is within the range of the bandwidth. The dynamic range of a circuit is a ratio of the maximum possible linear output swing ($\Delta V_{lin,max}$) to the total output-noise power. The expression for the dynamic range is given by $\Delta V_{out,max}$ which is defined as [90]

$$\Delta V_{out,max} = \frac{C_T}{C_f} \cdot \Delta V_{lin,max} \tag{4.8}$$

where $C_T = C_{sensor} + C_w + C_f$. The dynamic range varies inversely with C_f; therefore a high-gain amplifier will have a larger dynamic range than will a low-gain amplifier for the same values of C_{sensor} and C_w.

4.4 EXCITATION AND DETECTION

The RIE sensor has to be brought into vibration and the vibration has to be detected, so the choice of excitation and detection technique is of great importance. In this case, the RIE sensor is excited electrostatically and the resonance condition is detected by monitoring the displacement current that results from the air gap capacitance change between the electrodes and the vibrating structure.

Several other detection techniques are available from which one can choose, including interferometry and reflectometry. A brief description is given and illustrated in Figure 4.8 below:

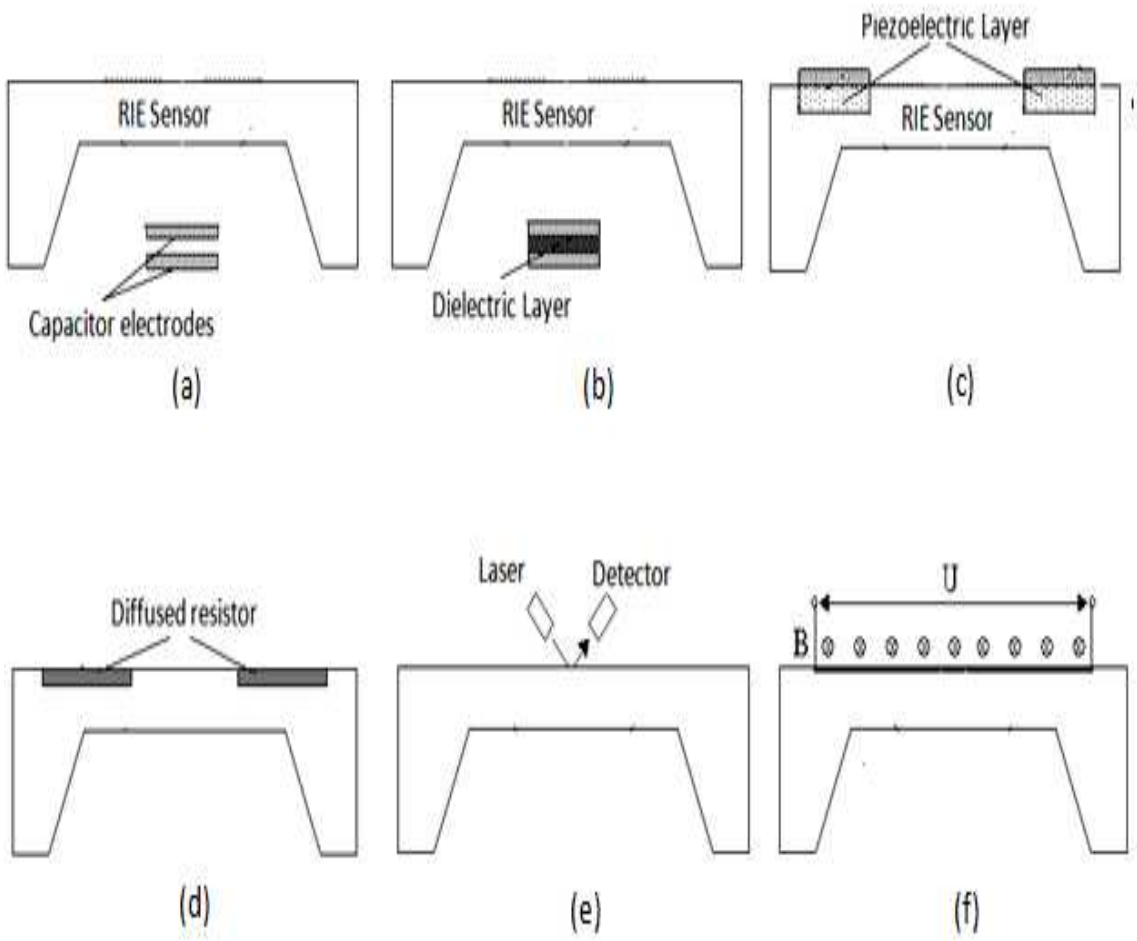

Figure 4.8: Different vibration detection schemes: a) capacitive, b) dielectric, c) piezoelectric, d) piezoresistive, d) optical, e) magnetic

1) *Capacitive detection*. This technique requires two electrodes arranged in close proximity to the vibrating structure. If the structure moves, the capacitance changes, which is detected electrically. It is a very attractive method because it provides a linear output when the vibrational amplitude is small and not sensitive to external conditions such as, temperature

changes. However, the air gap situated between the vibrating structure and electrodes provides a large damping force on the sensor and decreases its quality factor.

2) *Dielectric detection*. This technique uses a sandwich structure consisting of a thin dielectric layer between an upper and lower electrode. The movement of the structure will change the thickness of the dielectric layer, which in turn changes the capacitance. Since the permeability of a dielectric material is usually temperature dependent, this technique cannot be used if the device should operate in a wide temperature range.

3) *Piezoelectric detection*. A piezoelectric material, like single crystalline quartz, has built-in dipole charges. When it is exposed to stress the electrical characteristic of the material changes, which can be utilized for vibration detection purposes. Unfortunately, silicon is not piezoelectric, so a layer of another piezoelectric material should be deposited on the resonator. An often used, highly piezoresistive material is ZnO, but it is not a standard material in IC fabrication technology.

4) *Piezoresistive detection*. Integrated resistors can be used also for vibration detection since their resistivity changes due to the presence of stress in a material. An advantage of this technique is that it is quite easy to fabricate the resistors using standard IC processing steps and silicon has large piezoelectric coefficients. The main drawback of this method is large temperature sensitivity of the resistors.

5) *Optical detection*. There are two main types of optical detection techniques: interferometric

and amplitude modulation. The amplitude modulation method is simpler, but less sensitive. Optical detection techniques are mostly used in vibration characterisation setups because they are quite bulky. The main advantage of this technique is that it does not influence or degrade the vibration. However, this setup is difficult to integrate on a silicon chip.

6) *Magnetic detection*. The vibration of a conductor in a magnetic field creates an induced voltage. This can be used for vibration detection purposes. Despite the simplicity of this technique, it is quite rarely selected. This can likely be attributed to the small output voltage if a weak magnetic field is present.

Electrostatic excitation and capacitive detection presents many advantages, among them low power consumption and IC compatible technology. Although the other techniques are more sensitive, the possibility of integration with control electronics makes the capacitive detection technique very attractive to use. The capacitive interface sensing circuit is very well suited to the RIE etch rate application because when there is no external electric field, the RIE sensor will not vibrate due to the lack of excitation, thus the corresponding capacitance change will also be zero. The insensitivity of the capacitive sensing method to temperature changes is also a very positive feature. The one disadvantage is that this type of detection provides a nonlinear response at large vibrational amplitudes.

The force that the capacitive excitation method would apply to the RIE sensor was derived in [68] and is given by

$$F_{Drive} = \frac{1}{2}(V_{DC} - v_{ac})^2 \frac{\partial C}{\partial x} \tag{4.9}$$

where C is the capacitance, V_{DC} is the DC bias across the excitation gap and v_{ac} is the AC voltage across the excitation gap. It is important to note that when the RIE sensor is capacitively actuated, both an AC and a DC voltage are applied. Assuming the AC voltage can be represented as a time varying function, ($v_{ac} = V_{ac} \cos \omega t$), the drive force is given by [68]:

$$F_{Drive} = \frac{1}{2}\left[V_{DC}^2 + \frac{V_{ac}^2}{2} - 2V_{ac}V_{DC}\cos(\omega t) + \frac{V_{ac}^2}{2}\cos(2\omega t)\right]\frac{\partial C}{\partial x} \tag{4.10}$$

From this expansion it can be seen that with no applied DC voltage, the output force would only be a component of the input signal. To obtain a large force at the fundamental frequency of actuation, a large DC voltage in conjunction with a small AC signal is applied. In addition, if the input signal frequency is at the natural resonating frequency of the platform, the output signal will be magnified by the quality factor of the RIE sensor.

4.5 INTEGRATED RIE SENSOR AND INTERFACE CIRCUIT

The change in capacitance of the RIE sensor is directly related to the output voltage of the charge amplifier. A model was developed to investigate whether the small scale deflections of the RIE sensor platform, and the small current signals that are used to locate the resonant condition, will be properly sensed and amplified by the charge amplifier circuit. The integrated

charge amplifier circuit with the RIE sensor at the input (Figure 4.9), was modeled using NI-Multisim electronic schematic capture and simulation program.

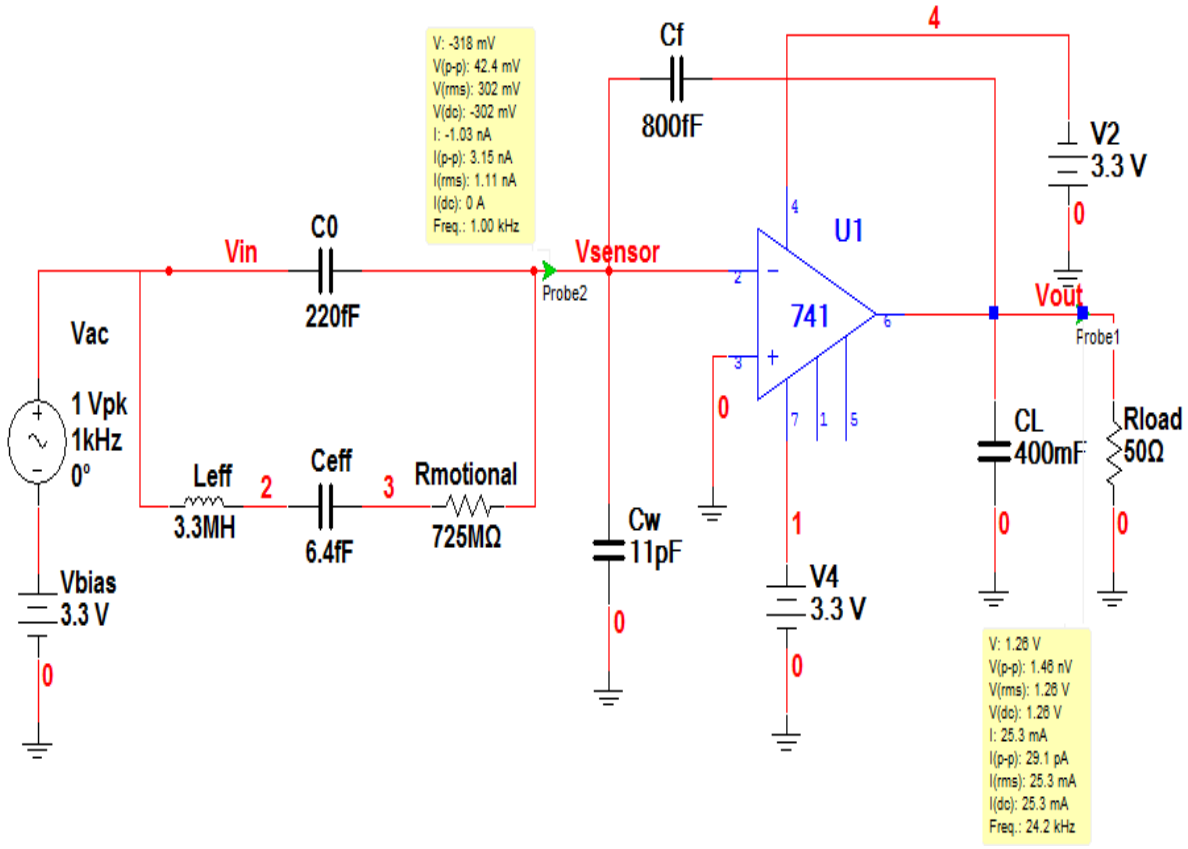

Figure 4.9: NI-Multism model of integrated RIE sensor and charge amplifier circuit.

The RIE sensor is replaced with its equivalent circuit and nominal impedance values that was discussed and calculated in Chapter 3. The static capacitance C_0 represents the capacitance of the air gap. The $R_{motional}L_{eff}C_{eff}$ series branch represents the motional behavior of the platform associated with the fundamental mode. The LM741 series operational amplifier is an

ideal op-amp, and is used to approximate the behavior of the charge amplifier interface circuit. If one assumes an ideal op-amp characteristic the expected voltage response of the integrated charge amplifier capacitive sensing circuit then follows (4.1).

Figure 4.10 shows the response of the integrated charge amplifier interface circuit to a $1V, 1kHz$ sine wave, offset by $3.3V$ that is superimposed on an input of the RIE sensor. The output voltage at the charge amplifier interface circuit is $1.2Vrms$, and the output frequency is $24.4kHz$.

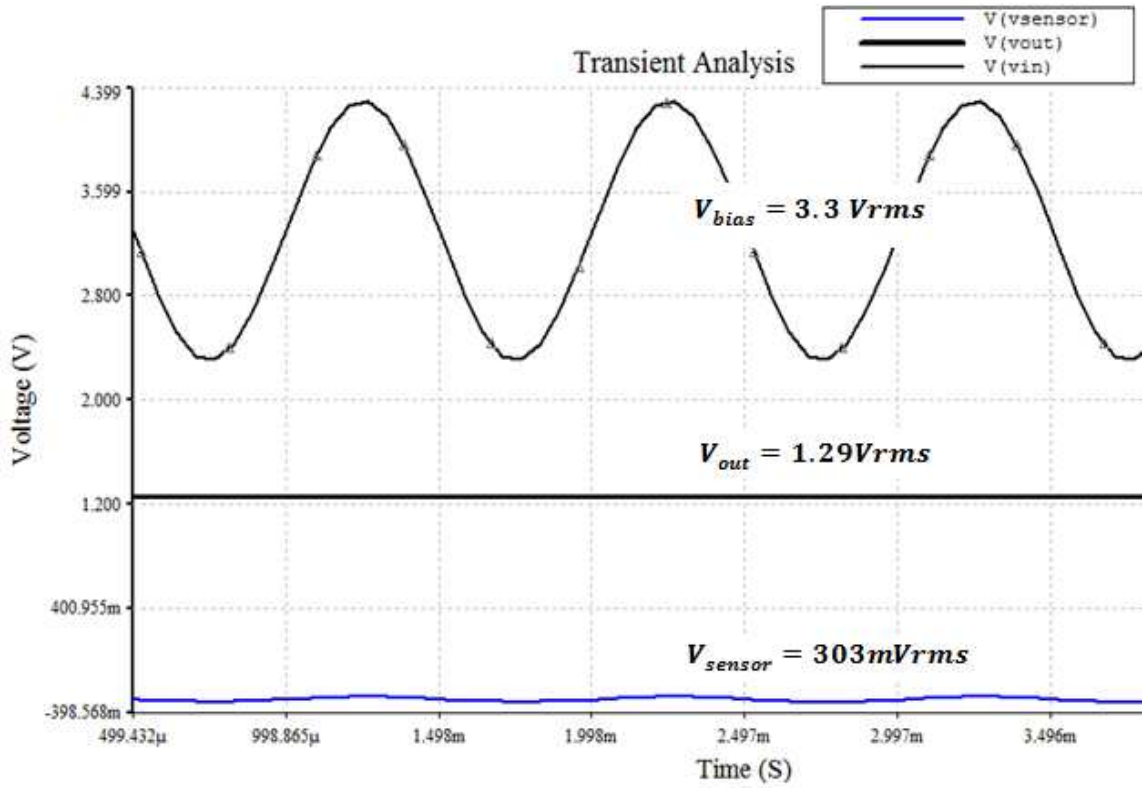

Figure 4.10: Voltage waveforms of integrated RIE sensor and charge amplifier circuit.

From the voltage waveform it appears that the unique integrated RIE sensor implementation results are consistent with what is expected from this charge amplifier interface circuit. The results of the transient analysis simulations are summarized in Table 4.1.

Table 4.1: Integrated RIE sensor and charge amplifier circuit simulated results.

Circuit Parameters	***Value***
V_{AC}	$1V, 1kHz$
V_{bias}	$3.3V$
C_0	$220fF$
C_f	$800fF$
C_W	$11pF$
C_L	$400mF$
V_{out} $Calculated$ (4.1)	$0.907Vrms$
Simulated Results	***Value***
V_{out} I_{out}	$1.29Vrms$ $25.3mArms$
V_{sensor} I_{sensor}	$300mVrms$ $1.11nArms$
$Output\ Frequency$	$24.4kHz$

4.6 SUMMARY

The integration of sensors and electronic circuitry is a dominant trend in the semiconductor industry, and much work and research has been devoted to this effort. The RIE sensor relies on capacitive transduction to detect small capacitance changes and the resulting change in resonant frequency during the RIE process. The RIE sensor's overall performance is limited by the interface circuit, and integration with the proper circuit allows the RIE sensor to function as a highly sensitive measure of etch rate during the RIE process.

A capacitive feedback charge amplifier circuit, when configured with the RIE senor at the input, achieves high sensitivity of capacitance changes by choosing a large value of of V_{bias} and a small value of C_f. By using a floating node in the capacitor feedback amplifier scheme, the circuit is more sensitive and the SNR is improved by the product of the load and the sum of the input and parasitic capacitors. The charge amplifier interface circuit offers the potential for wide dynamic range, high sensitivity, and high stability, along with an output for easy interface to digital circuitry.

CHAPTER 5

5.1 RESEARCH CONTRIBUTIONS

This research explores the design, operation, fabrication and integration of a novel *in-situ* RIE etch rate monitoring and endpoint detection system that incorporates an integrated micromachined sensor. This approach will advance the current state-of-the-art due to: 1) non-invasive sensing capability based on microsensor technology; 2) a simplified endpoint detection scheme that relies on the correlation between resonance frequency and the film thickness on the surface of the substrate; 3) dynamic feedback control during RIE and results in sharp and reliable endpoint; 4) advances RIE monitoring and diagnostics by giving process engineers more repeatable and flexible control over endpoints; and 5) a shortened process development cycle that eliminates under-etching and reduce over-etching to increase yield.

5.2 RIE SENSOR DESIGN CONSIDERATIONS

The micromachined sensor will be placed in an RIE system to monitor key figures of merit *in-situ*. One of the greatest benefits of micromachining is that the fabrication process can be made compatible with standard IC processing. Mechanical structures can thus be integrated with support electronics to yield a "smart sensor". This is the approach envisioned for RIE monitoring and control.

Figure 5.1 shows the micromachined sensor, which is the prototype designed at Georgia

Tech to assess RIE etch rate [20]. During operation, the MEMS platform is coated with the same material to be etched from the substrate and positioned above drive and sense electrodes. As etching proceeds, the sensor is excited into resonance. As the mass loading of the platform decreases during etching, its resonant vibrational frequency shifts by an amount proportional to the amount of material remaining, allowing etch rate to be inferred.

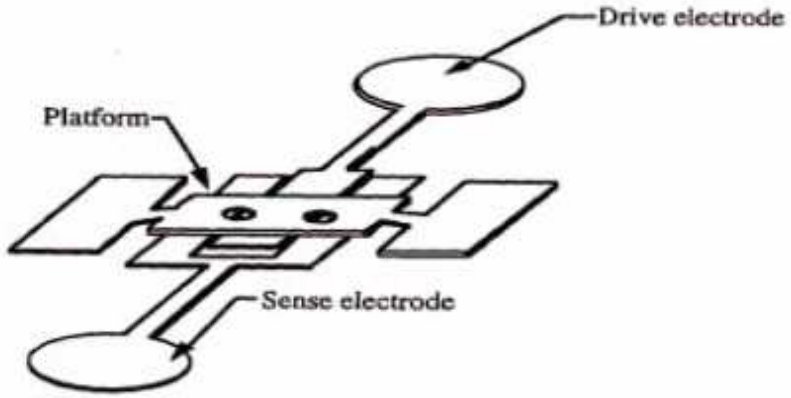

Figure 5.1: Prototype RIE sensor showing the platform suspended over electrodes [20].

The sensor consists of three major parts: the drive electrodes, sense electrodes, and vibrating platform. The drive electrode was designed such that the end of the electrode is precisely centered beneath the platform. This is very important because the location of the drive electrode will impact the mode being excited. Since we are only interested in the fundamental mode, centering the drive electrode relative to the platform is optimal. The sense electrode should be in close proximity of the drive electrode, but not touching as coupling between the two electrodes will adversely affect the performance of the sensor. The platform has maximum

displacement at its center, where the capacitance change is the greatest. This implies that not only should the sense electrode be placed near the center of the platform, but the platform should be long compared to the width of the sense electrode. A consequence of a platform that is too long is bending or buckling during operation.

The mechanical Q-factor is an important parameter in the design and operation of sensor. The platform should be designed such that the highest Q-factor can be achieved, thereby minimizing air damping and internal stress. The RIE sensor stability and performance is then almost entirely dependent on the mechanical properties of the elements. Proper placement of these elements ensures that the RIE sensor, within the process chamber, will have sufficient excitation and detection efficiency.

5.3 SENSITIVITY

Mechanical resonance obtained through electrostatic excitation and capacitive detection has implications to the overall design and fabrication of the RIE sensor. Recall that the RIE sensor is based on the doubly clamped beam design previously described in Chapter 3. In the middle of the sensor's platform, at the point of maximum deflection, where the capacitance change is greatest, the potential energy, E_p equals the total energy of vibration. The platform is subject to a bending moment and axial force, and as it vibrates it also achieves its maximum kinetic energy, E_k during the cycle.

The conservation of energy law gives another useful method, in addition to the general equations reported in Chapter 3 for determining the first resonant frequency, $\omega_1^2 = E_p/E_c$. Generally, a parameter can perturb the kinetic or the potential energy of the RIE sensor. The

sensitivity is defined as the fractional change in the unperturbed resonant frequency, ω_0 due to an incremental change in the parameter. The RIE sensor is sensitive to potential energy perturbations (e.g. mass loading of the platform), and the mode of vibration will be altered by the applied load.

Manipulation of the resonant frequency equation derived using the conservation of energy law yields the function for determining the sensitivity of the RIE sensor. The relation derived in [92] is given as:

$$S = \frac{8}{EI\pi^2} \cdot \frac{L + \frac{2}{\pi}\sin\left(\frac{\pi L}{2}\right)}{L - \frac{2}{\pi}\sin\left(\frac{\pi L}{2}\right)} \tag{5.3}$$

The RIE sensor platform is composed of a metalized polyimide layer, with effective Young's modulus, E and moment of inertia, $I = Wh^3/12$, L, h and W, are the length, thickness and width of the platform respectively.

Simulating the sensitivity of the RIE sensor, as a function of the length and width, using the relation (5.3) produces the surface in Figure 5.2. The plot indicates a decrease in the sensitivity with increase in width. The sensitivity of the RIE sensor will also increase if the gap capacitance decreases, but unfortunately, this also increases the nonlinearity. One can conclude that trade-offs exists between the large sensitivity and the small nonlinearity error requirements. The only parameter which increases the sensitivity and does not increase the nonlinearity error is the length of the platform. Unfortunately, this parameter cannot be increased without limit, because large value would degrade some other important mechanical parameter such as degree

of freedom and degrade the suppression of the higher order modes.

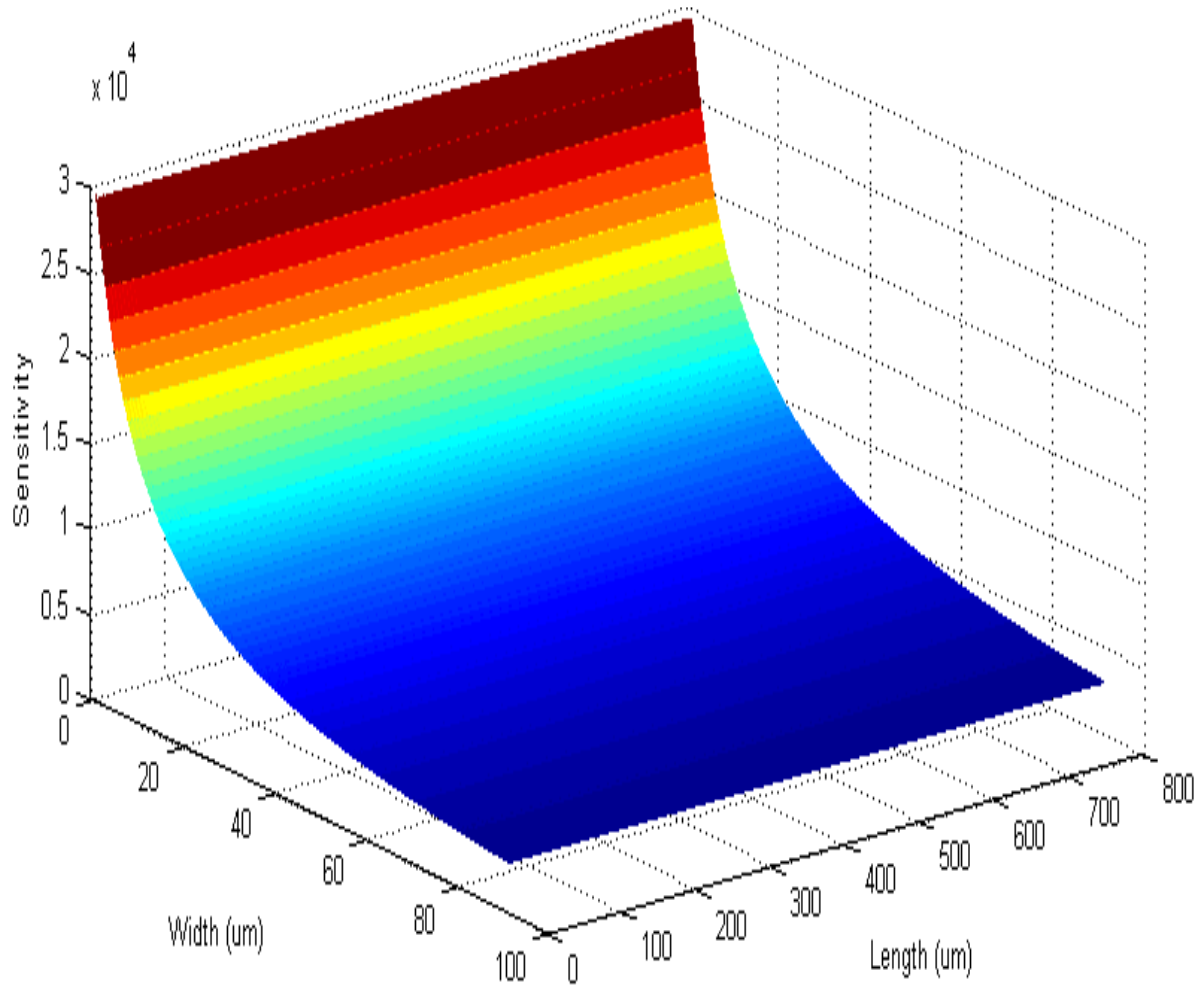

Figure 5.2: Sensitivity of the RIE sensor as a function of the length and width

5.4 FINITE ELEMENT ANALYSIS

The design of the RIE sensor was further analyzed and optimized by finite element analysis (FEA). This computer-based numerical technique for calculating the strength and behavior of engineering structures was conducted using ANSYS 7.0. With the ANSYS model, we were able to simulate deflection, stress, vibration and other phenomena. The MEMS structure was deformed and examined to establish the relationship between applied loads and deflections. A static ANSYS simulation of the RIE sensor yielded a fundamental frequency of 40.7 kHz, which is within the desired range. We were also able to verify the expected correlation between the platform height and its resonant frequency.

Steady state, transient and random vibration behavior was also analyzed to study the effects caused by the applied load to the sensor. Boundary conditions were employed to indicate where the structure was constrained and restricted against movement or in the case of our symmetric RIE structure when only a portion of the sensor needed to be modeled.

The RIE sensor is composed of a polyimide platform 700 µm long and 140 µm wide that extends 4 µm above drive and sense electrodes. The thickness of the polyimide platform is 6.5 µm. On top of the polyimide platform is a layer of gold that is 0.5 µm thick. The platform was modeled as a uniform beam with both ends clamped and suspended above a ground plane. The ANSYS parameters are given in Table 5.1 below.

Table 5.1: ANSYS parameters for RIE sensor model

ANSYS Parameter	Value
Platform length	700μm
Platform width	140μm
Platform thickness	6.5μm
air gap	4μm
Polyimide Young'sModulus	8.3GPa
Polyimide density	1400 kg/m^3
Poisson ratio	0.34
Gold Young'sModulus	78GPa
Gold density	19300 kg/m^3
Element Type	Beam 3
2D	Quad 4 node plane 42
3D	Brick 8 node solid 45
Coupled field element	TRANS 126

The sensor was first modeled and meshed using a 2-D element type, and then extruded into the 3-D model shown in Figure 5.3. We obtained the profile of the first three mode shapes and resonant frequencies and found that the fundament and harmonics were within the expected range. The mode shapes are illustrated in Figure 5.4 and the results are summarized in Table 5.2.

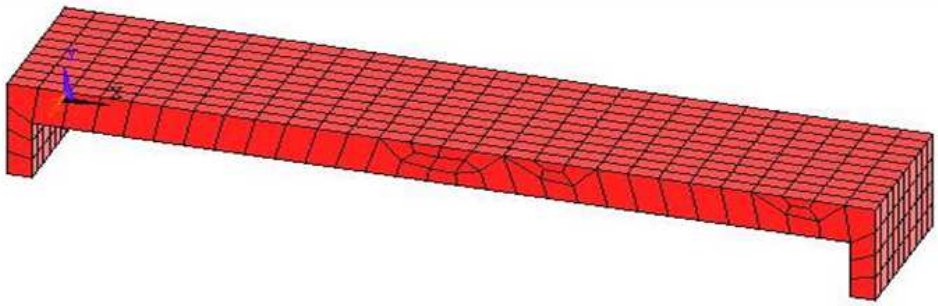

Figure 5.3: 3-D meshed model of RIE sensor

Table 5.2: RIE sensor resonance frequencies

Harmonics	*Resonance Frequency*
f_1	40.7 kHz
f_2	110.9 kHz
f_3	217.5 kHz

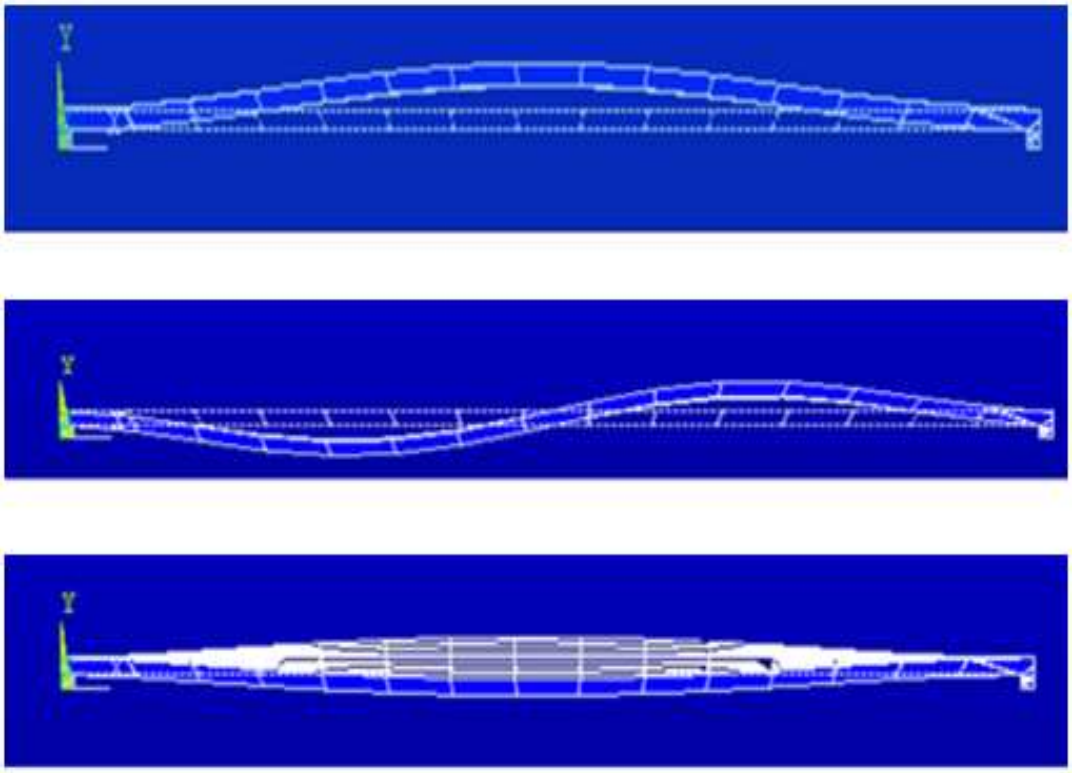

Figure 5.4: RIE sensor mode shapes for first 3 harmonics

5.4.1 Harmonic Analysis

The harmonic analysis gives us the ability to predict the sustained dynamic behavior of the RIE sensor enabling us to verify whether or not the sensor design will successfully overcome resonance, fatigue, and other harmful effects of forced vibrations. We used the mode superposition method that uses the natural frequencies and mode shapes to compute the response to a sinusoidally varying forcing function.

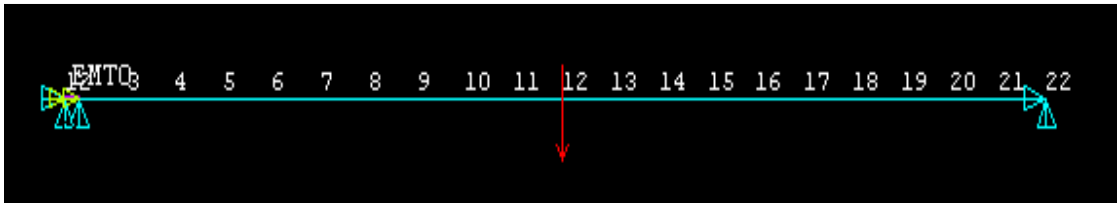

Figure 5.5: RIE sensor modeled using the elastic beam element

To confirm the expected response of the sensor, an electrostatic force was applied. The application of a range of voltages between 10-100 volts caused the platform to deflect. The resonance frequency and displacements varied with the application of the load. As already noted, the resonance frequency is a function of polarization voltage, and decreases with increasing voltage. Increasing the voltage creates a larger electrostatic force between the platform and the electrodes and causes the beam to deflect. Figure 5.6 show that the platform had its maximum deflection at the center, as expected, with a maximum displacement of 0.03216 µm.

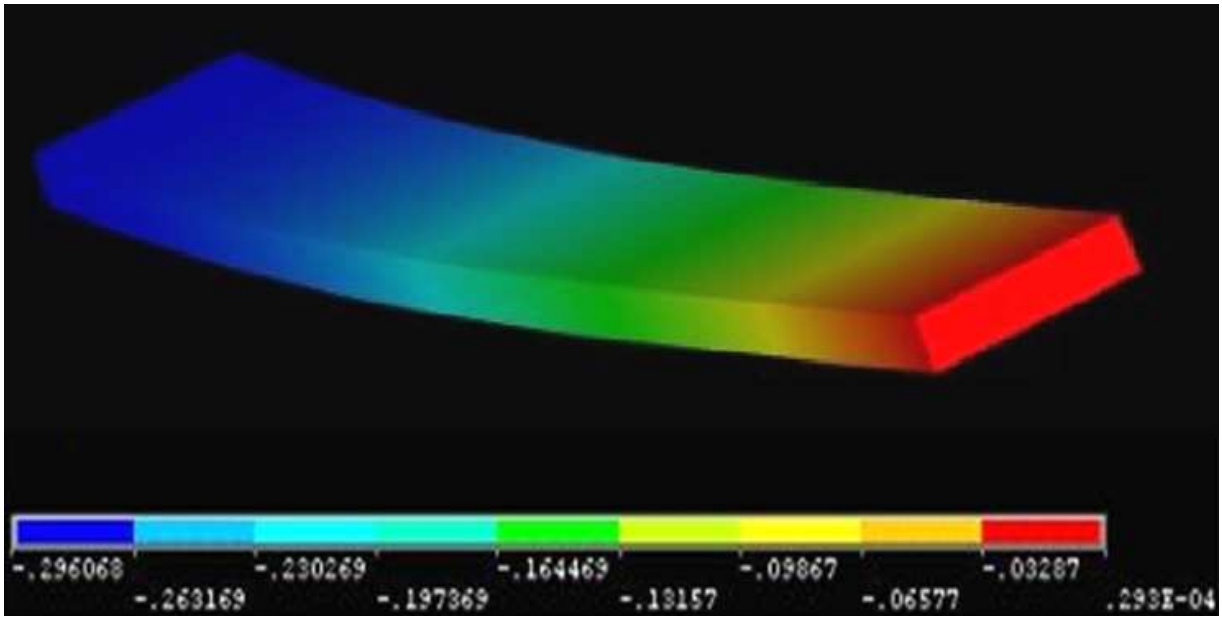

Figure 5.6: RIE sensor displacement plot showing maximum displacement of 0.032 µm

Changes in the mass loading of the platform and changes in film thickness that occurs during etching are simulated by varying the height of the platform. This produces a change in the capacitance between the platform and electrodes, which results in the change in the resonant frequency of the structure. The gap capacitance increases as material is etched since there is reduced bending in the middle of the beam due to its own weight. When the height of the platform increased, the resonant frequency shifts to the right on the frequency spectrum and vice versa.

The frequency spectra in Figures 5.7 and 5.8 (for two cases), illustrate how changing the height of the platform from 3.5µm to 7µm affected the resonance frequency. The 3.5µm thick platform has a resonance frequency of 20.45 kHz, and the resonance frequency was 35.65 kHz for a 7 µm thick platform.

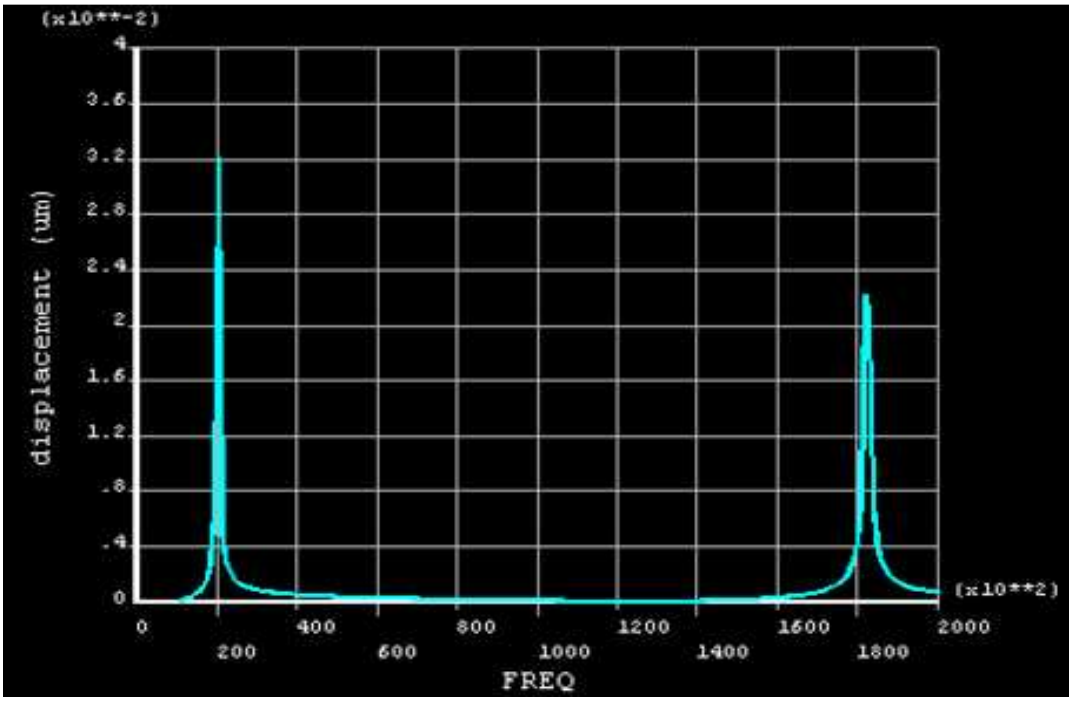

Figure 5.7: Resonance frequency f_1 = 20.45 kHz when the platform height = 3.5 µm.

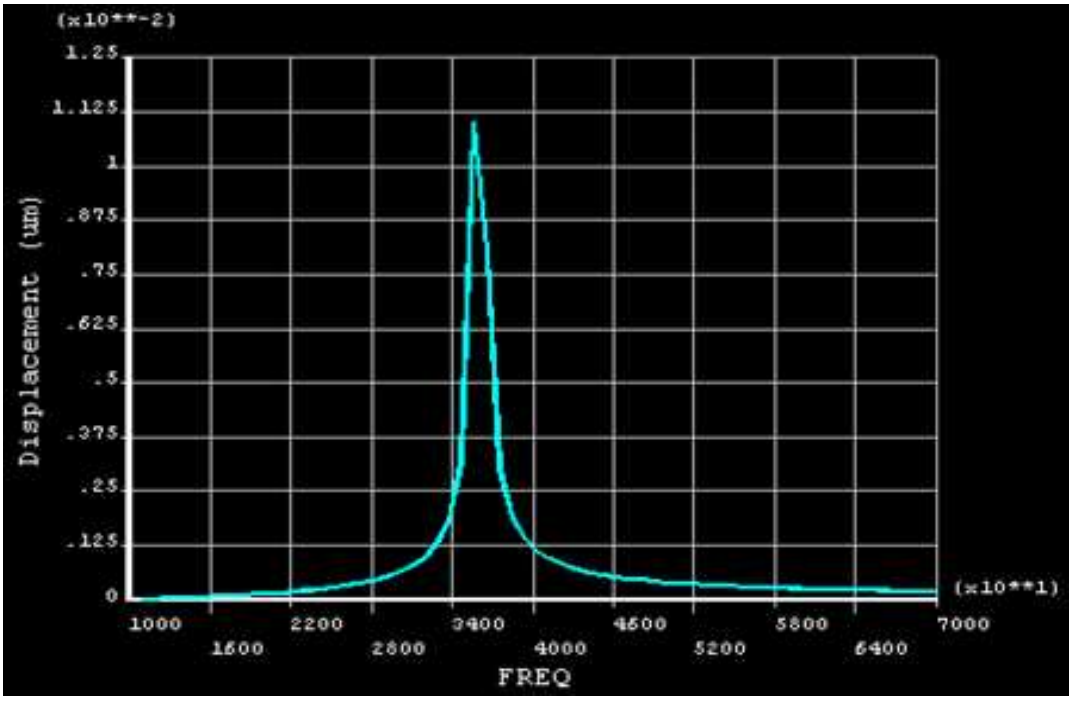

Figure 5.8: Resonance frequency f_1 = 35.65 kHz when the platform height = 7 µm.

Doubling the thickness of the platform does not cause a doubling of the resonance frequency. The thickness variation however, has a quadratic and interaction effect on the resonance frequency. Based on the results of the simulation, a direct correlation of platform height (film thickness) and resonant frequency is evident, potentially providing the desired mechanism of the RIE sensor for real-time monitoring of the wafer state during etching.

5.4.2 Coupled Field Analysis

The RIE sensor's platform is modeled as a 3-D beam that is positioned 4µm above the drive and sense electrodes, represented by the ground plane. An applied voltage coupled to the beam causes the beam to deflect and change the air gap between the beam and the ground plane (Figure 5.9).

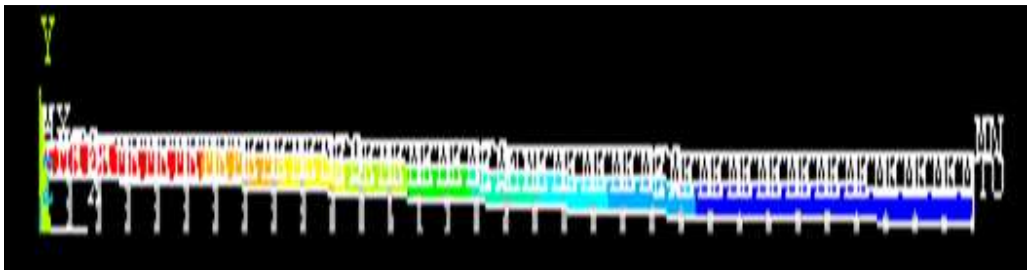

Figure 5.9: Coupled electrostatic beam above ground plane

A plot of the air gap capacitance versus applied "bias" voltage provides insight into the stability of the sensor. Figure 5.10 shows that the device appears to be well behaved, since it exhibits a nearly linear dependence on the applied voltage for voltages below approximately

40V. The variance in the capacitance represent the effects of the mass loading of the RIE sensor platform. As the mass loading decreases during etching, the gap between the platform and electrodes increases which reduces the coupling capacitance. Recall also that the resonance frequency of the RIE sensor is affected by the applied "bias" voltage. As the applied voltage increase, the resonant frequency decreases.

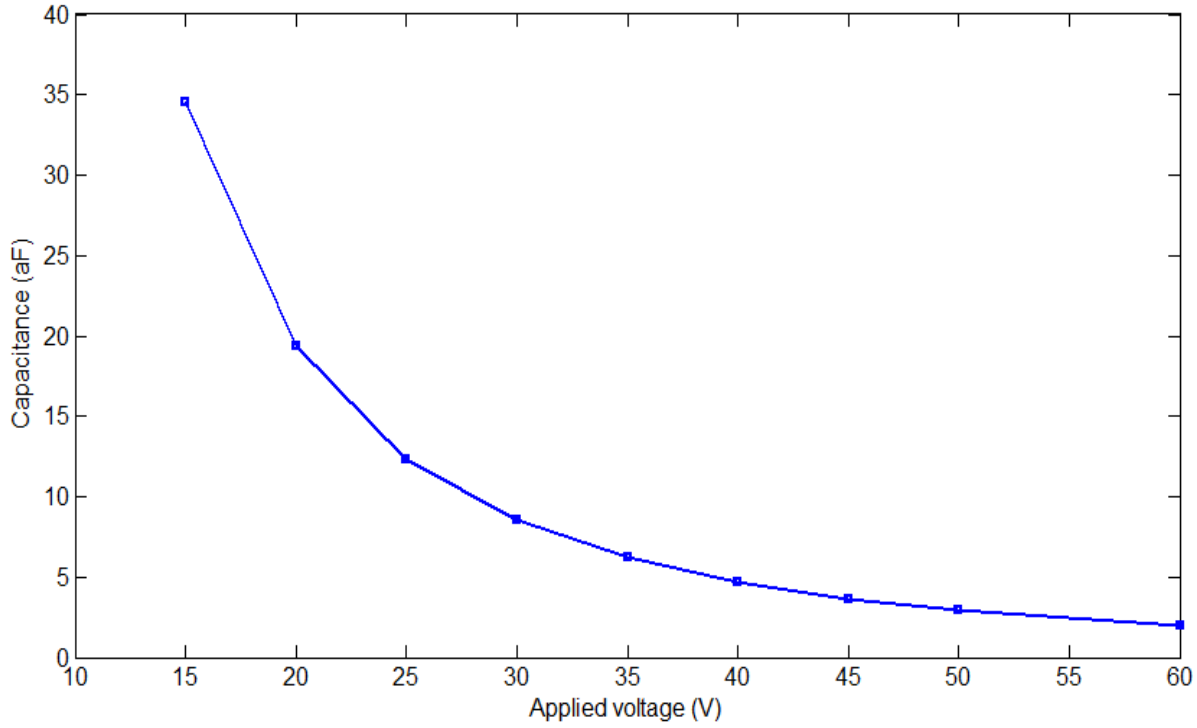

Figure 5.10: RIE sensor applied voltage vs. capacitance

5.5 SUMMARY

Preliminary design of a MEMS sensor for RIE monitoring has been conducted and verified using Matlab and ANSYS. The simulation was important for the practical realization of the RIE sensor and results confirmed the theoretical model. Using the general theory describing the model of the vibration of the clamp-clamped bridge, the range of the resonance frequency was obtained which is important for the signal detection cicuit and the range of sensitivity. One can conclude from these results that trade-offs should be made between the large sensitivity and the small nonlinearity error requirements. The only parameter which increases the sensitivity and does not increase the nonlinearity error is the length of the platform (L). There may also be potential advantages in minimizing the platform width or varying the platform height.

Overall, the sensor design appears to be feasible. The relationship between the height of the platform and resonant frequency has been established. Optimization of the design will result in the best properties for the minimum cost and impact future fabrication processes. The successful development of this sensor could lead to significant productivity enhancements in the RIE process.

CHAPTER 6

6.1 DEVICE FABRICATION

This research utilizes MEMS development techniques based on a number of tools and methodologies that are used to fabricate extremely small mechanical devices and electronics on the same chip: “integrated microsystems”, with dimensions in the micrometer scale. A significant part of the technology has been adopted from integrated circuit (IC) technology. For instance, almost all devices are fabricated on silicon wafers, the structures are realized in thin films materials, and they are patterned using photolithographic methods. There are, however, several processes that are not derived from IC technology. The three basic building blocks in MEMS technology are thin film deposition of materials, mask patterning on top of the films by photolithographic imaging, and selectively etching of the thin films.

The RIE sensor fabrication process is a structured sequence of these basic operations using surface micromachined technology. As previously mentioned, the advantage of using surface micromachined technology is that thin layers of structural and sacrificial material can be deposited and patterned inexpensively to create the micro mechanical sensor. The RIE sensor consists of three major parts: the drive electrode, the sense electrode, and the platform itself. The sensor was designed such that the electrodes are precisely centered beneath the platform, which is important because the location of the drive electrode will impact the mode being excited. The platform has maximum displacement at its center, where the capacitance change is greatest. As a result, the electrodes are placed in close proximity but isolated from the platform by utilizing a

sacrificial layer. At the end of processing, the sacrificial material is removed, yielding the completed RIE sensor that is then integrated with electronics.

6.2 RIE SENSOR LAYOUT

The RIE sensor requires a mask to be made for each patterning step of the process. A mask is a two-dimensional design representation that will be patterned and etched into the substrate. Bulk machining typically requires a minimum number of masks, usually only one or two.. Surface micromachining can require as many as 14 masks to produce a complex MEMS device that may have complicated patterns such as spirals, jagged edges, and other structures. Additionally, small design features make MEMS mask design more challenging and requires an in-depth understanding of mask making process, photolithography and exposure tools.

Figure 6.1 shows the mask data preparation path between the CAD layout tool (such as AutoCAD, Cadence, or others) and the GDSII, or DXF format required by the mask supplier located Georgia Institute of Technology Microelectronics Research Center. Clear and opaque pattern (on quartz or glass) masks are created from the layout data, including the data preparation. The mask plates are made in two different types: dark field and clear field which represents the pattern on the mask. The fabrication process sequence, exposure tools and materials determines which mask field type is used. A square pattern on the dark field mask will result in a black square pattern with all other area transparent. This pattern will be transparent to light and other area will be opaque. Photoemulsion is a material that acts as an opaque (nontransparent to UV radiation) part of the mask. Photoemulsion is inferior to chrome, also

used for the same purpose, due to lower optical density (thicker film needed to block off UV radiation) and grainy structure (not as sharp edges as in the case of chrome).

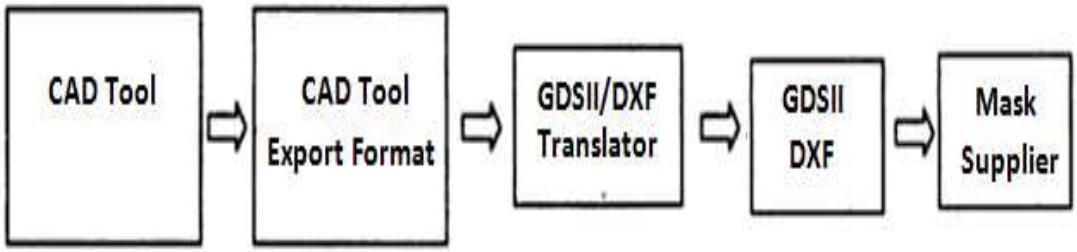

Figure 6.1: RIE sensor mask preparation flow

Four masks plates were used in the fabrication process of the RIE sensor. Mask 1 (Figure 6.2(a)) defines the drive and sense electrode, Mask 2 (Figure 6.2(b)) defines the sacrificial layer and air gap below the platform. Mask 3 (Figure 6.2(c)) and Mask 4 (Figure 6.2(d)) define the platform and the vias for electrical testing. The masks described above were made using emulsion plating on glass.

The sacrificial layer process, however, requires chrome-on-quartz for Mask 2. The exposure requirements, resolution and depth of focus of light passing through the sacrificial material are tightly controlled with Mask 2. Blank quartz plates are supplied by mask vendors and chromium can be deposited and patterned using an emulsion maskplate. The details of the chromium-quartz Mask 2 process sequence are described as follows:

1. Deposit chromium (1000 Å) by e-beam evaporation onto the quartz substrate.
2. Spin coat with photoresist. Resist may be either positive or negative acting. Soft-bake in an oven or hot plate.
3. Expose the chrome-on-quartz mask.
4. Develop and rinse mask.
5. Etch chromium in chrome etch and rinse.
6. Strip resist in solvent, rinse and dry mask 2.
7. Inspect for defects, features and placement.

If the mask is not properly developed, the chrome is removed and the process is repeated.

6.3 SUBSTRATE PREPARATION

The substrate for the RIE sensor is an undoped <100> 4” silicon wafer. If doped silicon wafers are used, this may create electrical characteristics that may compromise the performance of the sensor. The wafers are first cleaned using an RCA cleaning step that is performed before the high temperature processing begins. It involves the removal of organic and ionic contaminants, as well as the removal of the thin oxide layer that is present on the wafers.

After cleaning the wafers, they are dried in pure nitrogen and loaded in the plasma enhanced chemical vapor deposition (PECVD) machine for oxide growth. The PECVD system reacts gases SiH_4 (2% in N_2) and N_2O, in a RF induced plasma to deposit the fairly high-quality oxide film on the wafer substrate. An alternative to using PECVD is thermal oxide growth at high temperatures from (800°C - 1200°C) using either a "Wet" or "Dry" growth method.

Wet oxidation uses hydrogen/oxygen steam to accelerate oxide growth and can produce a thick oxide 2,000-24,000Å. As the oxide grows, the rate of growth slows down, because as more oxide is present on the surface of the silicon it takes longer for the oxygen atoms to penetrate the wafer surface and combine with silicon atoms to form more SiO_2. Any additional oxide must be grown at elevated temperatures. A dry oxidation produces a more uniform and denser thermal oxide with even higher dielectric strength than wet oxide. The major difference in the growth of wet and dry oxide is the growth rate. Dry oxide grows much slower than wet oxide and for this reason dry oxides normally do not exceed 1000Å in thickness.

The PECVD oxide deposition rate at 250 °C is 580 Å/min and the process took approximately 20 minutes to deposit 1µm of oxide. The thickness of the oxide was measured and verified, with a Plas-Mos ellipsometer, and it was approximately 9800Å and the wafer substrate appeared pink with a blue-green tint. The wafers were then placed in a properly sealed container in preparation for the first metal deposition that defined the drive and sense electrodes of the RIE sensor.

6.4 PROCESS SEQUENCE

The first metal layer evaporated on the substrate is titanium (Ti). The wafer was placed in substrate holder and loaded into the electron beam (E-beam) evaporator once the chamber was unloaded and vented. The chamber was closed and pumped until the pressure reaches $5x10^{-6}$ torr. At this pressure, 200Å of Ti was deposited. The Ti layer serves as an adhesion layer. A 4000Å gold layer was deposited. When patterned, this layer will serves as the sense and drive electrodes.

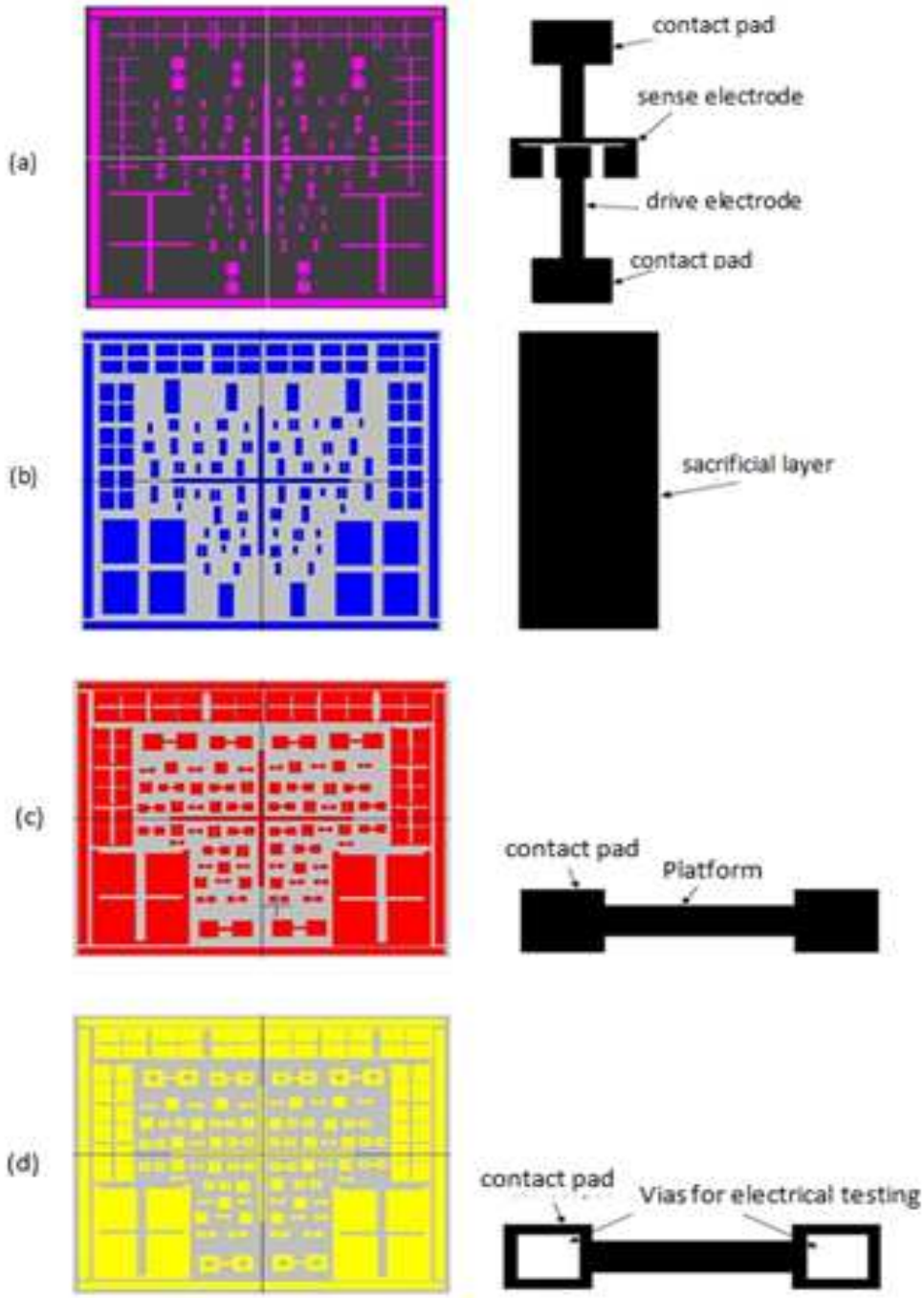

Figure 6.2: Masks used to fabricate the RIE sensor: (a) Mask 1 defines drive and sense electrode, (b) Mask 2 defines sacrificial layer, (c) Mask 3 defines the platform and (d) Mask 4 defines the vias for electrical testing.

The gold deposition rate is slow, and care must be taken to monitor the gold target as insufficient amounts of gold and improper positioning of the gun will overheat the crucible and cause damage to the e-beam equipment. The deposition time varies based on the chamber pressure, but took approximately 25 minutes at $5x10^{-7}$ torr to achieve this thickness.

Once the wafers are removed from the e-beam chamber, they were taken to the photolithography bay. HMDS primes the wafer prior to the application of the photoresist. The primer was allowed to dwell on the wafer for 10 seconds, and then spun at 3000 rpm with a ramp rate of 1000 rpm for 30 seconds. Shipley 1813 was spun on the wafers using the CEE 100CB spinner at 4000 rpm for 30 seconds. This produced a photoresist film thickness of 1.2 – 1.3 µm. The photoresist was soft baked on the hotplate for 60 seconds at 110℃ and then allowed to cool.

Mask 1 was inserted in the Karl-Suss MA-6 mask aligner and the exposure time was calculated for the current equipment setting. The exposure dose used for Shipley 1813 is 180 mJ/cm^2, and the wafers were exposed from 12 – 16 seconds at 15mW. The wafers were taken to the fume hood and developed in Shipley MF 319 developer for 55 seconds. The wafers were agitated during the development to prevent photoresist reside from remaining on the wafer. This prevented the possibility that the drive and sense electrodes would electrically short or form an air-gap capacitance.

After developing the photoresist, the wafers were hard baked at 120 ℃ for 5 minutes and allowed to cool. They were etched in a gold etchant (GE 8111) solution which has an etch rate of 30A/s at room temperature. It took approximately three minutes to etch the gold film, and the wafers were then immersed in a titanium etchant (TFTN) to remove the Ti adhesion layer. The only pattern remaining on the wafer was that of the drive and sense electrodes (Figure 6.3).

The wafer was immersed in a resist stripper to remove protective photoresist. An AMID

sequence using acetone, methanol, isoprophanol and de-ionized water is an alternative to using the resist stripper. The wafers were dried and inspected to ensure proper development of the electrodes and then readied for the sacrificial material layer process.

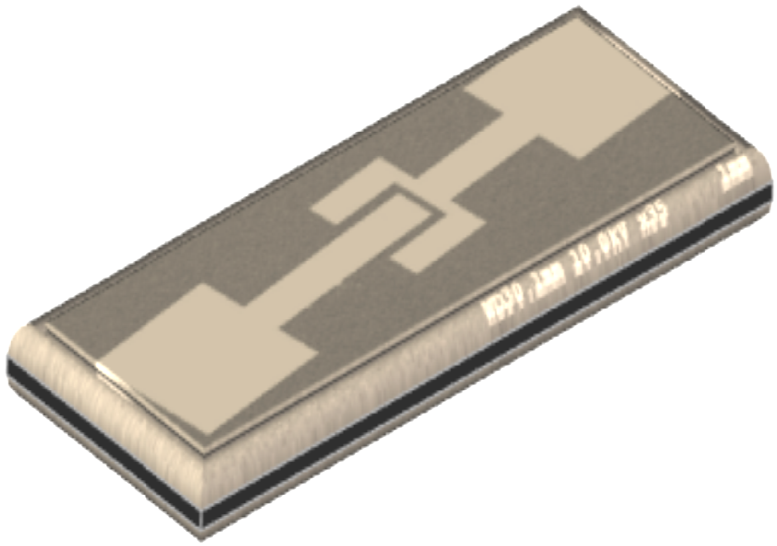

Figure 6.3: SEM image of RIE sensor drive and sense electrodes

Electrical isolation between the electrodes and the platform is critical. The isolation barrier and resulting air gap is created by utilizing a sacrificial layer material and process to develop and subsequently release the free standing sensor structure. The sacrificial layer material used was the low temperature Unity 2000P sacrificial polymer, which is an experimental material for air gap and protective overcoat applications. The Unity 2000P polymer contains photoactive compounds, and all processing was performed under yellow light. The substrate was thoroughly cleaned and dried prior to application of Unity 2000P, which is

spun on the substrate to the desired thickness. The spin curve in Figure 6.4 was utilized to attain sacrificial layer thicknesses between 2-80 microns.

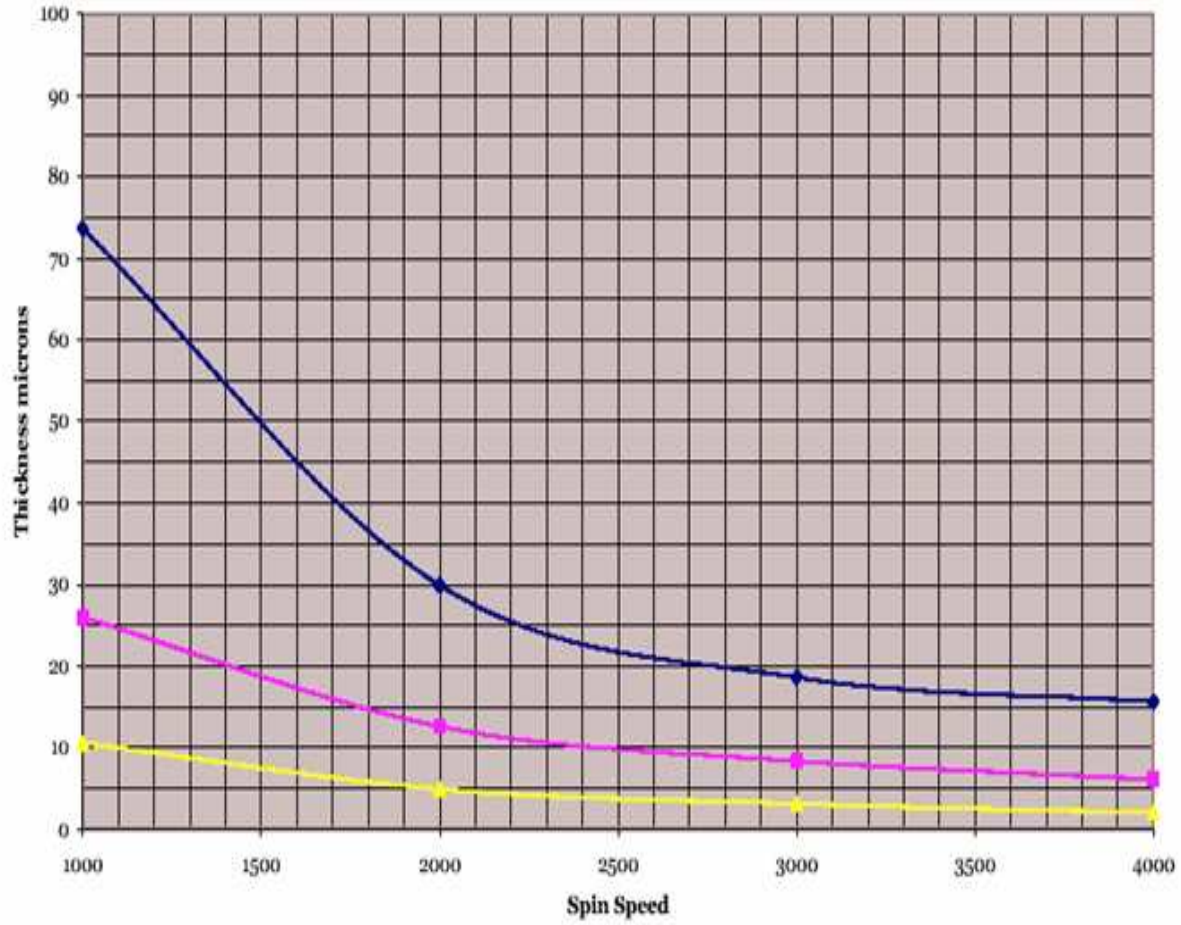

Figure 6.4: Unity sacrificial polymer material spin curve

The thickness of the sacrificial layer determined the space between the platform and the electrodes, as well as the magnitude of the voltage required to excite the platform. Typically, a sacrificial layer of 4 µm is sufficient. Low temperature Unity (lowest spin curve) was spun coated on the substrate to achieve a 4 µm sacrificial layer thickness.

The polymer coated wafer was first dehydrated at 100^{o}C on the hotplate for 10 minutes to drive off any residual solvent and provide a tack free surface. Unity 2000P is sensitive to 248 and 365 nm wavelength. The Karl-Suss mask aligner was used to expose the samples with 1000 mJ/cm^2 energy dose through the chrome-quartz mask (Mask 2). The exposed samples required a thermal treatment to develop the features in to the film. The wafers were placed on a hot plate at 110^{o}C for 15 minutes to dry develop the photo-defined features. The wafers were allowed to cool after the post exposure bake. The substrate and sacrificial polymer film was rinsed with isopropyl (IPA) that removed any residue or unexposed sacrificial polymer material.

Prior to using Unity as a clean-release sacrificial layer, the material had to meet certain requirements. A photoacid generator (PAG) was incorporated in the polymer solution in the composite material. The PAG produces an acid on irradiation to UV light. The sacrificial material decomposes in a narrower range of temperatures, leaving little or no solid residue either from the polymer or the PAG. The sacrificial material has sufficient adhesion to the substrates and the decomposition temperature of the PAG is much higher than the process-decomposition temperature of the material, thus only the UV exposed areas were selectively decomposed.

Unity is self-priming, photosensitive, and photodefinable, which permits the overcoat material to function without an additional resist masking step. The material is patterned like photoresist on I or g-line semiconductor exposure tools. There are improvements in the resolution and adhesion associated with utilizing this semitransparent sacrificial layer material, in contrast with using other sacrificial materials. A photoresist strip process was unnecessary as the exposed material is developed by heating the substrate in an oven at 110^{o}C to dry develop the photo defined features. Figure 6.5 shows the patterned and cured sacrificial polymer above the sense and drive electrodes on the surface of the substrate.

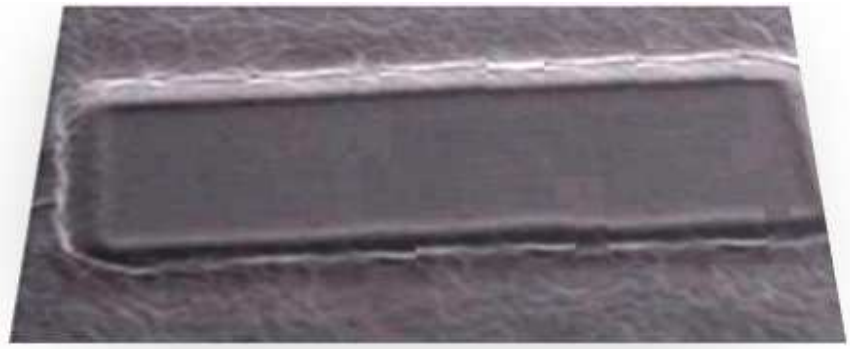

Figure 6.5: Unity sacrificial polymer over-coat above drive and sense electrode

This RIE monitoring methodology exploits the accuracy of resonant micromechanical structures, whereby shifts in the fundamental resonant frequency measure a physical parameter. A majority of these systems require free-standing mechanical movement and utilize the sacrificial layer process as the key technique to develop and release the structure on a substrate. The difficulties inherent in achieving free-standing micro-structures with the existing sacrificial materials are well documented and include lengthy deposition cycles, slow and expensive release process using hazardous materials, sacrificial thicknesses limits, and the occurrence of stiction [92−98]. The latter shown in Figure 6.6 is a well-known problem, that occurs when the device is removed from the aqueous solution after wet etching of the underlying sacrificial layer.

Various other materials that are routinely utilized as sacrificial layers to develop suspended MEMS structures were considered and compared throughout the fabrication process. Metals have traditionally been used as sacrificial materials. However, metal sacrificial layers require lengthy deposition cycles to achieve comparable thicknesses. A 16μm copper sacrificial

layer requires 5-14 hrs when coated using the CVC e-beam evaporator or DC sputterer. An additional photoresist process is necessary to pattern the metal prior to the slow and expensive etch and release process using hazardous materials. Metal sacrificial layer materials significantly increase the number of fabrication steps and lengthen the process cycle time.

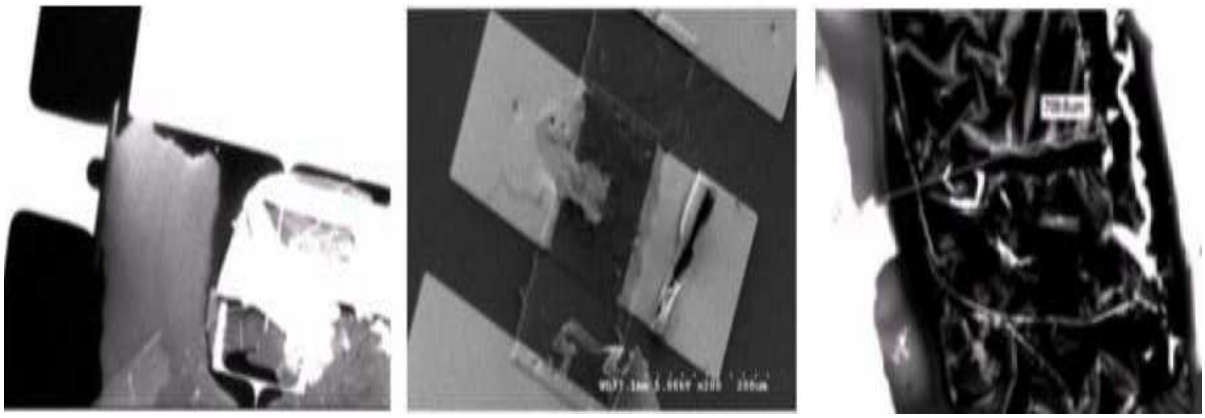

Figure 6.6: SEM images showing RIE sensor damage observed after development and release

In recent years, the trend has been towards photoresists and polyimide-based sacrificial materials. Photoresists and polyimide-based sacrificial materials are not inherently photosensitive, but can be made photodefinable with the addition of a methacrylate-based photo-polymerizable additive using an ester. Non-photodefinable self-priming polyimides, such as PI-2555, can be patterned in conjunction with a positive resist to achieve a 3.5 μm polyimide overcoat layer that serves as a sacrificial layer. Due to the precise pattern definition requirements of single mask processing, the wet etch polyimide process has a narrower process

window and needs to be tightly controlled. As a result, critical dimension control is difficult. Cured film thicknesses were limited by resolution requirements to < 3 μm. The results of the experimental comparison are summarized in Table 6.1 and illustrate why low temperature Unity 2000P was a better sacrificial material for fabricating the RIE sensor.

The wafers with the sacrificial polymer over-coat above drive and sense electrode were then taken to the DC sputterer for a second metallization layer. The DC sputterer was used to deposit the conducting layer of the platform. A 200Å of Ti and 5000Å of copper (Cu) was deposited directly on top of the sacrificial layer. It is important to sputter these metal films as, sputterer depositions tend to coat all exposed surfaces. E-beam depositions will coat surfaces facing the evaporation source, but will not coat the sides of features that are facing in directions parallel to the substrate surface. It is possible to have discontinuity in the metals at the vertical sides of the sacrificial layer.

Once the Ti-Cu is sputtered on the Unity sacrificial layer, it was patterned and exposed using Mask 3. The layer was etched in a ferric chloride copper etchant ($FeCl_3$), which was heated to 45ºC. The etch rate varied from 30- 55 Å/s. Ferric chloride is a selective etchant that does not etch gold or titanium, and the wafer will not be adversely affected if it remains in the etchant too long to ensure that all the copper is removed. The Ti adhesion layer was removed in a similar manner as before using the TFTN, etchant after which the wafer was cleaned using an AMID sequence to remove the resist.

The vibrating platform is composed of the bottom metal layer, an inner dielectric layer, and an upper metal plate. Pyralin PI-2555 polyimide was used and is a suitable material for the interlayer dielectric layer because it imidizes faster at lower temperatures. An adhesion promoter VM 651 was applied to help improve the adhesion of the polyimide to the metal layer.

Table 6.1: Experimental Comparison of Typical Sacrificial Layer Materials

Sacrificial Material	Coating Process	Development/Release Method
Photoresist S1827	Spin Coat Film Thickness: 2.5 um	Soft Bake: 90 sec / Exposure MF-319 Developer: 50 sec Hard bake: 30 min Resist Strip
Polyimide PI-2555	VM651 Primer Spin Coat Film Thickness: 3.5 um	Polyimide Soft Bake: 30 min Photoresist Overcoat & Soft Bake: 2 min Exposure / MF-319 Developer Polyimide Cure: 2 hrs Resist Strip Plasma-Therm RIE Gases: CF_4 / O_2 (PI-2555) Etch Rate: 5000 Å/min
Silicon Dioxide SiO_2 *additional photoresist masking step required	Plasma-Therm PECVD Rate: 400 Å/min	Plasma-Therm RIE Gases: CHF_3 / O_2 Etch Rate: 400 Å/min Wet Etching HF: NH_4HF:H_2O HF:HNO_3 Etch Rate: 20 Å/sec
Metals Aluminum / Copper / Chrome *additional photoresist masking step required	CVC E-Beam Evaporator Rate: 3 Å/sec (Al /Cu/Cr) CVC DC Sputterer Rate: 6.27 Å/sec (Al) 8.21 Å/sec (Cu) 6.88 Å/sec (Cr)	Plasma-Therm RIE Gases: BCl_3 / Cl_2 (Al) Etch Rate: 500-2000 Å/min Gases: Cl_2/O_2 (Cr) Etch Rate: 100-200 Å/min Wet Etching HCl/HNO3/HF 10 Å/sec (Al) H_2O/HNO_3 80 Å/sec (Cu) H_2O/H_2O_2 40 Å/sec (Cr)
Unity 2000P Sacrificial Polymer	Spin Coat Film Thickness: 2 - 80 um	Soft Bake: 15 min / Exposure & IPA Rinse Thermal Decomposition: 2 hrs

PI-2555 was spun on the wafer to achieve a 6.5-µm film thickness. The spin speed and time was determined by the spin speed curve (Figure 6.7). A bake process on a hotplate that cures the polyimide partially, and leaves the substrate dry followed.

The polyimide coating after the soft bake has minimum solubility in photoresist. At this point, the polyimide is normally either, coated and patterned with photoresist, then etched or allowed to cure in a furnace. Instead, the wafers were taken to the DC sputterer chamber where a metal layers consisting of 200Å of Ti and 5000Å of Au and 1000Å of aluminum (Al) were deposited. The deposited metal films served multiple purposes; as a metal mask for the polyimide, the Ti/Au layer is the upper metal layer of the platform, and the upper-most Al layer serves as the "test" metal film that will be etched during the RIE etch-rate monitoring experiments.

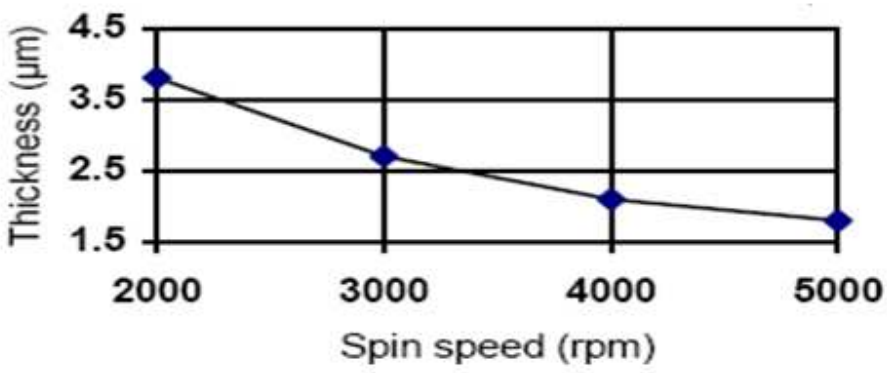

Figure 6.7: Spin speed curve for Pyralin PI-2555

The wafers were coated with photoresist as before and pattered and exposed with Mask 3. The patterned wafers were placed in aluminum etchant, followed by gold etchant (GE8111) and immersion in titanium etchant. This platform development process can take several hours to

complete, depending on outcome of each intermediate steps. Some of the issues related to wet etching have been discussed previously, and include stiction, the potential of chemical handling hazards and wafer contamination.

The resist was removed and the wafers were then taken to the photolithography bay, where photoresist was applied. Patterning and exposure of the substrate with Mask 4 defined the vias in the platform, which are necessary for electrical testing. A single immersion step using MF 354 at room temperature for 2 minutes was used to develop the photoresist and etch the polyimide. The developed wafers were rinsed and placed on the hotplate to complete the drying process. An alternative is to use the PlasmaTherm RIE system to etch the polyimide. Good results were achieved though, when the developer was heated to between 23℃ and 25℃. This accelerates the dissolution of the polyimide, while having minimal effect on the solubility of the photoresist.

The wafers were then ready to be loaded in the furnace at a temperature between ambient and 100℃ in preparation for the polyimide cure and also to thermally decompose the sacrificial material. The oven was heated to 120℃ with a $10℃/minute$ ramp and to 180℃ with a $1℃/minute$ ramp. The wafers stayed at 180℃ for 30 minutes then were heated and held at 250℃ for 30 minutes. The wafers were allowed to gradually cool to room temperature after which they were removed and inspected. The thermal curing process drives out the remaining solvent in the polyimide and allowed the vibrating platform to achieve its electrical and mechanical properties. It decomposes the sacrificial polymer material and released the suspended micromachined RIE resonant sensor (Figure 6.8). The complete RIE sensor fabrication process is illustrated in Figure 6.9.

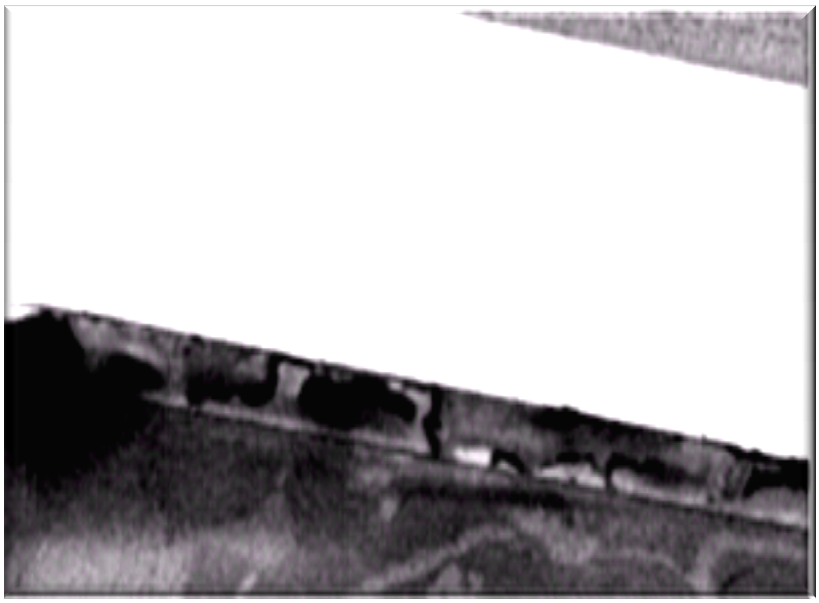

(a)

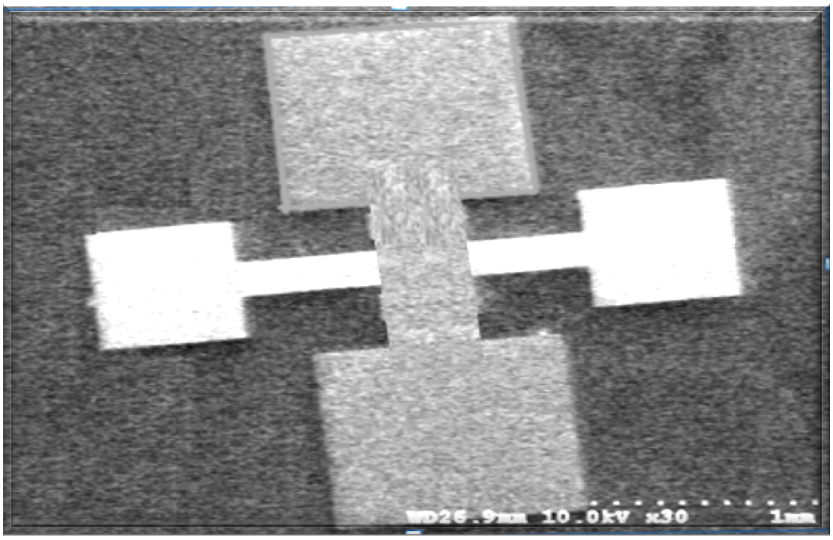

(b)

Figure 6.8: SEM images of micromachined RIE sensor: (a) Platform after thermal cure and decomposition, (b) Suspended RIE sensor.

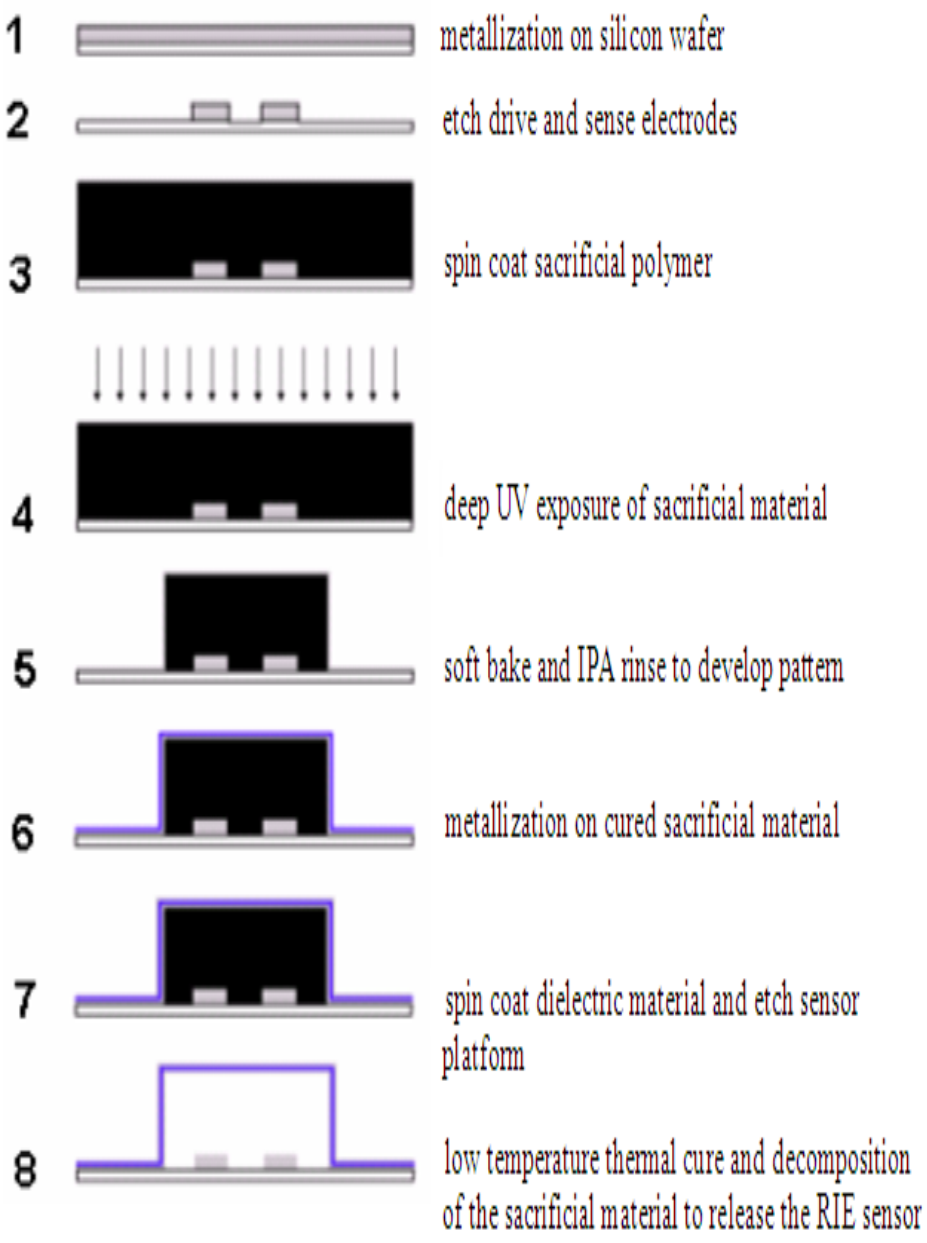

Figure 6.9: Complete RIE sensor fabrication process

6.5 SUMMARY

This chapter focused on the fabrication process of the RIE sensor which is a structured sequence of thin film deposition, photolithography, and selectively etching using surface machined techniques. Four masks were required and utilized to develop the RIE sensor's three major parts: the drive electrode, the sense electrode, and the platform itself. The isolation barrier and resulting air gap is created by utilizing a sacrificial layer material and process to develop and subsequently release the free standing sensor structure.

In view of the importance of the sacrificial layer process, we demonstrated a sacrificial layer technique that possess the following attributes: (1) the process is simple and reproducible; (2) the coating process is compatible with dry or aqueous etching processes; and (3) the release-stiction problem is alleviated by thermal cure and decomposition of the sacrificial material. In chapter 7, the application of the sensor will be demonstrated including electrical testing and integration with the capacitive charge amplifier interface circuit.

CHAPTER 7

7.1 RIE SENSOR MEASUREMENT

Chapter 6 described the fabrication process and function of the RIE sensor. In this chapter, the performance analysis and electrical measurement of the sensor will be presented. As discussed in Chapter 4, there are a number of methods for detecting the motion of the RIE sensor. This work focuses on the capacitive detection of the RIE sensor movement, as this is the most amenable to integration with the charge amplifier capacitive sensing interface circuit. The DC voltage applied between the platform and electrode combined, with a time varying capacitance leads, to a current.

The magnitude of this current will depend on the amplitude of oscillation of the platform. The greater the amplitude of oscillation is, the greater the change in capacitance ($\partial C/\partial x$), and therefore, the greater the change in output current. Based on the dimensions of the vibrating platform, the calculated output current for the RIE sensor is on the order of tens of nanoamps, assuming the mechanical Q of the platform is 1000. It should be noted that a lower Q would lead to lower oscillation amplitude and less output current. Even though the frequency-shifted RIE sensor output is advantageous for noise immunity in signal transmission, such small levels of output current still require a very sensitive test setup.

There are two input methods to drive RIE resonant sensor. One is to place the RIE sensor in the chamber and etch the device, which applies a physical stimulus to the free-standing structure. The other is to apply an electrical signal and applied bias voltage to the platform. There are also two different methods to measure the output of RIE sensor. One is a direct

displacement measurement with a laser interferometer, and the other is electrical measurement using test signals. For direct displacement measurements, an interferometer would have to be constructed using a laser, beam-splitter, lens, mirror, and function generator to verify the movement of the sensor as it is electrostatically excited. A diagram of this optical testing setup is shown in Figure 7.1.

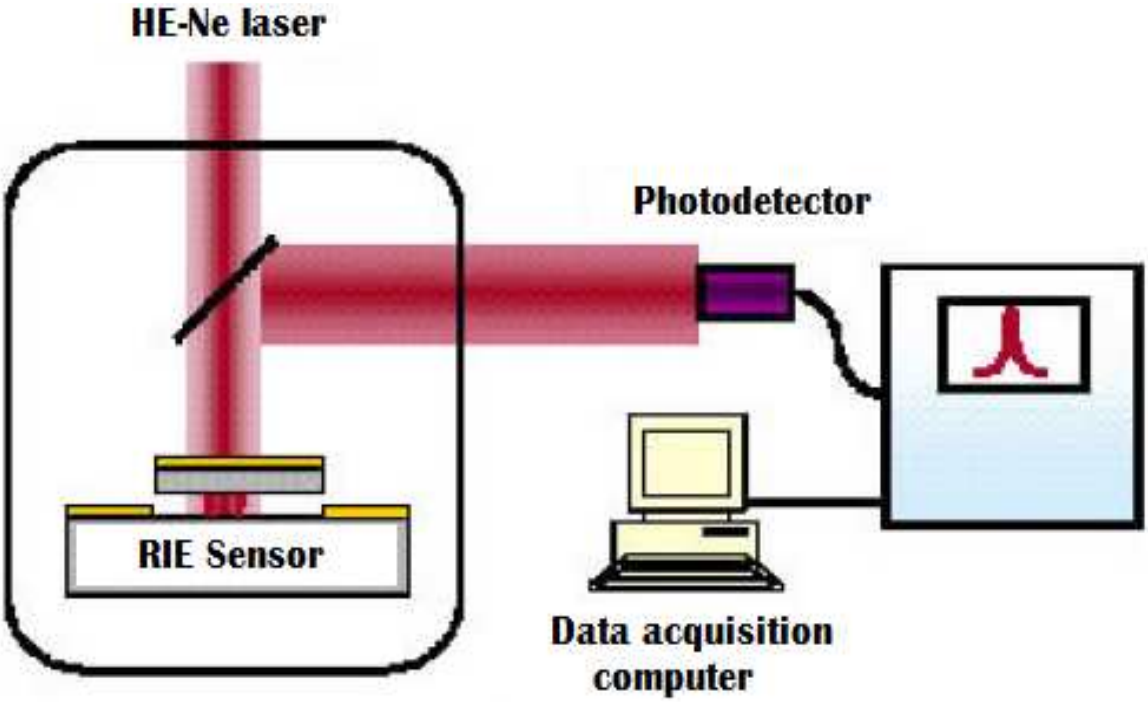

Figure 7.1: An interferometric test setup for measuring the resonant frequency

The RIE sensor resonating platform is illuminated from above by a laser, and reflected light from the both the top surface of the platform and the substrate are photodetected. Interferometric techniques are then used to measure the resonant frequency. Though the direct

measurement with a laser interferometer is straight forward and accurate, aligning it can be a tedious process taking several hours. Additionally, this technique would not be easily integrated into a real time monitoring and control scheme.

Applying a physical stimulus to the RIE sensor, such as mass loading of the platform, is better when duplicating the operating behavior. However, an electrical signal as the input stimulus and electrical output measurement are applicable for electrostatic capacitance measurement testing when cost and speed is a factor. Electrical measurement is also superior in terms of the repeatability, accuracy and usability. The electrical measurement tests that were performed helped to further characterize the RIE sensor behavior. The electrical measurements were later confirmed using capacitive detection as the sensor was brought "on-line" and placed inside the RIE chamber, where the sensor was etched and the resonance frequency was monitored.

7.2 ELECTRICAL TESTING

Before placing the sensor in the chamber, a continuity test was used to verify that the structure was released correctly and that the platform was conductive across its surface. Figure 7.2 illustrates the measurement setup for the continuity test experiment, which consists of the RIE sensor and an Agilent 34401A Digital Multimeter. Figure 7.2(a) illustrates the continuity test that was used for the platform. If the platform was broken at its support, the current (I) would not flow between the anchors. Figure 7.2(b) describes the second experiment. Here, if the platform was shorted as a result of residual sacrificial material remaining between the platform and the drive electrode, current would flow from the drive electrode to the platform. The third

test performed verified that the drive and sense electrodes were isolated (Figure 7.2(c)). Occasionally, the first two tests will be affirmative, but the two electrodes will be shorted. The RIE sensor passed all three continuity tests.

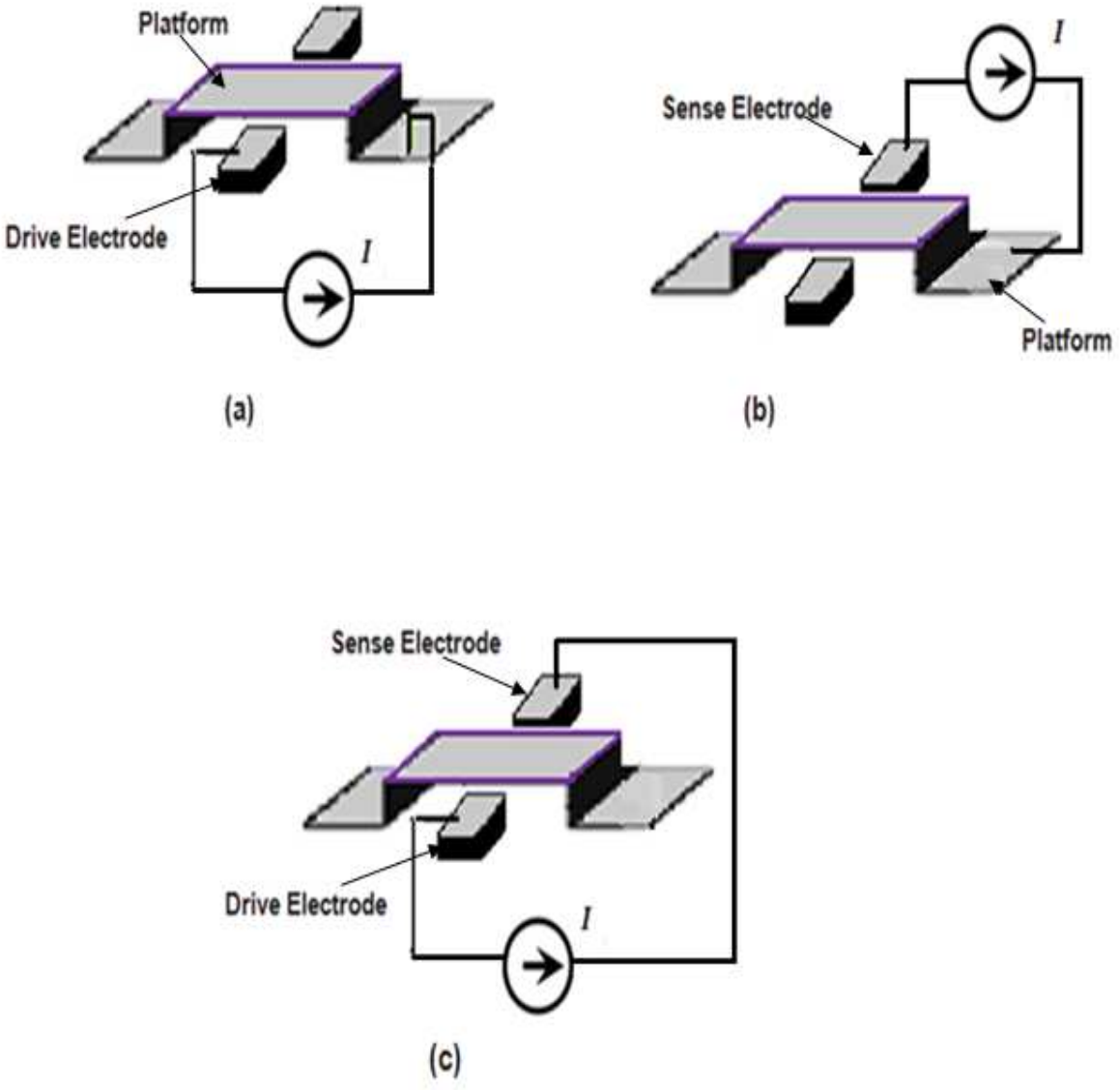

Figure 7.2: Measurement setup for RIE sensor continuity test: (a) platform and drive electrode test, (b) platform and sense electrode test and (c) drive and sense electrode test.

7.3 STATIC AND DYNAMIC SENSOR PARAMETERS

The static response and the dynamic response performance are two mechanical characteristic of the RIE sensor. The properties that are measured in a static analysis are the pull-in displacement and pull-in voltages. Applying a DC voltage to the RIE sensor generates an electrostatic force between the platform and electrodes, which changes the air gap capacitance distance between the electrodes.

The static pull-in test measurement was done with an impedance meter, and as expected, the capacitance varies nonlinearly with the applied voltage (Figure 7.3). There are two reasons for this nonlinearity: the first is the quadratic relationship between electrostatic force and voltage, and the second reason is that the electrostatic force depends on the capacitor gap, which decreases if a voltage is applied. Because of this, the force increases, causing the gap to again decrease.

The RIE sensor has a measured length of 702µm, width of 144µm, thickness of 7.13µm and an air gap measuring 4.05 µm. The base capacitance value of the RIE sensor measured 0.203 pF which is slightly different than the calculated value (approximately 0.22 pF). This could be caused by fabrication process nonuniformity, which causes air-gap variation and compressive stresses in the RIE sensor structure. However, as expected, the capacitance values decrease rapidly if the pull-in voltage increases because the sensor starts to deflect.

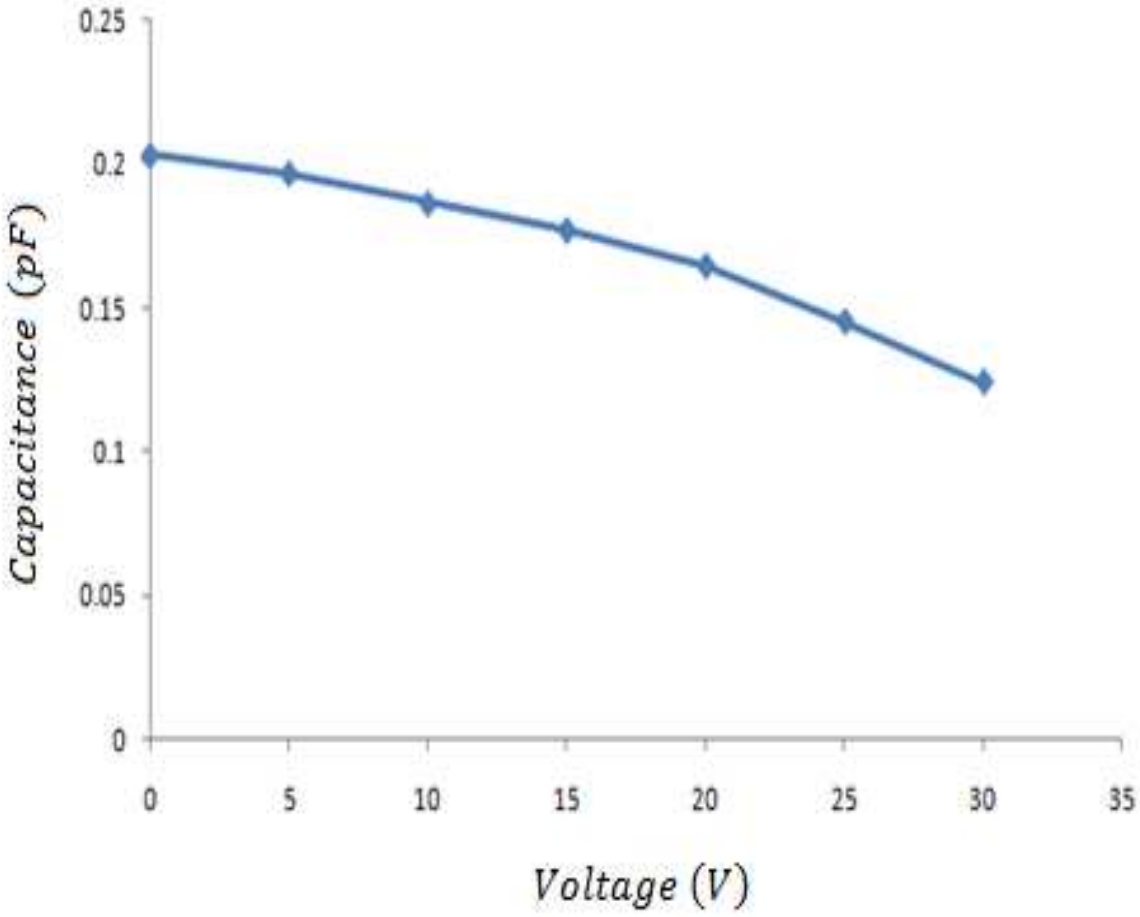

Figure 7.3: Electrostatic capacitance of the RIE sensor as a function of the applied pull-in voltage

The RIE sensor capacitance measured 0.203 pF at its neutral position, and consequently the test setup needed to be capable of measuring electrostatic capacitance accurately in the femto farad range. The most straightforward testing configuration is a two port measurement setup (Figure 7.4). In this configuration, AC voltage was applied at the drive electrode while a DC bias was applied to the sensor platform. At the resonant frequency this AC + DC potential forces

the platform to oscillate. The net DC bias between the electrode and the platform, combined with the induced oscillation, resulted in an output current.

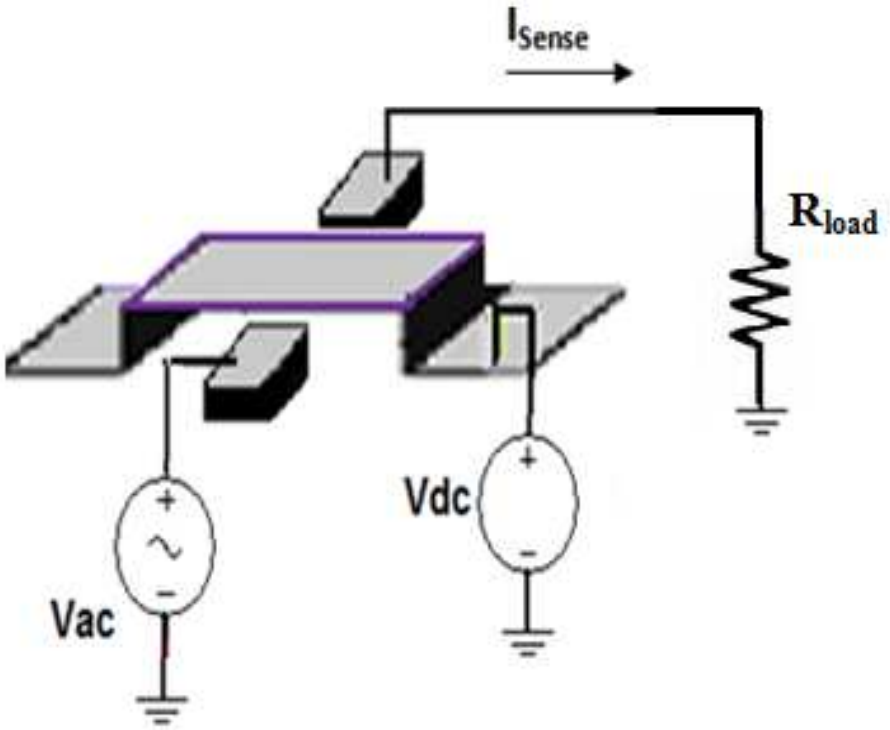

Figure 7.4: Measurement test setup for RIE sensor

When a 1 Vrms voltage step input was applied to the RIE sensor the measured output voltage is 3.8 mVrms (Figure 7.5). The RIE sensor output consists of an exponential decaying impulse due to the parasitic capacitance C_f and an exponentially decaying sinusoidal voltage due to the current. The RIE sensor was designed with a highest Q possible, so that its output will persist much longer than the parasitic capacitance output. The parasitic capacitance however

adds an undesirable current to the RIE sensor total output current, I_{sense}, and its parasitic value at higher operating frequencies will deteriorate the sensor performance over time. It was observed that oscillations are possible but the current across the output impedance is very small (~3.8 nA).

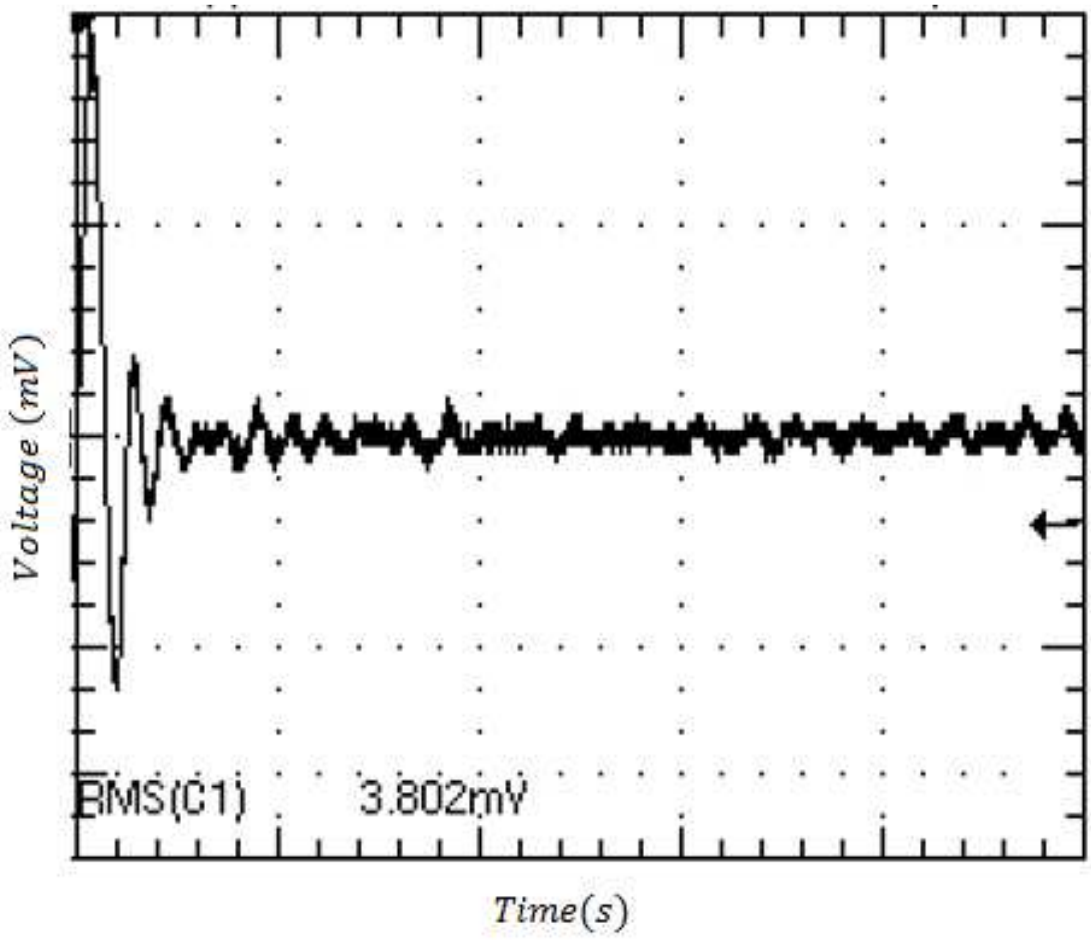

Figure 7.5: Response of RIE sensor to a 1Vrms step input the measured output voltage is 3.802 mVrms.

Increasing the amplitude of the AC input signal has relatively little effect on the output voltage and resulting output current. The RIE sensor response to a 10 Vrms 1kHz AC square wave is shown in Figure 7.6. The output voltage measured 27.1 mVrms and the resulting sensor current is approximately 27.1 nA rms.

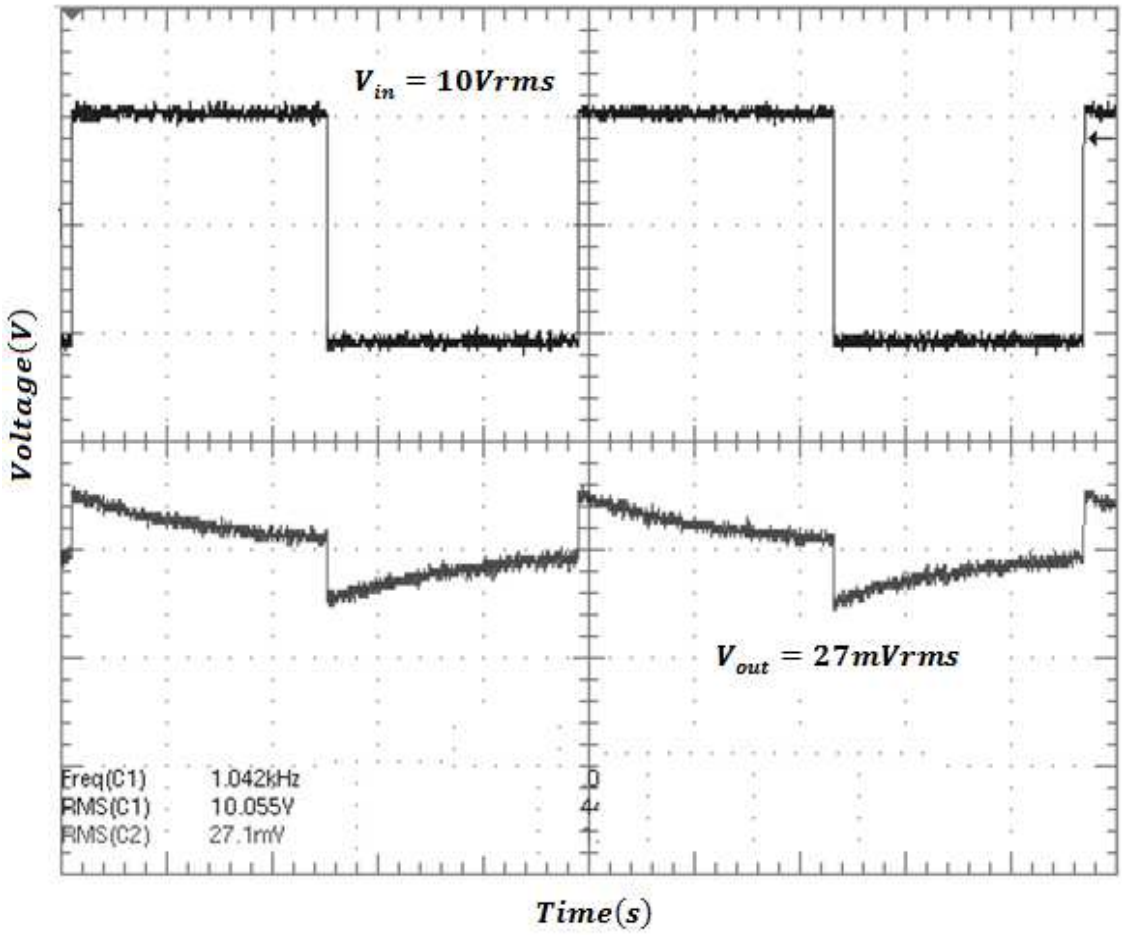

Figure 7.6: The voltage output to a 10Vrms 1 kHz input measured 27.1 mVrms.

As discussed earlier, the platform has large motional resistance, which results in a mismatch between the source or load impedance and the RIE sensor equivalent circuit. Relying on such small sensor current to determine the resonance condition for etch rate monitoring is not effective without amplification of the output signal and the addition of a circuit to compensate for the impedance mismatch. This impedance mismatch leads to input power being reflected. The voltage reflection coefficient is given by [101]:

$$\Gamma = \frac{Z_{sensor} - Z_{input}}{Z_{sensor} + Z_{input}} \tag{7.1}$$

where Z_{sensor} represents the impedance of the platform, and Z_{input} the impedance of the input source. The motional impedance of the RIE sensor is approximately 970MΩ, and for a 1kHz AC input signal the reflection coefficient is ($\Gamma \cong 1$).

With large impedance mismatch, most of the power that is applied at the drive electrodes never reaches the platform, which results in less electrostatic force on the platform, minimal change in air gap capacitance, and lower amplitude of vibration. Increasing the power at the drive electrodes compensates for this problem and improves the RIE sensor sensitivity, but this also increases the possibility of damage to the signal source and deterioration in the sensor performance.

Initially, no output transimpedance amplifier was employed at the sensor output node. So in order to match the motional resistance of the platform to the resistance of the load with sufficient bandwidth, a series of LC matching networks was needed. The downside was that as

more components are added to the output signal path, the signal loss became greater. In addition the useful bandwidth of the LC matching network limited the detectable frequency range of a signal. For this work, monitoring the fundamental mode which occurs at approximately 40 kHz is of greatest interest. In this regard, the modeling and simulations previously conducted proved to be useful for approximating the RIE sensor resonant frequency and in designing the LC matching network (Figure 7.7).

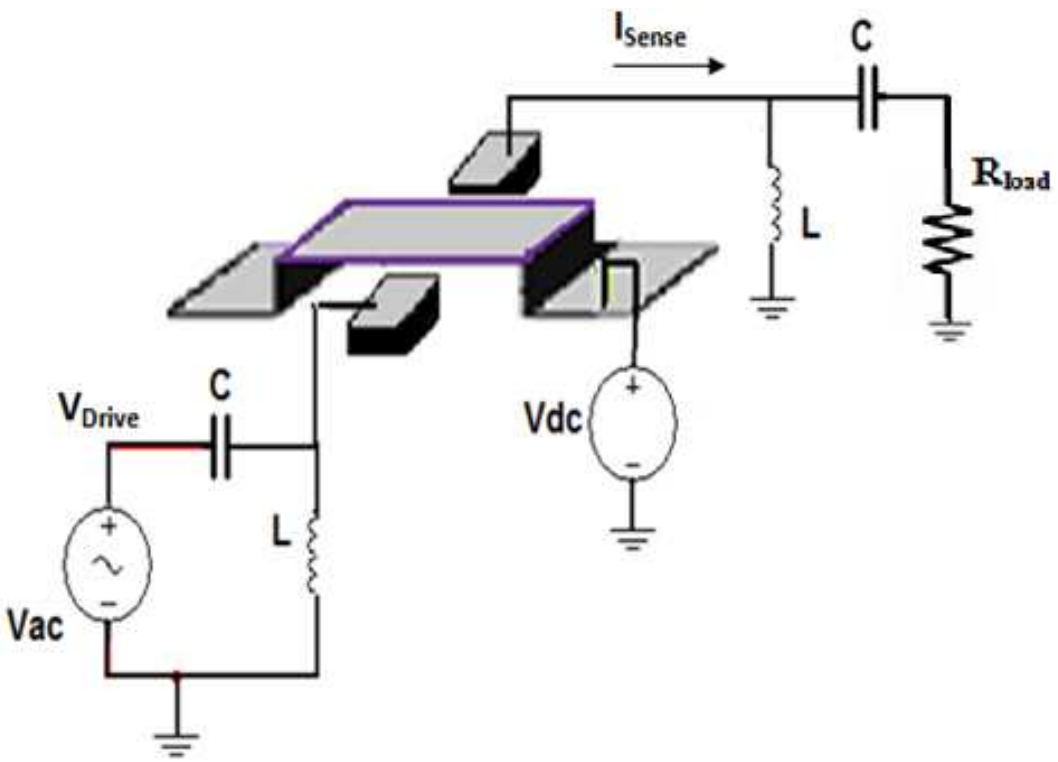

Figure 7.7: RIE sensor and matching LC network configuration

When the RIE sensor is subject to a physical stimulus, its response is often represented by parameters such as resonance frequency, Q-factor, and 3dB bandwidth. To obtain time plots of the resonance frequency, the output of the sensor was connected directly across the sense electrode. The signal at the drive electrode was offset by DC bias voltage and the oscillation frequency was then measured. We are primarily interested in monitoring the fundamental mode and the plot of the normalized frequency response curve shows that this occurs at 43.2 kHz (Figure 7.8).

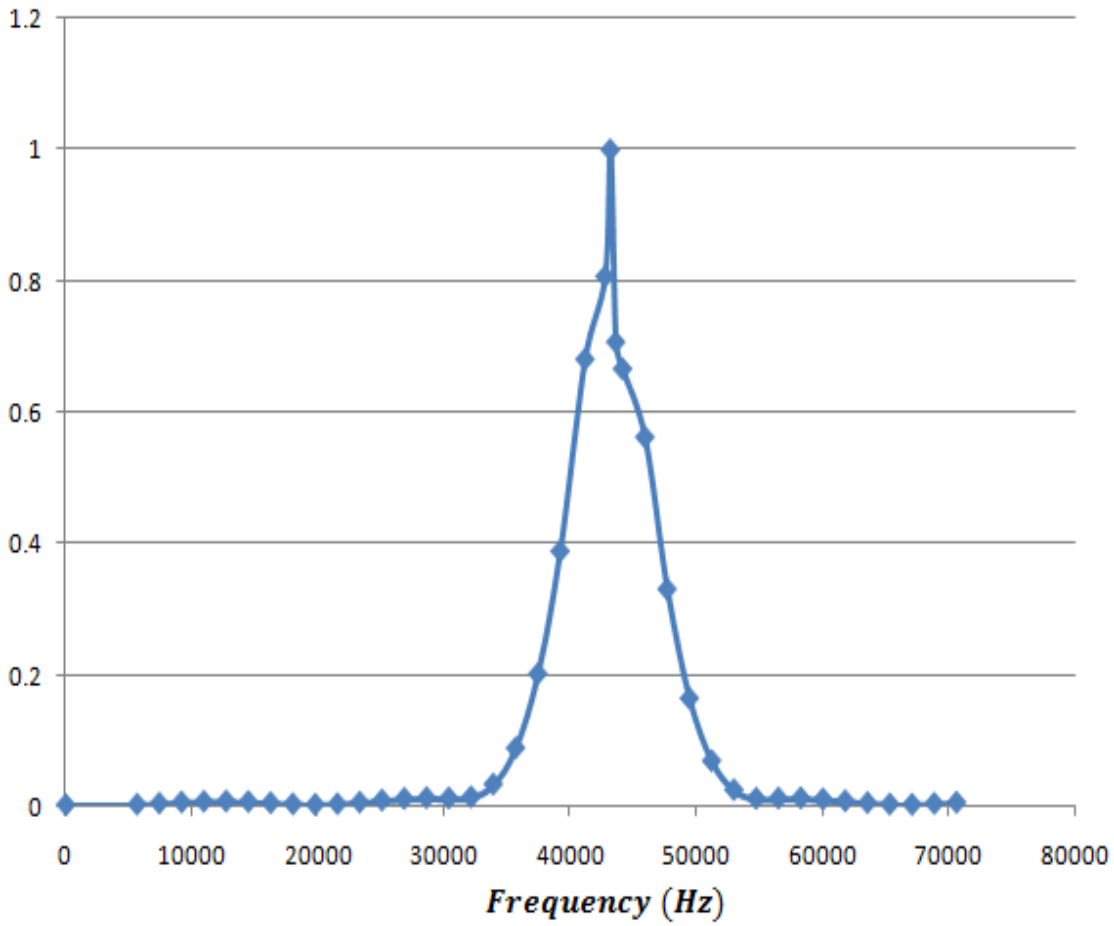

Figure 7.8: The normalized frequency response curves of the RIE sensor with DC bias voltage showing a fundamental f_1 = 43.2 kHz.

This frequency compares well with the calculated and simulated frequencies of 37.7kHz and 41kHz respectively. The discrepancy in the values may be attributed to the stress in the platform as a result of the air damping as this measurement was made in air at atmospheric pressure. The value is expected to be within this range when the RIE sensor is brought on-line and operated in the RIE chamber.

The bandwidth BW was determined (850Hz) from the frequency response plot and with respect to the mechanical Q-factor in air, it was calculated using the relation ($Q= f_1/BW$). The mechanical quality factor in air is 51. The results are summarized in Table 7.1.

Table 7.1: Sensor parameters and resonant frequency and Q

length	*width*	*height*	*air gap*	f_1 *Calculated*	f_1 *Simulated*	f_1 *Measured*	*BW*	*Qfactor*
705 *μm*	144 *μm*	7.13 *μm*	4.1 *μm*	37.7 *kHz*	40.7 *kHz*	43.2 *kHz*	0.85 *kHz*	51

The RIE sensor has nominal capacitance of 0.20 – 0.22pF. Due to the bending deformation of the platform in the μm range (and thus small surface strains), the capacitance changes are in the fF range. The RIE sensor relies on capacitive transduction to detect small capacitance changes and the resulting change in resonant frequency during the RIE process. The RIE sensor's overall performance is limited by the interface circuit, and integration with the

proper circuit allows the RIE sensor to function as a highly sensitive measure of etch rate during the RIE process.

In order to measure these small capacitance changes, it was necessary to focus on the parasitic capacitances that are somewhere in the same order as the capacitance changes to be measured and thus affects the in situ etch rate measurement significantly. To provide the necessary output resolution and suppress the parasitic capacitances effectively, the RIE sensor was configured with a capacitive feedback charge amplifier circuit.

7.4 RIE SENSOR AND CHARGE AMPLIFIER CIRCUIT

The RIE sensor is integrated with electronics developed with respect to the capacitance change, ΔC of the RIE sensor. As mentioned earlier, based on application complexity and accuracy of measurement, the capacitive charge amplifier interface circuit was used. The preliminary analysis of the electronic amplifier circuit was presented in Chapter 4, and it was shown that the charge amplifier circuit is suitable for suppressing parasitic capacitances effectively. The capacitance change is measured in combination with the reference capacitance, C_f, which is in the neighborhood of the RIE sensor capacitance.

The charge amplifier interface circuit was fabricated in a 0.5 µm two-metal two-poly CMOS process, which is fully compatible with the RIE sensor technology. This is why it is possible to design, realize and test the building blocks of the sensor separately, before it is integrated with the charge amplifier chip. The topology of the T5CXAV CMOS charge amplifier chip is a cascade operational transconductance amplifier (OTA) operating in the deep subthreshold region (Figure 7.9). A tunneling junction and an indirect injection transistor are

integrated on chip as floating-node charge adaptation circuitry to avoid large leakage currents. The circuit parameters are listed in Table 7.2.

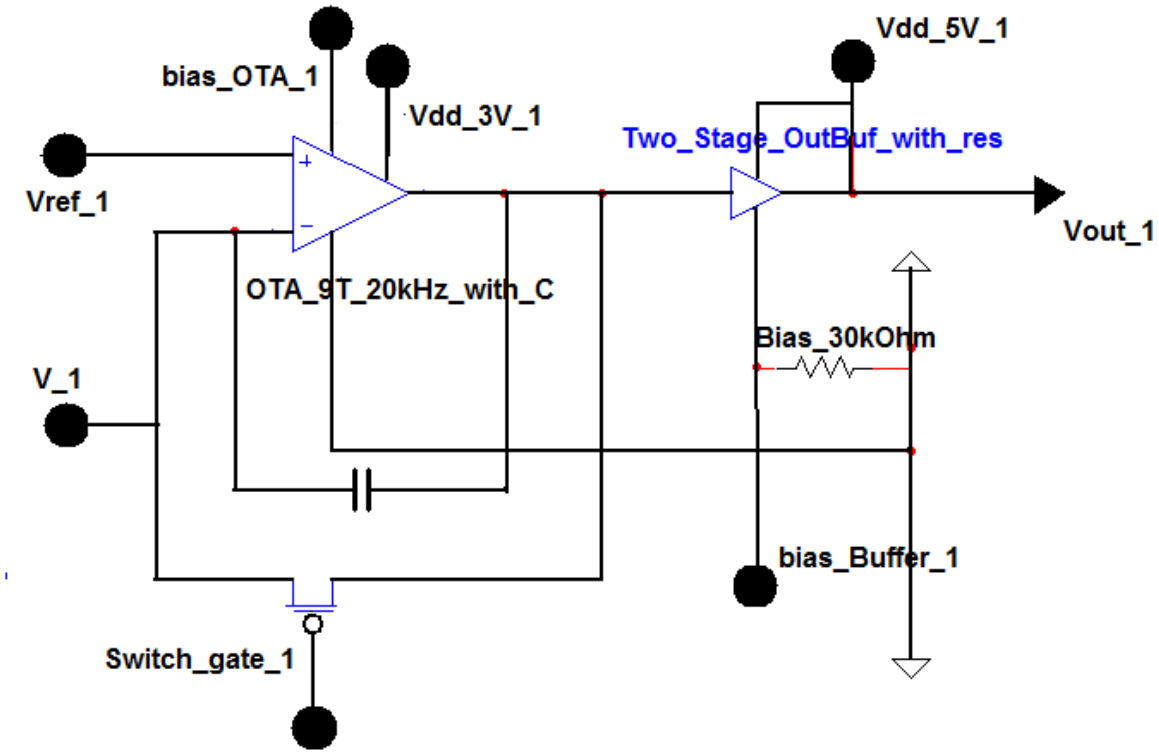

Figure 7.9: T5CXAV CMOS chip charge amplifier sub-circuit

Table 7.2: Charge Amplifier Interface Circuit Parameters

CIRCUIT PARAMETERS	
Area	$390 \times 200\ \mu m^2$
Power Supply	$3.3V$
Amplifier Power Consumption	$0.5\mu W$
Open-Loop Gain	$80dB$
Bandwidth f_{BW} $(C_L = 0.4\,pF)$	$25kHz$
Feedback Capacitance C_f	$20fF$

The RIE sensor was connected to the sensing amplifier interface circuit by soldering wires from the sense electrodes directly to the pad connecting to the capacitive feedback amplifier. The interface circuit used the auto-zeroing mechanism to stabilize the leaky floating node voltage and integrated the input charge over time. The charge amplifier circuit is very sensitive to the RIE sensor leakage current and the voltage output was measured directly from Vout_1 output pin.

An AC input voltage biased with 10V DC was applied to the drive electrodes of the RIE sensor as shown in shown in Figure 7.10. The output of the RIE sensor is connected to the charge amplifier circuit, which applies a voltage step every half period after a rising or falling edge of V_{drive}, and the component due to the parasitic capacitance C_f reduces to nearly zero. After the amplifier stage, the difference signal passes through a comparator in order to determine the voltage and current DC offsets of the operational amplifier. The comparator determines when the zero crossing occurs and applies a new voltage step to the RIE sensor. The DC offset of the

processed signal is fed back to the instrumentation amplifier as zero point reference. Thus an automatic DC offset compensation is realized.

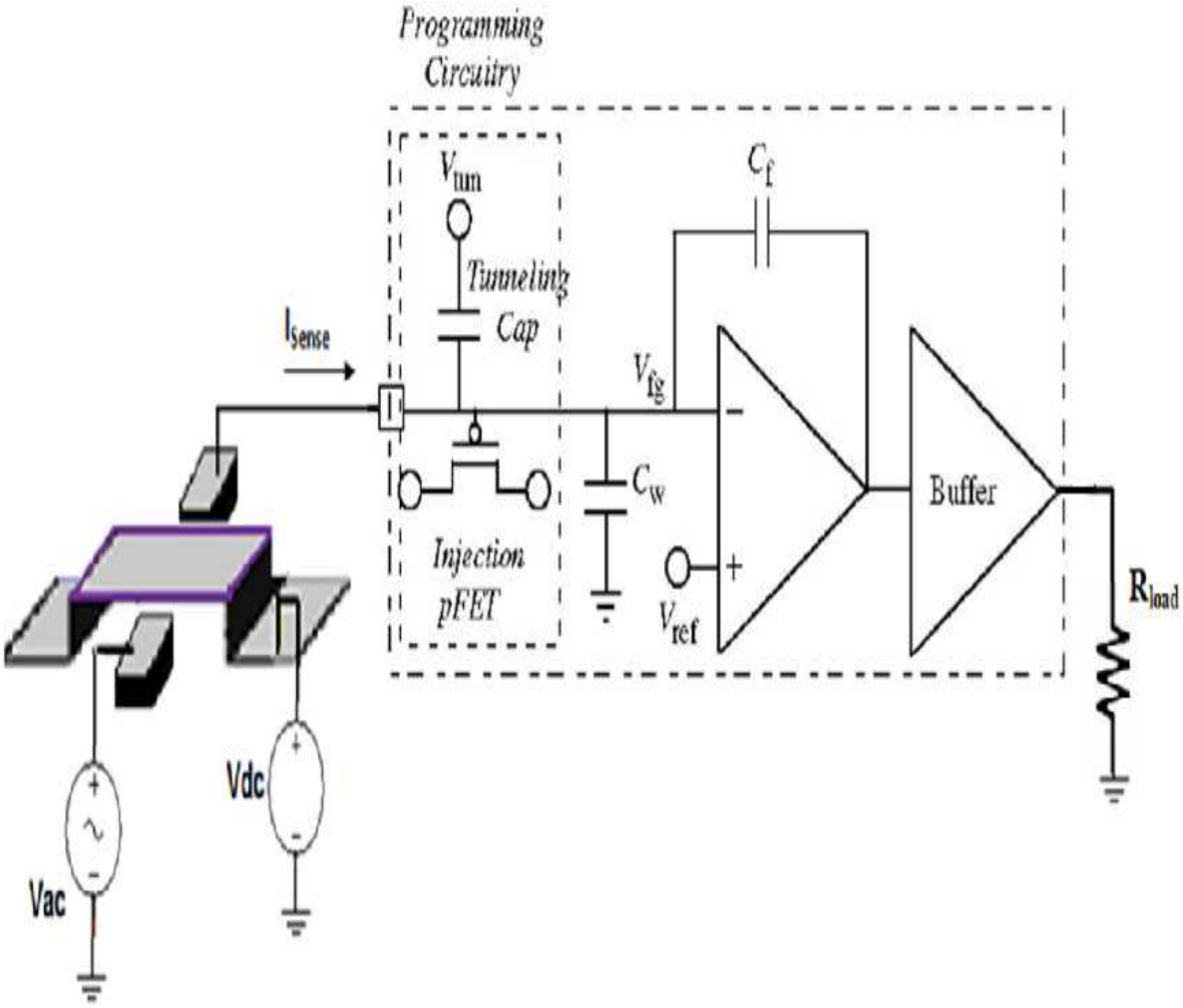

Figure 7.10: The test setup of the RIE sensor and capacitive sensing circuit

The output voltage waveform of the integrated RIE sensor and charge amplifier circuit response to a 5 Vrms 1kHz AC square wave is shown in Figure 7.11. The RIE sensor voltage and current was measured at the input of the amplifier stage. The voltage measured 8.7 V, which results in a sensor current of 180 pArms. The output voltage when measured across the 50Ω output impedance measures 1.36 Vrms. The resulting integrated sensor current is approximately 27.2 mArms.

Based on these measurements, the output of the charge amplifier stage, which is controlled by feedback, largely determines the magnitude of its output voltage gain and facilitates regenerative gain and oscillation. The high input impedance from the RIE sensor still results in a measurable output current with a 5 Vrms input voltage, which is significantly higher that previous circuit topology because of the DC offset compensation.

The RIE sensor and charge amplifier subcircuit yields a gain factor A = $20 \times log_{10} (\frac{V_{out}}{V_{in}})$ of 11.4 dB. The RIE sensor can be realized with higher gain when operated inside the RIE chamber, where the pressure is less than atmospheric pressure. In addition to operating with higher Q-factors, the charge amplifier stage circuit will be realized with a higher gain factor and provide very high sensitivity for capacitive sensing. This fact accompanies a higher sensitivity simultaneously.

The response of the amplifier is flat to about 100 kHz, which is much larger than the carrier frequency (Figure 7.12). This is more than adequate, since the carrier frequency should not have a higher frequency than 100 kHz due to the relatively low modulating (resonance) frequency of the RIE sensor.

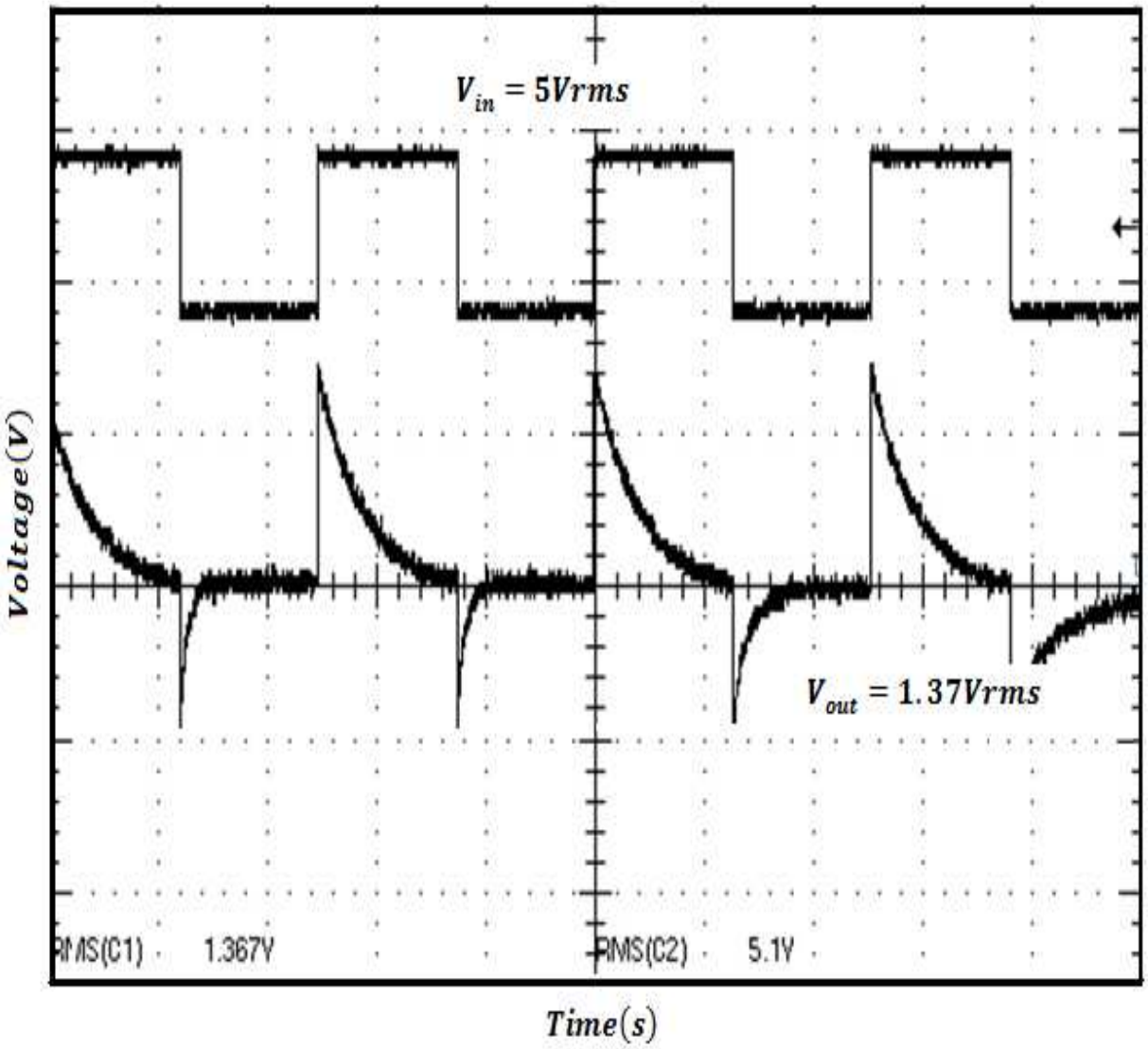

Figure 7.11: The output to a 5.1Vrms square wave input voltage measured 1.367Vrms

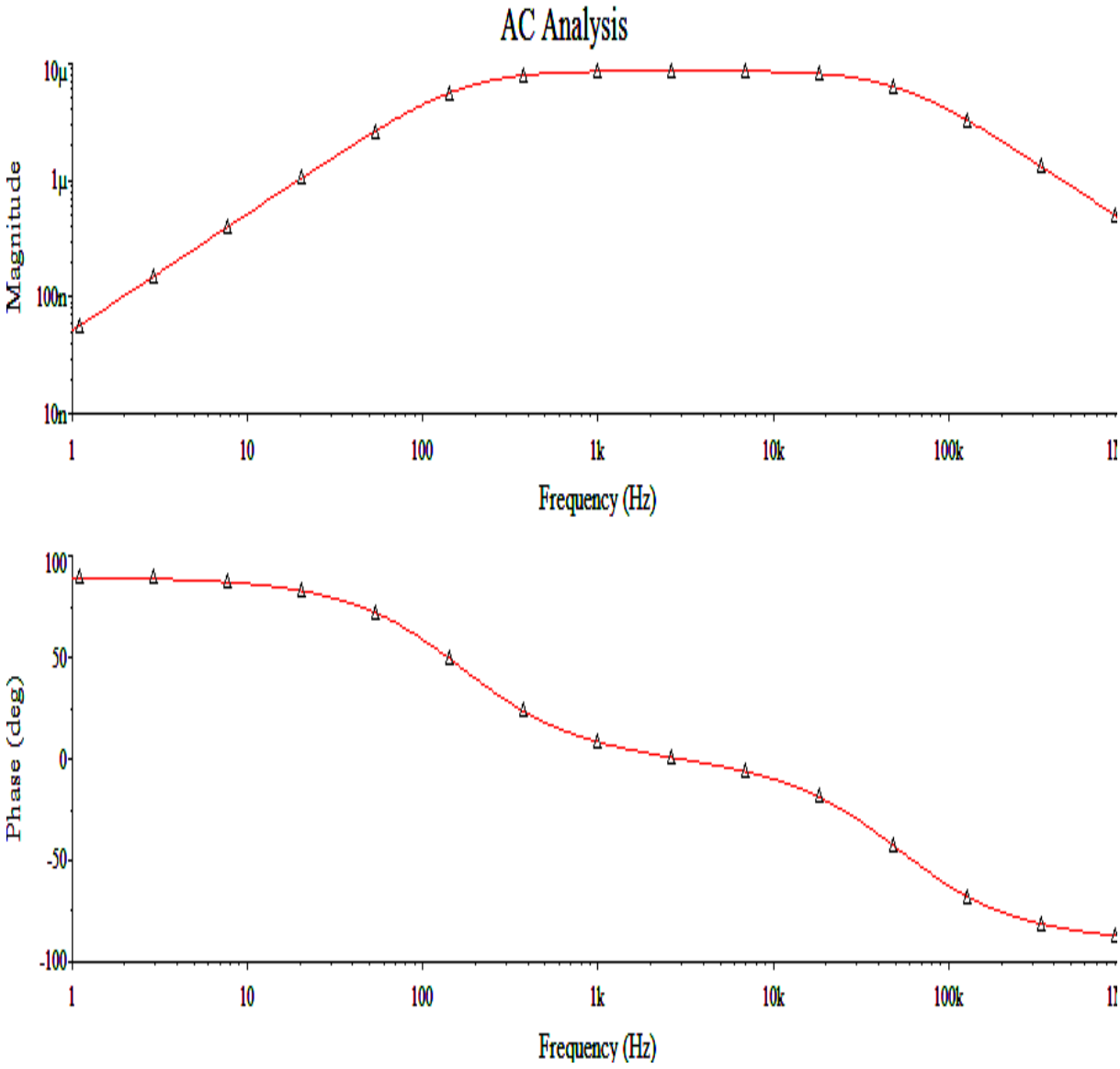

Figure 7.12: Amplitude and phase response of the charge amplifier circuit

7.5 SUMMARY

The performance analysis and electrical measurement of the RIE sensor was presented. This work focuses on electrostatic excitation and capacitive detection of the RIE sensor. Before placing the sensor in the chamber, a continuity test was used to verify that the structure was released correctly. The static response measurement results confirmed that the capacitance varies nonlinearly with the electrostatic force generated by a bias voltage. The electrostatic force was used to adjust the resonant frequency electrically in order to match the driving and detecting resonant frequency for high sensitivity.

The RIE sensor has large motional resistances and the small output current cannot be effectively used for in situ etch rate monitoring without amplification of the output signal and the addition of a circuit to compensate for the impedance mismatch. The RIE sensor's overall performance is limited by the interface circuit and integration with the capacitive charge amplifier allows the RIE sensor to function as a highly sensitive measure of etch rate during the RIE process by suppress the parasitic capacitances effectively. The integrated RIE sensor and charge amplifier interface circuit will be operated in the PlasmaTherm SLR RIE system and is expected to facilitate closed-loop feedback control of the RIE process.

CHAPTER 8

8.1 RIE SENSOR FEEDTHROUGH PROBE

The RIE sensor was operated in the PlasmaTherm SLR RIE chamber, where closed-loop feedback control of the process was demonstrated. The PlasmaTherm equipment is a single-chamber system with a load lock. It is designated for etching substrates using the following gases: Cl_2, BCl_3, CCl_2F_2, H_2, Ar, CF_4, and O_2. The flow rate for each gas is set by a mass-flow controller, and the pressure is controlled separately by a valve between the chamber and the pump.

There are four vacuum inlets on the RIE chamber, one of which will provide access to the drive and sense electrodes inside the chamber. The vacuum channel is terminated by a simple high-vacuum seal that can be easily removed. These inlets are shielded from the plasma glow region on the RIE chamber. A feed-through probe was designed to access the RIE sensor, such that the performance of the RIE chamber would not be compromised. In this regard, the inlet valve which currently terminates with a vacuum seal was removed and a stainless steel conical reducer was added. Figure 8.1 shows the attachment of the vacuum system to the PlasmaTherm SLR RIE chamber.

The conical reducer was attached to a BNC coax feed-through using stainless steel vacuum seals. Copper wires covered in ceramic beads were connected to the probe. The ceramic beads were used to insure that air pockets, which may result from using coated wires, would be eliminated (Figure 8.2). Connectors were then soldered on the ends of the feed-through wires.

(a)

(b)

Figure 8.1: PlasmaTherm SLR RIE chamber sensor feed-through a) stainless steel conical reducer and, b) BNC coax chamber attachment

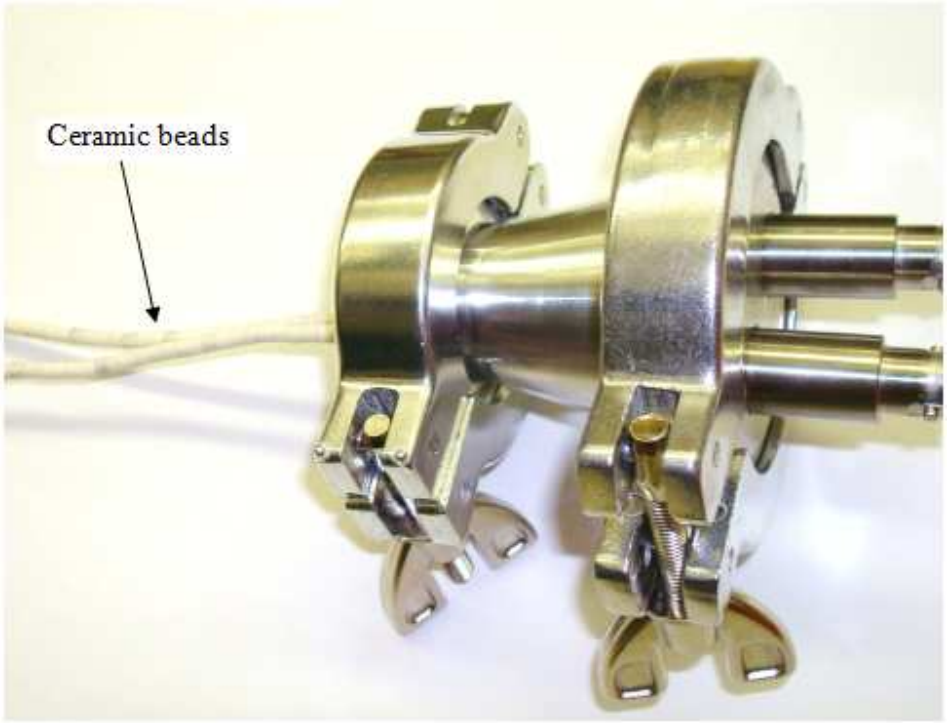

Figure 8.2: Copper wires covered with ceramic beads to RIE sensor drive and sense electrodes

8.2 RIE ETCH RATE MONITORING TEST SETUP

The PlasmaTherm RIE chamber was prepared with a thorough cleaning prior to the RIE sensor etch rate monitoring test. The cleaning step ensured that any residual process gases that remained in the chamber were removed. Etch rate is a function of the process chamber conditions and its history, so the cleaning process significantly reduced the possibility of etchant gas cross-contamination and other factors that would influence the RIE sensor etching process and affect the time and outcome of the etch rate monitoring test. This also produced more reproducible results. The RIE chamber was pumped down, and an oxygen cleaning gas flowed into the chamber at a rate of 30 *sccm* while maintaining a vacuum and RF power. The cleaning process for the PlasmaTherm RIE chamber is summarized in Table 8.1.

Table 8.1: PlasmaTherm RIE chamber preparation process

Pressure (mTorr)	***Time (s)***	***Gas***	***RF Power (W)***
100	3600	O_2 (30 *sccm*)	300

The PlasmaTherm SLR RIE system is equipped with a load-locking chamber, and interlocks for handling the etchant gases (e.g., O_2, *Ar*, Cl_2, BCl_3, $CHCl_3$) and for automatic loading and unloading of samples through the slit-valve. The automatic movement of the chamber loading arm and loadlocks were disabled over the duration of the RIE sensor measurement test. During the RIE etching process, conditions such as, RF power, gas flows, pressure, and bias are constantly monitored. The ion gauge controller, which monitors out-

gassing of the etchant gases, was removed, and its function was disabled. The RIE sensor feed-through probe was then coupled to the inlet valve reserved for the ion-gauge controller. The ceramic coated feed-through wires were carefully fed through the ion-gauge valve and up into the PlasmaTherm RIE process chamber.

After the RIE chamber was properly cleaned, it was vented (which takes 10 to 15 minutes). The RIE sensor was placed on the substrate loading plate, and it was manually moved into the process chamber. The ceramic coated feed-through probe pads were then secured to the drive and sense electrodes electrical contact pads with kapton tape. The heat-resistant tape is an ideal adhesive and insulator that can withstand elevated temperatures and it prevented the feed-through probe copper pads from coming into contact with the plasma. Any exposed copper in the charge plasma causes electrical arcing, triggers the RIE chamber alarms and eventually disables the etching process.

The thin layer of aluminum on top of the RIE sensor platform that was etched during the etch rate monitoring test was measured with an Alpha-Step Profilometer before the sample was loaded into the RIE chamber. The thickness of the aluminum measured at 528Å. The RIE chamber was pumped down to $< 0.3\ Torr$, and the aluminum etch recipe that was developed for the etch rate monitoring test was loaded. The first step of the aluminum etch recipe was the chamber pump-down, which was set to $1 \times 10^{-2} Torr$. The gas stabilization step followed, and the flow rate for the aluminum etchant gases (Cl_2 *and* BCl_3) was set. During the gas stabilization step, the RF power was not applied, so the etchant gases were not charged (no plasma), and no pre-mature etching of the RIE sensor occurred during this step. The third step in the aluminum recipe was the etch process. The RIE chamber pressure was set to $30\ mTorr$, and the RF power was activated for 2 minutes. The etch time was determined based on the most

recent data from the PlasmaTherm RIE log sheets and from test runs with aluminum coated samples with the same thickness. The etchant gases were purged, and the chamber pressure was returned to atmospheric pressure and vented in steps 4 and step 5 of the aluminum etch recipe. The aluminum etch recipe is summarized in Table 8.2.

Table 8.2: RIE sensor aluminum etch recipe

Step	***Pressure (mTorr)***	***Time (s)***	***Gas***	***RF Power (W)***
Pump loadlock	10	30	–	–
Gas Stabilazation	30	30	Cl_2 (10 *sccm*) BCl_3 (40 *sccm*)	–
Etch	30	120	Cl_2 (10 *sccm*) BCl_3 (40 *sccm*)	125
Purge loadlock	10	60	–	–
Vent	10	600	–	–

In the final experiment, the RIE sensor was etched with the aluminum etch recipe. Process control was demonstrated by monitoring the RIE sensor current during the excitation of the plasma and transmitting the resonance information outside of the PlasmaTherm RIE chamber. The plasma environment is typically noisy, and it is difficult to extract the RIE sensor signal. The diagram of the etch rate monitoring measurement test setup is shown in Figure 8.3. The setup consisted of the the micromachined RIE sensor, the charge amplifier capacitive-

sensing T5CXAV chip, the RIE chamber feedthrough probe, analog and digital I/O boards, a GPIB card to interface with the data acquisition computer, power supplies, and miscellaneous lab hardware and supplies.

The feedthrough probe connected the RIE sensor drive and sense electrodes to the T5CXAV charge amplifier circuit and AC voltage source. Two analog and digital I/O boards were used to interface with the integrated RIE sensor and charge amplifier circuit with the data acquisition computer and lab equipment. The PCI-DAS4020/12 board is a high speed 4 channel, 12 bit analog input board with two output channels and 24 digital I/O channels. The PCI-DDA08/16 board provides eight channels of 16-bit analog output and 48-bits of digital I/O. The PCI-488 GPIB board is the interface between the I/O boards and converts the PCI bus into a control and data acquisition system.

The InstaCal calibration and test software was used to configure the three boards which are shown in Figure 8.4. The MATLAB data acquisition toolbox provided the necessary tools for controlling and communicating with the data acquisition hardware and was used to configure the external circuit and hardware devices and read data into MATLAB for further analysis.

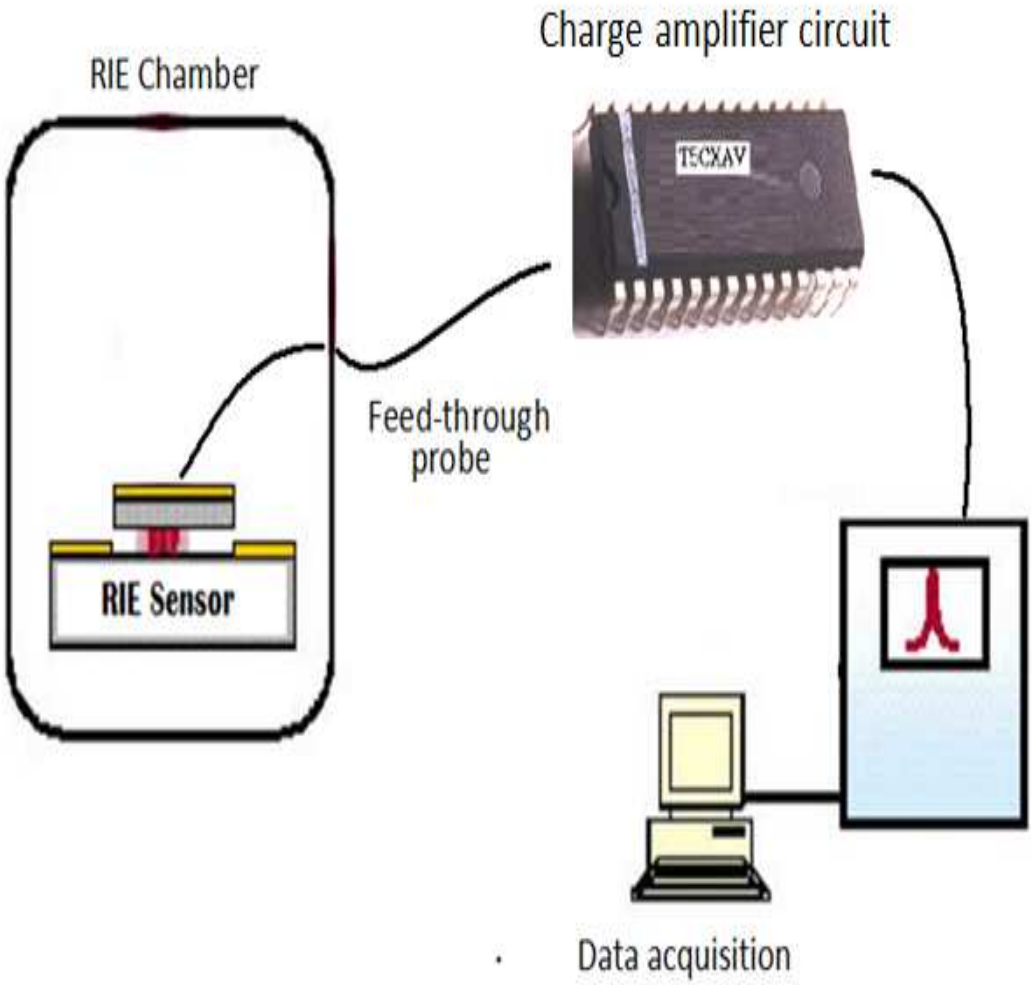

Figure 8.3: RIE chamber etch rate measurement setup

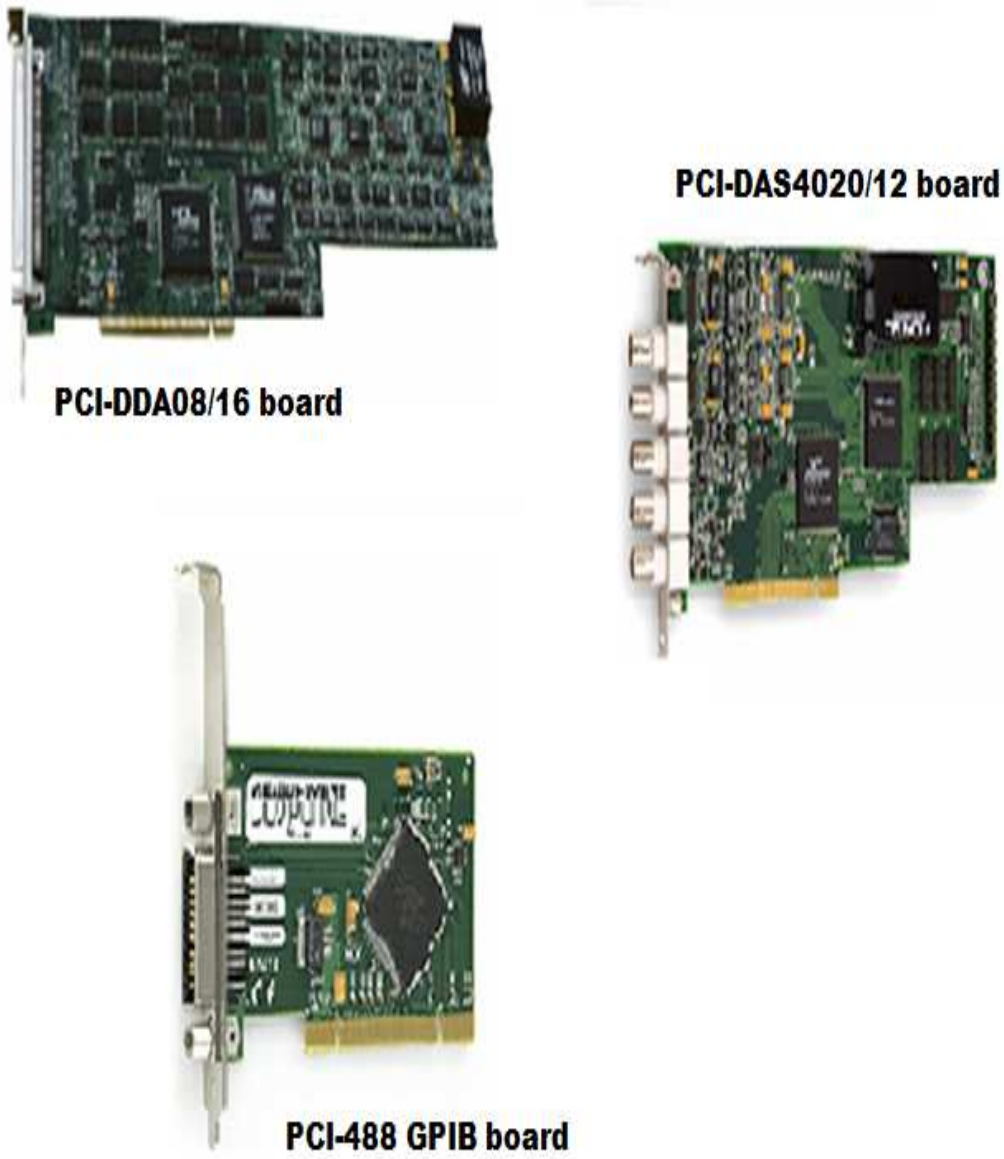

Figure 8.4: Analog and Digital I/O and GPIB boards used to interface the RIE sensor and external circuit and measurement equipment

8.3 INTEGRATED RIE SENSOR MEASUREMENTS

The RIE sensor was driven into resonance and measurements were taken while the PlasmaTherm RIE chamber was pumped down to a pressure of $10\,mTorr$ and prior to excitation of the plasma. The voltages were measured at the RIE sensor output and at the output pin of the charge amplifier interface circuit as described in Chapter 7.4. The voltage at the RIE sensor electrode measured 4.423mVrms and 975mVrms when measured at the output of the charge amplifier circuit. The RIE sensor resonant frequency measured 58.5 kHz. The resulting output voltage waveform and frequency spectrum are shown in Figure 8.5.

During the gas stabilization stage, the pressure in the chamber was at 30 mTorr and the etchant gases flowed into the chamber. It was observed that the gas flow affected the RIE sensor output even though no RF power was applied. The measured voltages at both the RIE sensor sense electrode and at the output of the charge amplifier circuit decreased during the gas flow. A voltage change of $50.2\mu V$ at the sensor output resulted in a $11.1mV$ change at the output of the charge amplifier interface circuit. The results are consistent with the non-linearity of the charge amplifier circuit, when the input voltage is small and results from the voltage-controlled current source of the transconductance amplifier. The measured waveform along with the spectrum is shown in Figure 8.6.

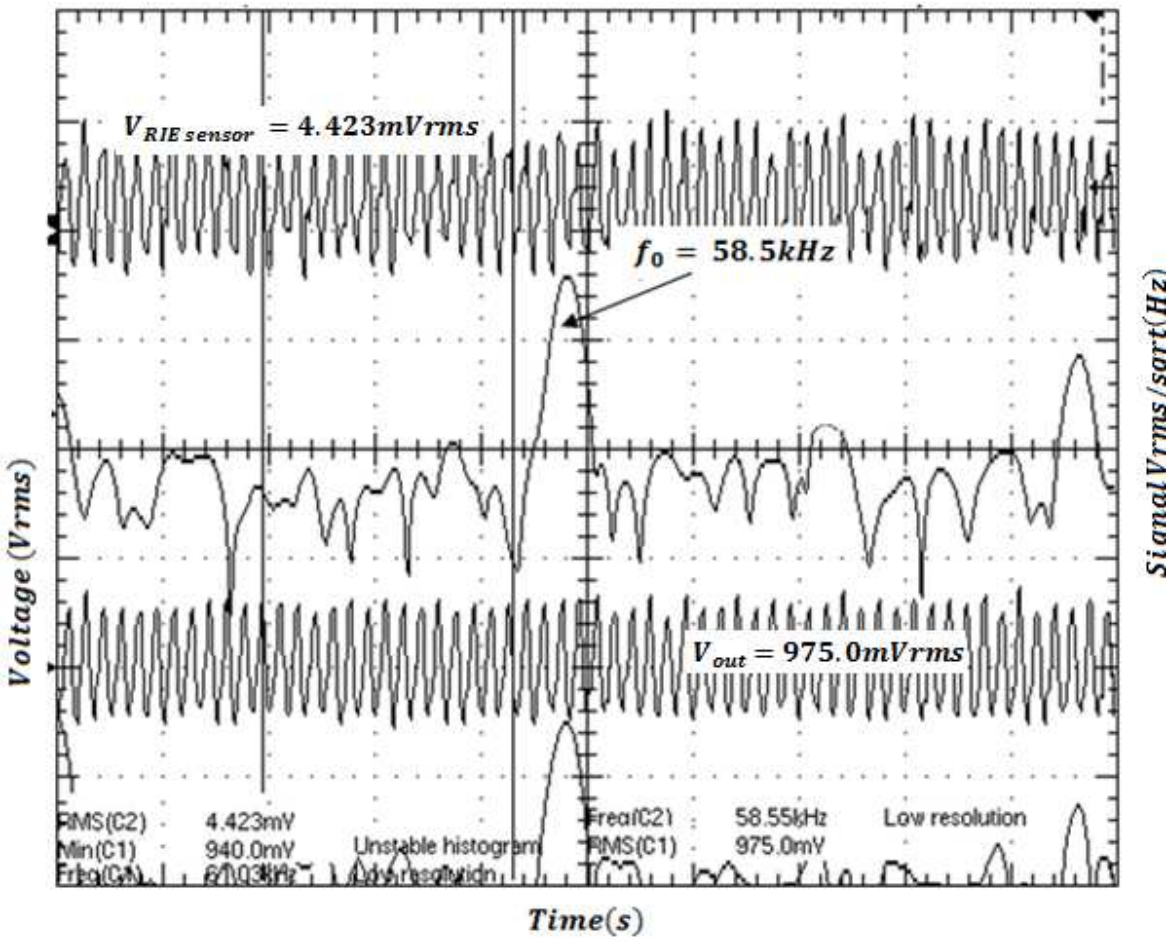

Figure 8.5: Measured waveform taken at $10mTorr$ prior to gas flow and excitation of the plasma. The RIE sensor resonant frequency measured 58.5 kHz. The voltage at the RIE sensor output measured 4.423mVrms and 975mVrms at the output of the charge amplifier circuit

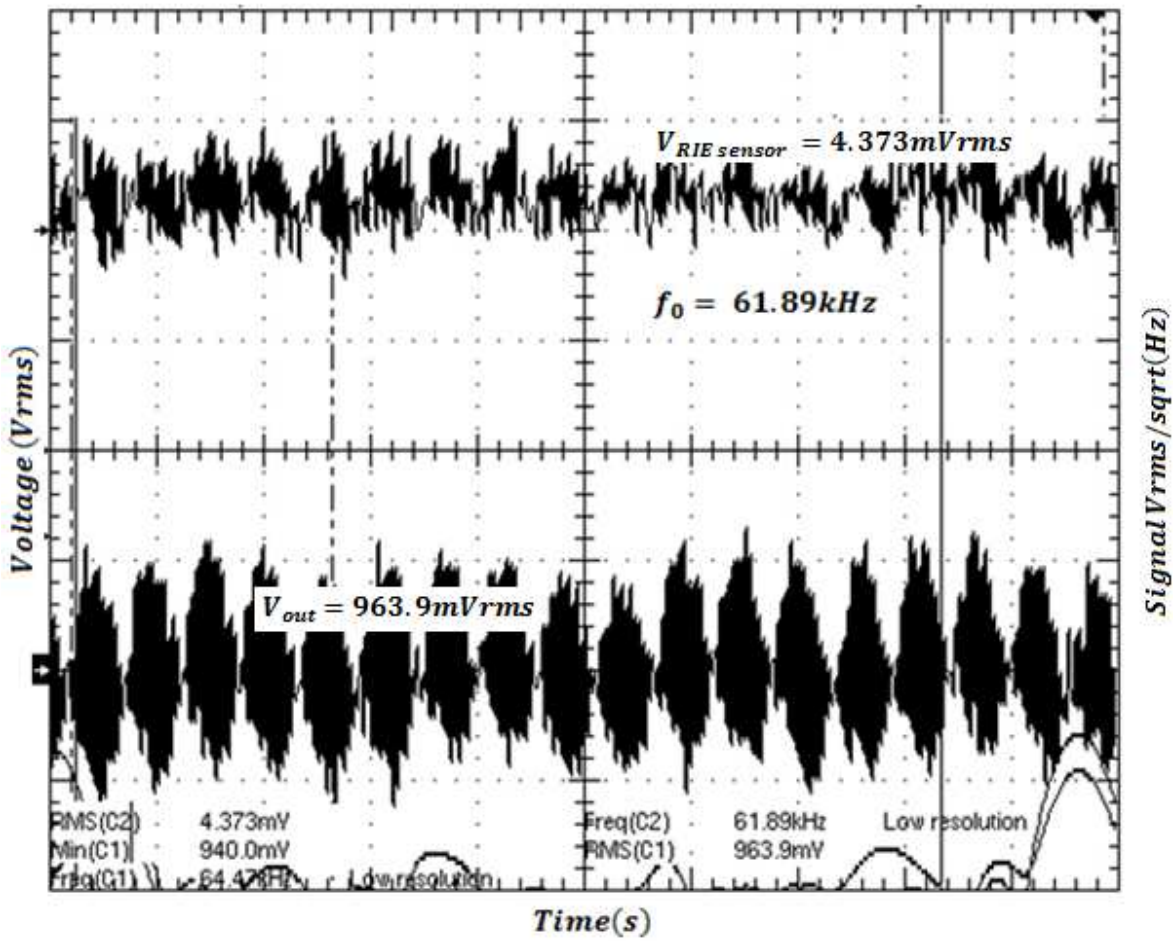

Figure 8.6: Measured waveform taken at 30$mTorr$ during the etchant gas flow. The RIE sensor resonant frequency measured 61.89 kHz. The voltage at the RIE sensor output measured 4.373mVrms and 964mVrms at the output of the charge amplifier circuit

It was observed that the frequency and Q-factor, determined from the output spectrum, also varied during the gas stabilization stage prior to the start of the etching process (Table 8.3). During the etch process, the RF power was applied and the characteristics of the RIE sensor and voltage waveforms immediately changed (Figure 8.7). The impedance of the RIE sensor increased by several orders of magnitude and the measured voltages were initially out of range.

There was also significant noise level in the RIE chamber which further reinforced the necessity for the capacitive sensing charge amplifier interface circuit.

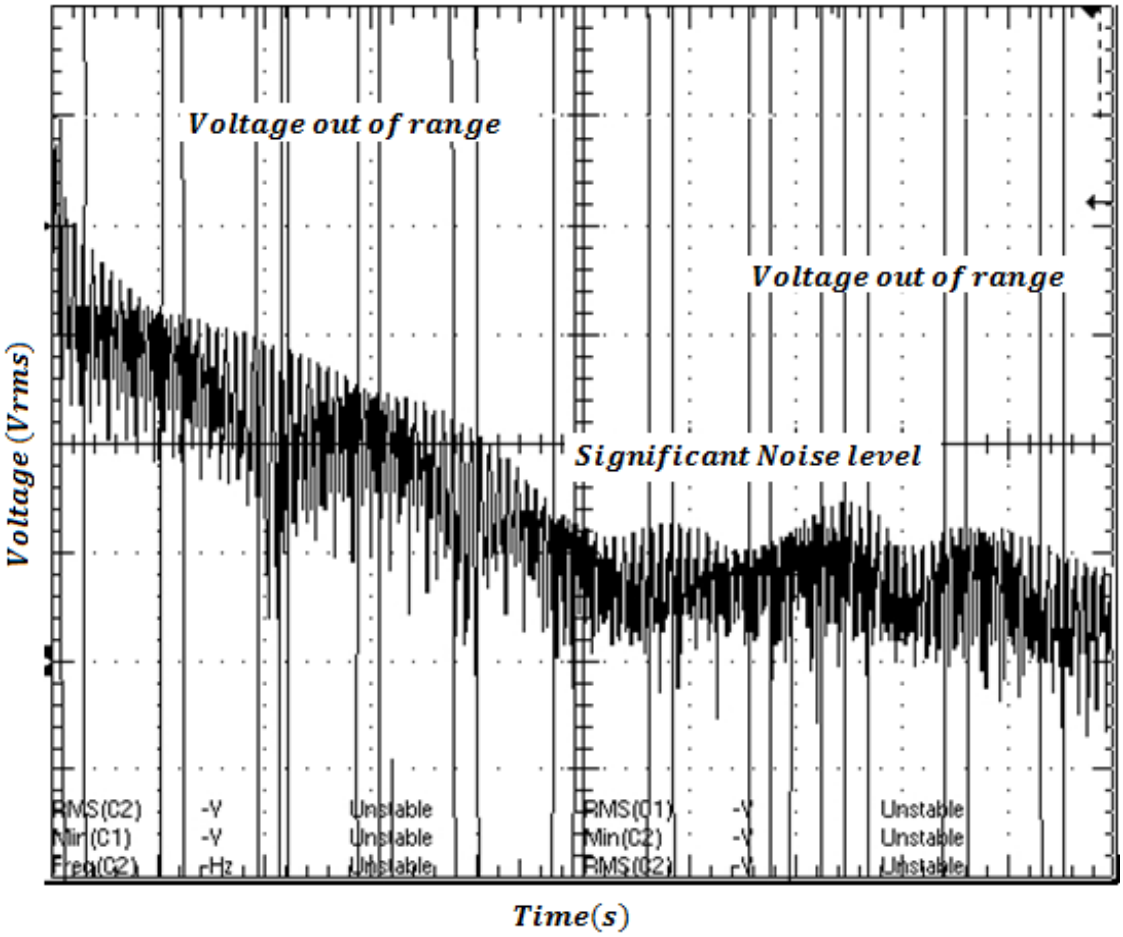

Figure 8.7: Waveforms observed immediately after RF power was applied.

Once the plasma was excited, the etching process started and the waveform in Figure 8.8 was observed. The resonant frequency changed from 61.89 kHz (measured during the gas stabilization stage) to 61.37 kHz (after the plasma was excited). The RIE sensor resonant frequency decreased as the aluminum was etched from the platform.

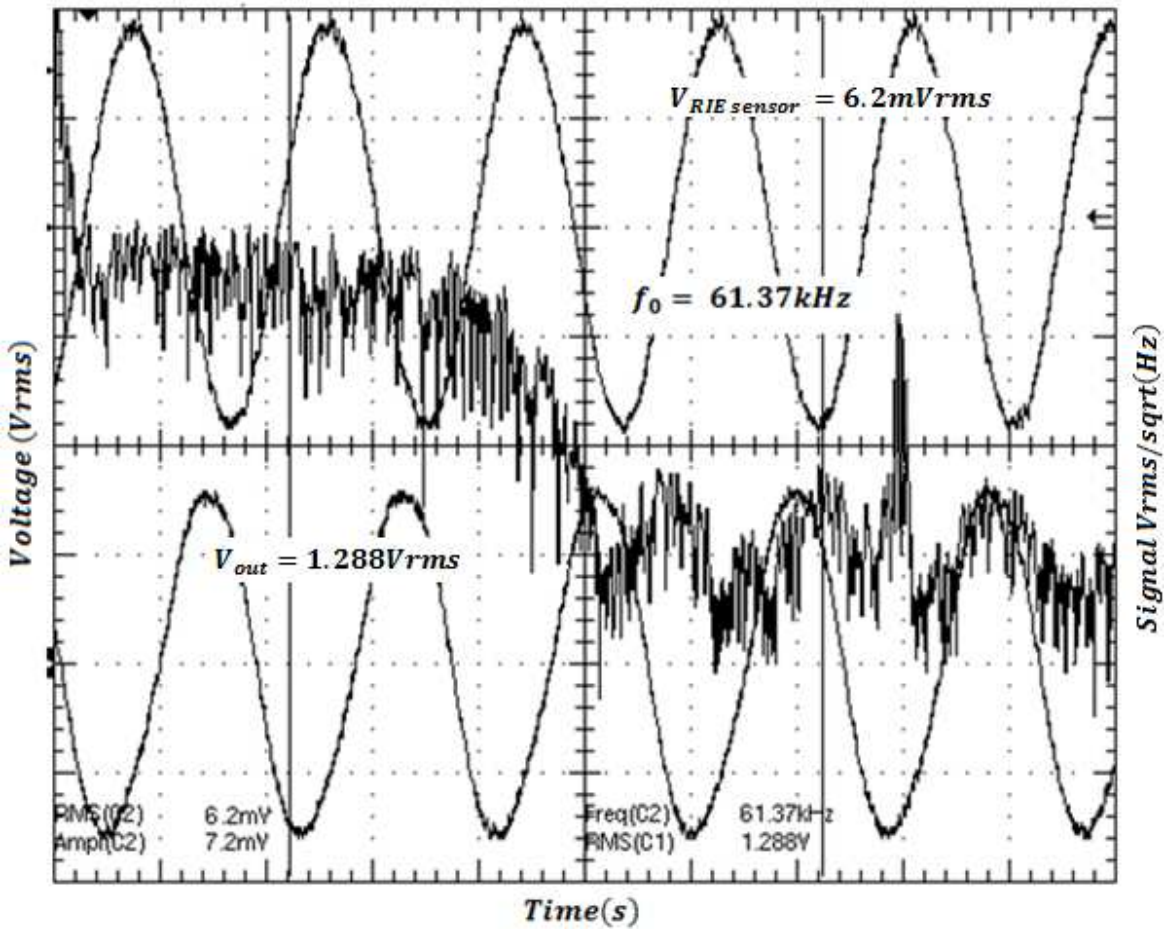

Figure 8.8: Measured waveform for the RIE sensor during the excitation of the plasma. The RIE sensor resonant frequency measured 61.37 kHz. The voltage at the RIE sensor output measured 6.2mVrms and 1.29Vrms at the output of the charge amplifier circuit

When the resonant frequency was 61.37 kHz, the voltages at the RIE sensor output measured 6.2mVrms and 1.29Vrms at the output of the charge amplifier circuit. The maximum measured output voltage at the charge amplifier output was 1.29Vrms. This was equivalent to a maximum integrated RIE sensor charge-amplifier current of 1.29μA and power consumption of 1.67μW.

The resonant frequency and output voltages continued to decrease as the aluminum was etched. Approximately one minute during the etch proccess the RIE sensor resonant frequency measured 57.28 kHz. When the resonant frequency reached 57.28 kHz, the output voltage measured at 910.3mVrms (Figure 8.9).

For the remainder of the (two minutes) etch process time, while the plasma was still excited, the resonant frequency remained constant at 57.28 kHz and output voltage remained unchanged at 910.3mVrms. This implied that the thin layer of aluminum was completely etched from the top of the RIE sensor platform when the resonant frequency measured 57.28 kHz. This was later verified after the RIE sensor was removed from the process chamber.

The resonant frequency and ouptput voltage remained unchanged and at the end of the etch process, the RF power was turned off and the output voltage decreased significantly.

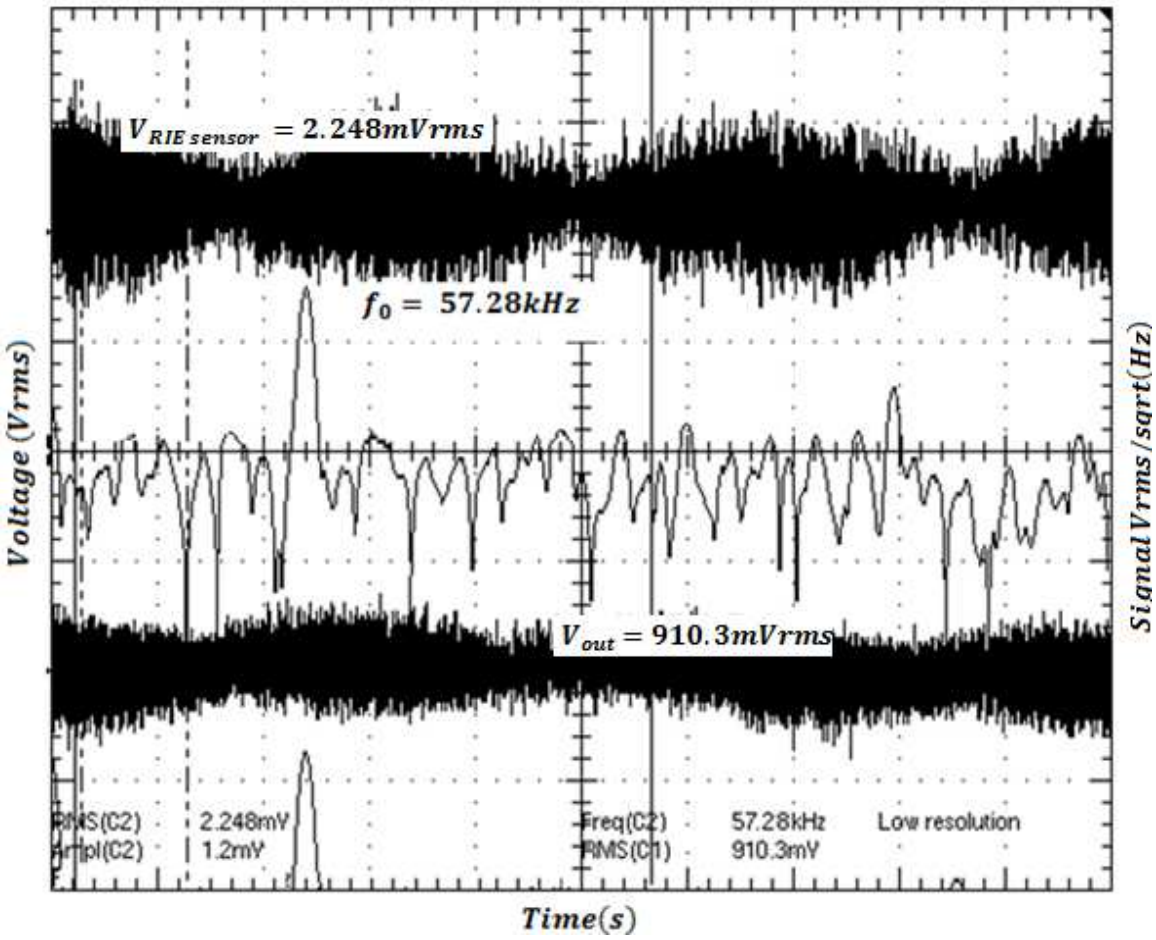

Figure 8.9: RIE sensor resonant frequency measured 57.28 kHz after approximately one minute. The voltages at the RIE sensor electrode and charge amplifer output measured 2.248mVrms and 910mVrms respectively.

8.4 RESULTS AND DISCUSSION

Process control was demonstrated by monitoring the RIE sensor resonance frequency during the excitation of the plasma. The plasma inside the RIE process environment has non-linear impedance characteristics, and the etching process caused the RIE sensor to resonate at frequencies that were different than its unbiased resonant frequency. The RIE sensor resonant frequency measured at different intervals during the etching process decreased as aluminum was etched (Figure 8.10).

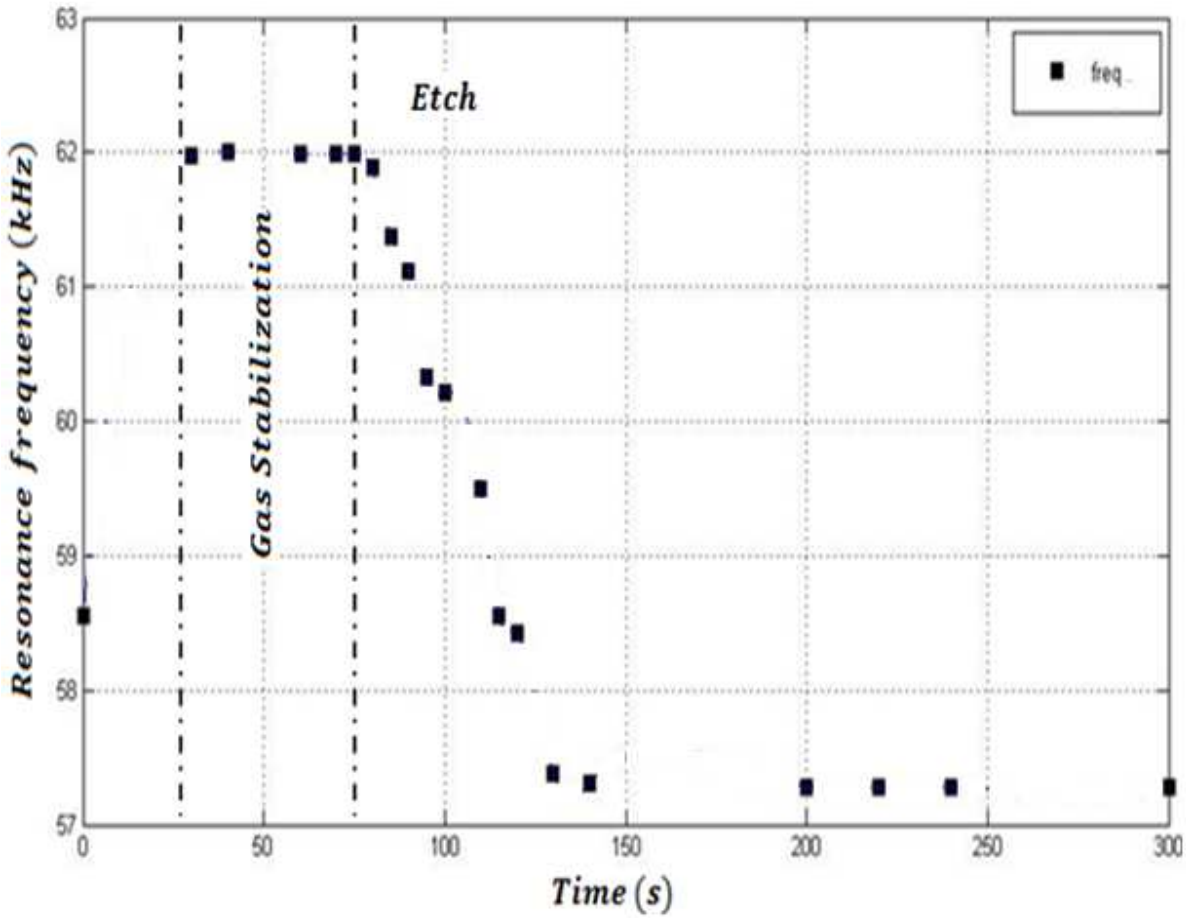

Figure 8.10: RIE sensor resonant frequencies measured at different intervals during the etching process

The RIE plasma environment is noisy so there will be some noise error associated with the RIE sensor resonance frequency measurements. The sensor electronics, however, provided a reasonable immunity to the RIE chamber noise. The aluminum layer is completely etched when the measured resonance frequency remained constant at 57.28 kHz.

It took approximately 65 seconds to etch the aluminun. The etch rate for aluminum was established from the correlation of the resonance frequency and thickness of the aluminum layer. The etch rate was approximately $0.04902\mu m/min$ (Figure 8.11). The RIE sensor utilized frequency shifts as an output and was extremely sensitive. The sensitivity of the integrated RIE sensor was also determined from the resonant frequency and film thickness plots and was $13.62 Hz/\text{Å}$.

It is evident that the etch rate monitoring experimental results confirmed the theoretical prediction of the correlation between film thickness and resonant frequency. The reasons for any deviations from the ideal sensor characteristic resulted from the sensor's frequency transformation principle (physical to electrical), the influence of RIE process conditions, chamber noise and variations in the sensor interface electronics.

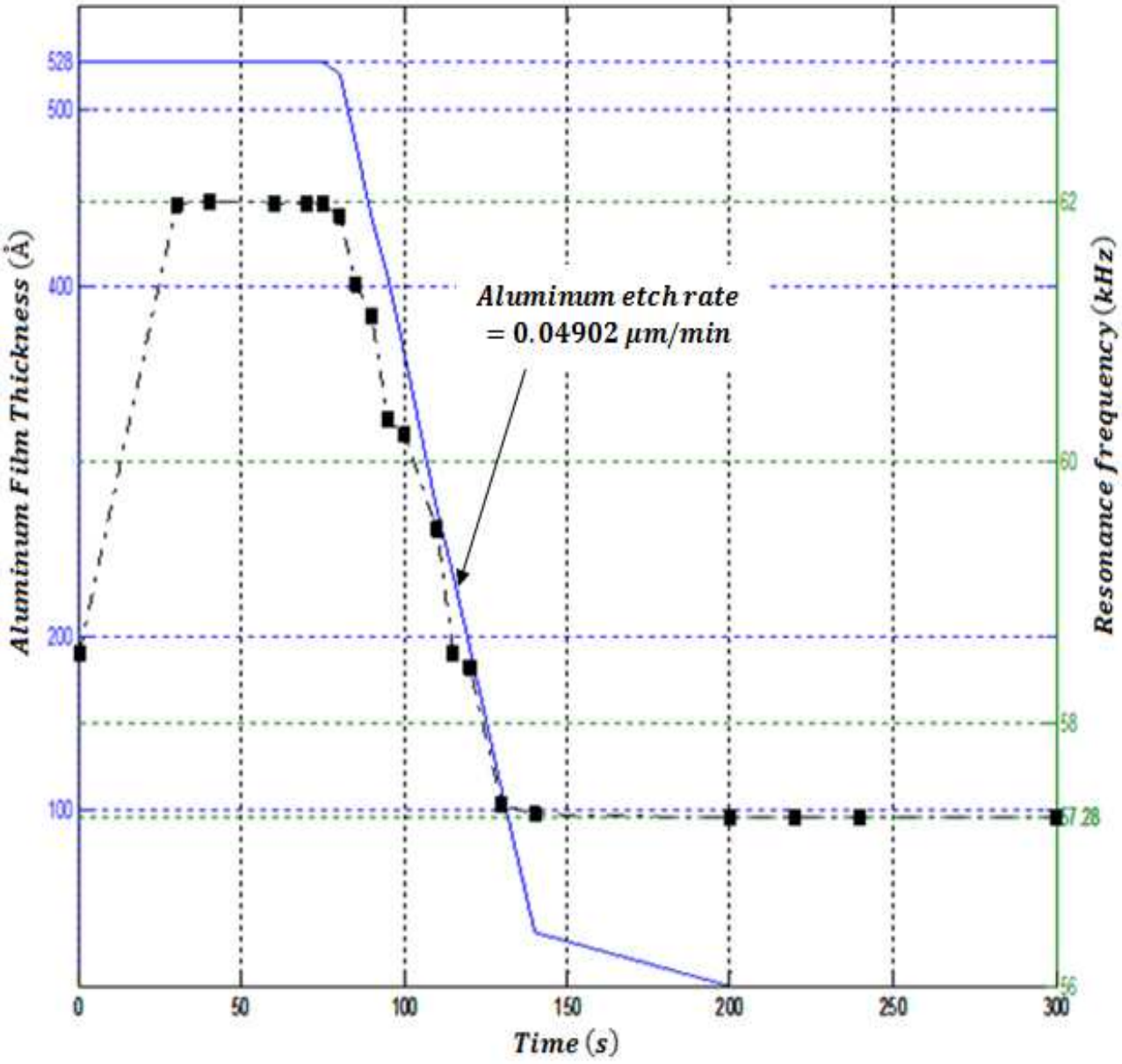

Figure 8.11: RIE sensor resonant frequency and aluminum etch rate plots measured during the excitation of the plasma. Aluminum etch rate is $0.04902 \mu m/min$ and the RIE sensor sensitivity is $13.62 Hz/Å$

The capacitive charge amplifier sensor electronics provided a reasonable immunity to noise and responded more sensitively to variations in the signal amplitude than to variations in the signal frequency (Figure 8.12). The measurement showed the ability of the RIE sensor in combination with the charge amplifier interface electronics to detect the small current changes typical for etch rate monitoring.

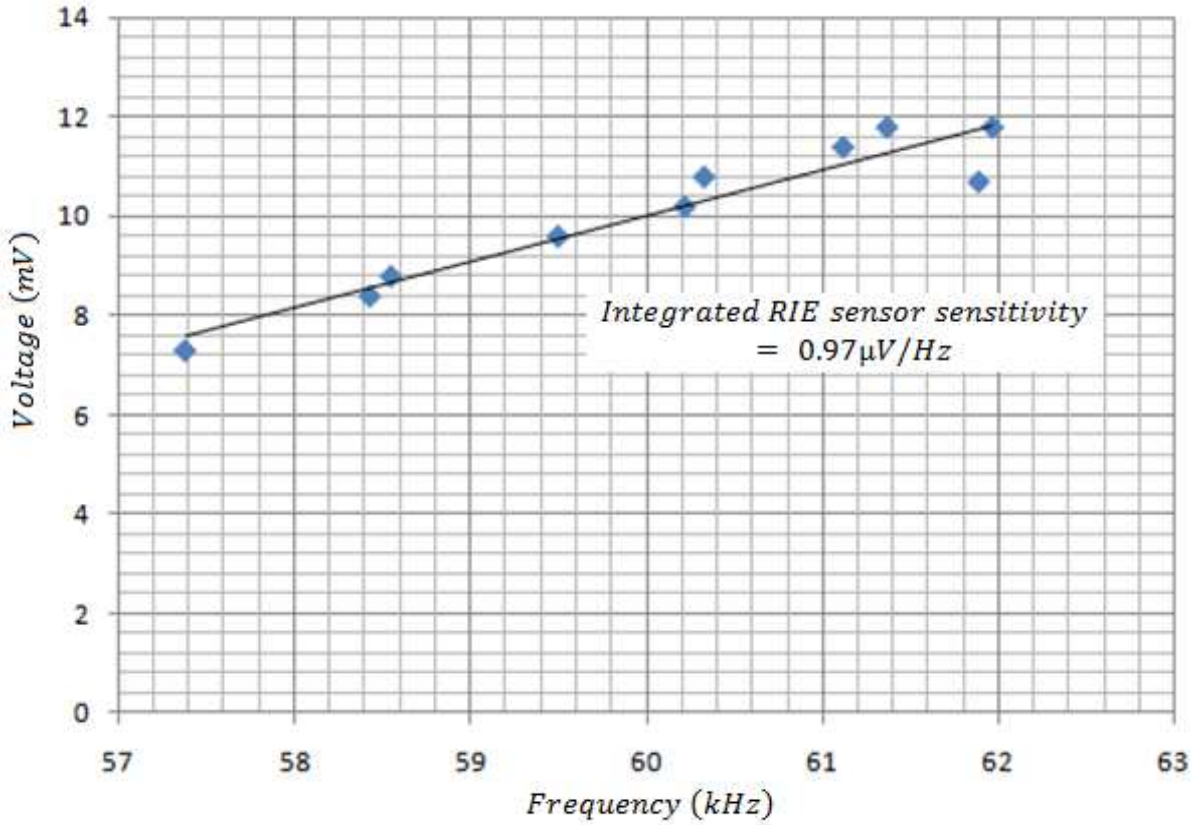

Figure 8.12: The integrated RIE sensor sensitivity to small current changes. The sensitivity to variations in the measured output signal was $0.97\mu V/Hz$.

The performance of the integrated RIE sensor was characterized by its resonance frequency, Q-factor, and 3dB bandwidth. The RIE sensor Q-factor was function of the chamber pressure and was calculated from the curves using the formula, $Q = f_0/\Delta f$. The measured frequency values and Q-factors at vacuum before and after the etch process are summarized in Table 8.3.

Table 8.3: Measured resonant frequencies and Q-factors for the integrated RIE sensor

$Pressure\ (mTorr)$	$f_0\ (kHz)$	$f_1\ (kHz)$	$Qfactor$
10	58.55	123.45	934.1
30	57.28	114.75	762.4

It is clear that the quality factor decreases as the pressure in RIE chamber pressure increases. This behavior is expected since the pressure is inversely proportional to the mechanical quality of the RIE sensor. The output signal of the amplifier yielded the gain factor of the RIE sensor. The output signal of the charge amplifier sensor electronics only depended on the DC offsets and was a linear function of the capacitance change. With respect to the frequency $f =$ 57.28 kHz, a total gain factor A = 405.

The output signal and noise spectrum of the integrated RIE sensor was measured (Figure 8.13). -40dB THD was measured which is dominated by the second harmonic. The source of

the distortion may result from the offset of the amplifier as well as the nonlinearity of the RIE sensor.

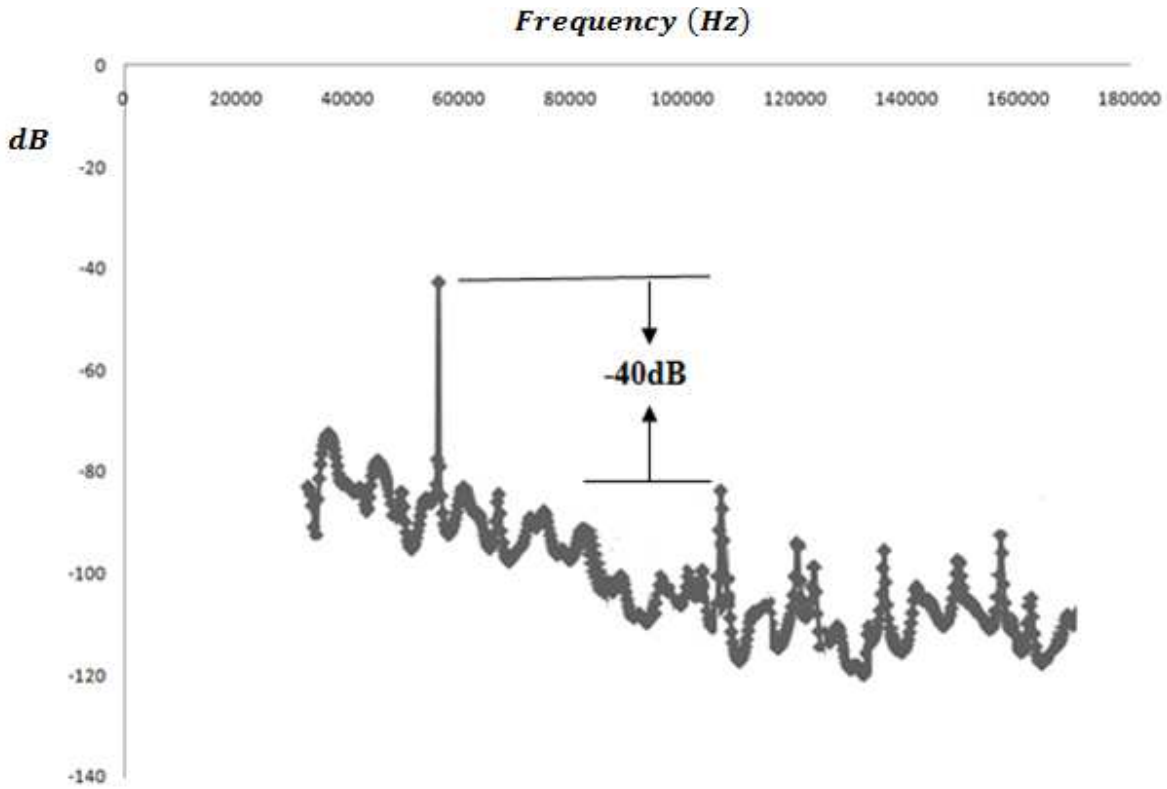

Figure 8.13: The measured output spectrum of the integrated RIE sensor. -40dB THD was observed.

It is evident that using the capacitive feedback charge amplifier to sense capacitance changes achieved high SNR. The power consumption was low ($1.67\mu W$) when the measured output voltage was at a maximum (1.29Vrms). The minimum detectable capacitance variation

ΔC derived from Equation 4.3 (repeated again here as Equation 8.1) and the parameters in Table 8.4 was $29.04aF$.

$$\Delta V_{out} = -\frac{V_{bias}}{C_f} \cdot \Delta C_{sensor} \tag{8.1}$$

Table 8.4: RIE sensor Measurements and Performance

Circuit Parameters	
Power Supply	$3.3V$
Amplifier Power Consumption	$1.67\mu W$
Open Loop Gain	$52dB$
RIE Sensor Bias Voltages	$3.3V$
Feedback capacitance C_f	$800fF$
Measurement Results and Performance	
Aluminum Etch Rate	$490.2\text{Å}/min$
RIE Sensor Sensitivity	$13.62\text{Å}/Hz$
Sensitivity to Voltage Variations	$0.97\mu V/Hz$
Minimum Voltage Variation ΔV	$0.12mV$
Minimum Detectable Capacitance	$29aF$

8.5 SUMMARY

The RIE sensor was operated in the PlasmaTherm SLR RIE system and *in-situ* monitoring and control of the RIE etching process was demonstrated. A feed-through probe was designed for the RIE chamber to access the RIE sensor and interface with external charge amplifier capacitive sensing interface circuit and test equipment. The measurement setup for etch rate monitoring was developed such that the performance of the RIE chamber and RIE sensor would not be compromised during the plasma excitation and extraction of the resonance condition.

The RIE sensor was coated with aluminum and was placed inside of the RIE chamber where the etch rate was monitored by measuring the resonant frequency during the excitation of the plasma. The plasma environment is typically noisy, and it is difficult to extract the small current signal for *in-situ* process control. Because of the very small capacitance changes (fF-range), it was necessary to integrate the RIE sensor with a charge amplifier sensing circuit that transformed the capacitance into utilizable electrical output signals. The interface circuit was highly sensitive and had a large gain.

Due to different etchant gases and plasma process conditions, in combination with the etching forces, different sensor characteristics were expected. The feasibility and robustness of the integrated RIE sensor was demonstrated *in-situ*, and the etch rate for aluminum was established from the correlation of the resonance frequency and thickness of the aluminum layer. The performance and resolution of the integrated RIE sensor was improved. More-consistent results and better sensor performance can be achieved by monitoring and controlling the process parameters, such as etchant gas flow and RF power during the plasma etching.

CHAPTER 9

9.1 CONCLUSION

Semiconductor manufacturers rely on process control methods and analysis of tool sensor outputs to improve yields, increase tool productivity, and reduce manufacturing costs. RIE has emerged as a critical process step in the production of integrated circuits, because it offers high etch directionality, enabling accurate pattern transfer not obtainable with wet etching and its importance cannot be over-emphasized. Volume production often emphasizes etch rates as a route to lowering costs and increasing throughput. Significantly higher production yield can be achieved for applications in which etch rates and feature profile are of greater importance. However, increased etch rates are often accompanied by higher initial capital costs, which must be considered in the context of market size and dynamics. Because there are always trade-offs between performance and capital costs, the required process capability and production volume must be well matched.

The quality of the etch process is principally driven by the condition of the plasma. Changes in the chemistry resulting from variations in the gas-flow rate, the deterioration of chamber parts, pressure deviations, or power or electrode gaps all affect the plasma and therefore, etch characteristics. The behavior of plasma etch tools is difficult to control because small variations in equipment and process setup can have an unpredictable impact on etch quality. Many parameters have a very small margin of deviation (<1%) before yields decline.

Historically, methods to control etch processes have relied on end-of-line metrology and test wafers. While these methods have been used to detect process chamber faults, they are slow

and sometimes unable to provide an unrealistic picture of etch chamber behavior. Determining the root cause of chamber faults has relied on the process engineer's experience and interpretations of tool data, which are not the most efficient ways to detect and remedy tool faults. Given the wealth of data provided by process tools, more-sophisticated methods have been developed, which are known collectively as advanced process control (APC). With APC, engineers can systematically interpret data from many tool sensors using statistical rules that can track tool performance and detect fault conditions in real time. These techniques can be used to analyze data and faults, defined as statistical deviations outside the normal limits of variation. A potential drawback to this method is that the tool parameters in question may not always display a normal distribution, so that such concepts as average and standard deviation can only be approximate. This uncertainty can lead to compromises that broaden fault limits, reducing sensitivity, or that allow statistical outliers to be processed, giving rise to false alarms.

In the environment of fast changing and diverse customer requirements, novel approaches to process monitoring and control have to be found. The focus of the APC efforts is now, more than ever, on a fundamental understanding of etch mechanisms and its implications to process development. Each etch step has to be characterized not only by its etch characteristics, like etch rate, profile, selectivity, and uniformity across wafer, but also by its fundamental properties, such as sidewall layer composition and thickness, chamber wall deposition composition, depth of the etch, and line edge roughness generated by the sequence of process steps. A better understanding of the underlying etch mechanisms allows the process engineer to choose the best points for process optimization for any new structure.

Highly accurate and repeatable, noninvasive *in-situ* plasma etch monitoring and control process sensors are required, and are essential for producing the kinds of yields, product quality,

and throughput necessary for IC manufacturers to remain competitive. Although well-known monitoring techniques have demonstrated distinct performance advantages and market penetration, other lesser-known applications have been successful as well. The monitoring technique presented here demonstrates the capability for real-time, accurate monitoring of the etch rate in the RIE process that can potentially improve process yields and decrease equipment downtime.

9.2 CONTRIBUTIONS OF THE RESEARCH

This thesis described a unique implementation of an integrated micromechanical resonant sensor for *in-situ* monitoring and control of the reactive ion etching process. Resonant sensing at the micromechanical scale allows for the precise detection of shifts in a physical parameter (the resonant frequency), and its principles were studied for both the static and dynamic performance.

1) *Finite Element Analysis*: The design of the RIE sensor was verified with ANSYS. The simulation was important for the practical realization of the RIE sensor and the results of the simulations confirmed the theoretical model. The relationship between the platform height (film thickness) and resonant frequency was established. Optimization of the sensor design results in the best parameters which influenced the fabrication process.

2) *Fabrication Process Improvement*: This RIE monitoring methodology exploits the accuracy of resonant micromechanical structures, whereby shifts in the fundamental resonant frequency measure a physical parameter. A majority of these systems require free-standing mechanical movement and utilize a sacrificial layer process as the key technique to develop and release the

structure on a substrate. A sacrificial layer technique was demonstrated that utilized a low temperature polymer to develop and release the free-standing RIE resonant sensor. The sacrificial layer technique possess the following attributes: (1) the process is simple and reproducible; (2) the coating process is compatible with dry or aqueous etching processes; and (3) the release-stiction problem is alleviated by thermal cure and decomposition of the sacrificial material.

3) RIE Sensor Integration: The integration of sensors with electronic interface circuitry, into more sophisticated instrumentation subsystem, is very important and an increasing trend. The RIE sensor's overall performance is limited because of the nature of the plasma etch environment, thus, the interface circuitry performs an essential role in the complete RIE etch rate monitoring system. Integration with the capacitive charge amplifier circuit allows the RIE sensor to function as a highly sensitive measure of etch rate during the RIE process by suppressing the parasitic capacitances effectively. Additionally, the integrated RIE sensor and charge amplifier interface circuit achieves a large dynamic range, allowing for its application as an *in-situ* etch rate monitor during the RIE process.

4) Etch Rate Monitoring: The etch rate monitoring technique based on the correlation between the RIE sensor's resonant frequency and film thickness changes, during plasma etching have been demonstrated. The resonant sensing technique has the potential to overcome the challenges for RIE, which are inhibited by the inadequacies of the existing process control strategies. The integrated RIE sensor can be used to provide direct, real-time measurements of the actual wafer state during the etch, potentially enabling rapid etch rate measurements in automated production

equipment without opening or contaminating the process chamber, and without the need for special hardware modifications. Beyond that, the possible future development of the integrated RIE sensor has the potential for monitoring and controlling other critical plasma etch applications, such as, high-k dielectric and source-drain etch endpoint detection.

9.3 POTENTIAL INDUSTRY SOLUTIONS

Measurement data obtained with the integrated RIE sensor can enable process engineers to monitor and compare processes and tools to achieve better control of RIE process in real-time. The development of the RIE sensor has important implications on other manufacturing issues. In addition to etch rates to achieve high throughput, other concerns include sidewall smoothness to achieve device performance, process stability and reproducibility, and sensitive endpoint detection in SOI processing.

One of the key challenges for etch engineers today is matching process chambers to achieve consistent performance across the entire toolset. Smaller processing windows make chamber matching difficult, and increasingly higher RF power recipes make it harder to achieve process goals. The integrated RIE sensor measurement technique is immune to RF and ideal for use in any plasma reactor. It also has the ability to sense the resonance shifts and provide data without modification of process recipe or tool settings. With the RIE sensor's highly accurate measurement of plasma etch rates, engineers will have access to much needed and sometimes unavailable data, gaining information on the dynamic response to diverse recipe steps, as well as

chamber-to-chamber variations. The data captured by the integrated RIE sensor can also be used by equipment engineers to qualify tools and ensure chamber health.

Because of the nature of deep silicon etching, the conventional endpoint-detection methods of laser reflectance interferometry and optical emission spectroscopy (OES) lack sufficient sensitivity. To counteract the effects of over etching in SOI processes, a sensitive method of endpoint detection is required to detect the small amounts of oxide exposed during the etch process. With endpoint detection, the SOI finish-etch step can occur as early in the process as possible. The RIE sensor can function as an appropriate etch endpoint-detection device and can accommodate a wide range of aspect ratios.

Achieving the desired degree of smoothness on a vertical profile while maintaining an acceptable etch rate has proved challenging using traditional plasma etch processes. The timing of the steps in each cycle of the etch process is directly correlated to the etch rate and sidewall roughness. The roughness issue can be addressed by including additional gases in the process, such as oxygen or nitrogen, to encourage a more anisotropic etch behavior. Although this approach reduces roughness, it is difficult to control and lowers the etch rate. Additionally, the length of the etch cycle is primarily limited by the relatively slow response of the plasma chamber mass-flow controllers (MFCs). Fast digital MFCs have improved the situation. However, they are still limited in their ability to stabilize gas flows or avoid a flow burst at the start of each cycle, which affects process reproducibility and stability. The sensitive etch rate measurement data from the RIE sensor can potentially monitor and maintain the critical profiles, and other important device characteristics.

The extensive range of feature sizes and aspect ratios during RIE has made profile control a challenging issue. One way of controlling feature profile is to use the RIE sensor in a control

scheme that allows the etch parameters to be changed automatically and smoothly during processing. By adjusting process variables such as pressure, gas flows, and power during etching, the profile can be adjusted to compensate for changes in plasma reactant gas and by-products as the features are etched. Variants of the RIE sensor can potentially be developed and designed specifically for chamber matching, post-PM qualification, trouble-shooting and process development.

9.4 FUTURE WORK

Instruments based on wireless and mid-infrared (IR) laser technology are compatible with most semiconductor processing equipment. They can simultaneously measure multiple processes and perform reliable measurements in hazardous and inaccessible environments. The possible future advances in the RIE sensor development may involve a means to transmit and acquire the resonance frequency and etch rate measurement data wirelessly from within the plasma chamber. The semiconductor industry could find use for such real-time etch rate data, for endpoint detection. Additional correlation for process gas purity monitoring, radical density measurements in the plasma chamber, and emissions monitoring may be discovered. The measurements can be accessed by transmitting directly through the processing chamber or gas lines equipped with IR-transparent windows composed of such materials as sapphire, calcium fluoride, or zinc selenide.

Data acquired from the integrated RIE sensor may be sent to a real-time controller, where software interprets and makes, if necessary, any adjustments to the process. Depending on the range, data can be sent to a central fab server to permit factory-wide access. Users could have

access to the software via a touch screen at the tool. Information available to equipment operators includes the etch rate, whether or not the etch process and plasma chamber is in a fault state, what the probable root cause of a fault is, and a list of wafers affected by the fault. Engineers would have access to more-detailed information on etch process and tool, including analysis and raw sensor data.

Finally, the combination of the RIE sensor, interface electronics and embedded microcontroller into an "instruments on a chip" to do etch rate monitoring and control is viewed as a significant motivation for monolithic integration. There are several reasons for integrating the RIE sensor and electronics on chip. It may improve the RIE sensor's performance, especially in the case of capacitive and resonant sensors parasitic capacitance that can adversely affect the performance. These effects are minimized if the interface circuits and the sensor structure are on the same chip. Another motivation for integration can be the increased reliability from the reduction of interconnects. There can be severe restriction on the RIE sensor design. At present, sensor-electronics integration does not seem to be a significant focus for the semiconductor industry, but trends favor monolithic integration in high-volume applications and in those areas where reliability and/or size are especially critical factors.

BIBLIOGRAPHY

[1]. R. Leachman and D. Hodges, "Benchmarking Semiconductor Manufacturing," IEEE Trans. Semi. Manufac., vol. 9, no 2, May, 1996.

[2]. S. Limanond, J. Si and K. Tsakalis, "Monitoring and Control of Semiconductor Manufacturing Processes," IEEE Control Systems Magazine, vol. 18, no. 6, pp. 46 – 58, Dec., 1998.

[3]. M. Moslehi, R. Chapman, et al., "Single-wafer Integrated Semiconductor Device processing," IEEE Trans. Electron Devices, vol. 39, no. 1, pp. 4 – 32, Jan., 1992.

[4]. J. Hosch, "Process Control Sensor Development for Automation of Single Wafer Processors," Proc. SPIE Advanced Techniques for Integrated Circuit Processing, vol. 1392, pp. 555 – 562, 1990.

[5]. C. Spanos, H. Guo, A. Miller, and J. Levine-Parrill, "Real-Time Statistical Process Control Using Tool Data," IEEE Trans. Semi. Manufac., vol. 5, no. 4, Nov., 1992.

[6]. P. Burggraaf, "Coping with the High Cost of Wafer Fabs," Semiconductor International, March, 1995.

[7]. "International Technology Roadmap for Semiconductors 2006," www.itrs.net/news.html (Accessed April 18, 2008).

[8]. G. Rubloff, "In-Situ Metrology: The Path to Real-Time Advanced Process Control," 2003 Proc. Inter. Conf. Characterization and Metrology for ULSI Technology, March 24-28, 2003, vol. 683, pp. 583 – 591, March, 2003.

[9]. S. Cho, D. Janiak, and G. Rubloff, "In-situ Chemical Sensing in AlGaN/GaN Metal Organic Chemical Vapor Deposition Process for Precision Film Thickness Metrology and Real- time Advanced Process Control ", J. Vac. Sci. Technol. vol. B 23, pp. 2007 – 2013, Sep/Oct., 2005.

[10]. Y. Xu, T. Gougousi, et al., "Thickness Metrology and End Point Control in W-CVD Process from SiH 4/WF 6 Using In-situ Mass Spectrometry," J. Vac. Sci. Technol., vol. B 20, pp. 2351 – 2360, Nov/Dec., 2002.

[11]. S. Cho, W. Rubloff, et al., "Real-time Material Quality Prediction, Fault Detection and Contamination Control in AlGaN/GaN High Electron Mobility Transistor Metalorganic Chemical Vapor Deposition Process Using In-situ Chemical Sensing," J. Vac. Sci. Techn., vol. B 23, pp. 1849 – 1855, Sept/Oct., 2005.

[12]. C. Himmel, T. Kim, A. Krauss, E. Kamen, and G. May, "Real-Time Predictive Control of Semiconductor Manufacturing Processes Using Neural Networks," Proc. 1995 American Control Conf., vol. 2, June, 1995.

[13]. S Wolf, Silicon Processing for the VLSI Era, vol. 2 (Sunset Beach, CA: Lattice Press, 1990), 192–193.

[14]. C. Fiorletta, "Capabilities and Lessons from 10 Years of APC Success," Solid State Technology, vol. 47, no. 2 pp. 67–70, 2004.

[15]. T. Edgar et al., "Automatic Control in Microelectronics Manufacturing: Practices Challenges and Possibilities," Automatica vol. 36, no. 11, pp. 1567–1603, 2000.

[16]. J. Scanlan, M. Hopkins, and K. O'Leary, "Knowledge-Based Process Control for Fault

Detection and Classification," Semi. Manuf., vol. 4, no. 10, pp. 132–136, 2003.
[17]. D. Oh et al., "In Situ Diode Laser Absorption Measurements of Plasma Species in a Gaseous Electronics Conference Reference Cell," J. Vacuum Science Technology, pp. 954–961, 1995.
[18]. N. Maluf and K. Williams, "Introduction to microelectromechanical systems engineering," Artech House Pub., 1998.
[19]. M. Gad-el-Hak, "The MEMS Handbook: MEMS, design and fabrication," CRC Press Pub., 2006.
[20]. M. D. Baker, "In Situ Monitoring of Reactive Ion Etching," Ph.D. dissertation, Georgia Institute of Technology, 1996.
[21]. W. Gelder and V. Hauser, "The Etching of Silicon Nitride in Phosphoric Acid with Silicon Dioxide as a Mask," J. Electro. Society, vol. 114, no. 8, pp. 869–872, 1967.
[22]. DM Knotter and TJJ Denteneer, "Etching Mechanism of Silicon Nitride in HF-Based Solutions," Journal of the Electrochemical Society, vol. 148, no. 3, pp. 43–46, 2001.
[23]. C. Deckert, "Pattern Etching of CVD Si_3N_4/SiO_2 Composites in HF/Glycerol Mixtures," J. Electrochemical Soc., vol. 127, no. 11, pp. 2433–2438, 1980.
[24]. C. Gabriel and A. Ginwalla, E. Yeh, "In Situ Wafer Temperature Measurement during Plasma Etching," Solid State Technology, vol. 42, no. 10 pp. 99–107, 1999.
[25]. H. Shan et al., "Process Kit and Wafer Temperature Effects on Dielectric Etch Rate and Uniformity of Electrostatic Chuck," J. Vacuum Science and Tech., vol. B 14, no. 1 pp. 521–526, 1996.
[26]. 1. Duek et al., "Improving Plasma Etch with Wafer Temperature Readings," Semi. International, vol. 32, no. 7, pp. 208–210, 1993.
[27]. S. Bosch-Charpenay, X. Jiazhan, et al., "Real-time Etch-depth Measurements of MEMS ," J. Microelectromechanical Systems, vol. 11, Issue 2, pp. 111 – 117, Apr., 2002.
[28]. D. Stokes and G. May, "Indirect Adaptive Control of Reactive Ion Etching Using Neural Networks," IEEE Trans. Robotics and Autom., vol. 17, Iss. 5, pp. 650–657, Oct., 2001.
[29]. B. Kim and G. May, "Reactive Ion Etch Modeling Using Neural Networks and Simulated Annealing," IEEE Trans. Comp. Manuf. Tech., vol. 19, Issue 1, pp. 3 – 8, Jan., 1996.
[30]. M. Baker, F. Williams, and G. May, "A Novel In-Situ Monitoring Technique for Reactive Ion Etching Using a Surface Micromachined Sensor," IEEE Trans. Semi. Manufac., vol. 11, no. 2, May, 1998.
[31]. Y. Kuo, "Reactive Ion Etching Technology in Thin-film-transistor Processing," IBM J. Research and Development, vol. 36, no. 1, pp. 69 – 72, 1992.
[32]. J Coburn, "Plasma Etching and Reactive Ion Etching," American Institute of Physics Pub., 1982.
[33]. I. Herman and P. Leong, "Real Time Optical Diagnostics in Laser Etching and Deposition," Proc. Mater. Res. Soc. Symp., vol. 201, 1991.
[34]. H. Fang, C. Su, I. Herman and B. Ben, "Real-Time Monitoring of GAAs(100) Etching by Surface Photoabsorption," Mater. Res. Soc. Symp. Proc., vol. 309, 1996.
[35]. S. Kim, F. Terry et al., "In situ measurements of HCl during plasma etching of poly-silicon using a diode laser absorption sensor", Meas. Sci. Tech., vol. 14, pp. 1662-1670, 2003.
[36]. A. Chambers, R. K. Fitch, and B. S. Halliday, "Basic vacuum technology," CRC Press Pub., 1998.
[37]. P. Dawson, "Quadrupole mass spectrometry and its applications," Springer Pub., 1995

[38]. S. Cho, L. Henn-Lecordier, and Y. Liu, “In-situ Mass Spectrometry in a 10 Torr Chemical Vapor Deposition Process for Film Thickness Metrology and Real-time Advanced Process Control,” J. Vac. Sci. Technol., vol. B 22, pp. 880 – 887, May/Jun., 2004.
[39]. D. Greve, T. Knight, X. Cheng, B. Krogh, and M. Gibson, "Process Control Based on Quadrupole Mass Spectroscopy," J. Vac. Sci. Tech. B, vol. 14, no. 1, Jan., 1996.
[40]. D. White, D. Boning, S. Butler, and G. Barna, "Spatial Characterization of Wafer State Using Principal Component Analysis of Optical Emission Spectra in Plasma Etch," IEEE Trans. Semi. Manufac., vol. 10, no. 1, February, 1997.
[41]. J. Schramm, D. Babic, et al., “Anisotropy Control in the Reactive Ion Etching of InP Using Oxygen/methane/hydrogen/argon,” Sixth Inter. Conf.InP and Related Materials, pp. 383 – 386, Mar., 1994.
[42]. M. Bale and R. Palmer, “Reactive Iion Etching of Piezoelectric $Pb(Zr_xTi_{1-x})O_3$ in a SF_6 Plasma,” J. Vacuum Science Tech., vol. 17, Issue 5, pp. 2467-2469, Sept., 1999.
[43]. C. Cheng, K. Guinn, et al., “In Situ Pulsed laser-Induced Thermal Desorption Measurements of Silicon Chlorine Layer Thickness During Silicon Etching in High Density Plasmas of Cl2 and Cl2/O2 Mixtures,” J. Vac. Sci. Technol., A 12, 1994.
[44]. H. Tang and I. Herman, “Polarization raman Microprobe Analysis of laser Melting and Etching in Silicon,” J. Appl. Phys., vol. 71, 1992.
[45]. R. Muller, “Control of the Reative Ion Etching Process for InP and Related Materials by In Situ Ellipsometry in the Near Infra Red,” Inter. Conf. InP and Related Materials, pp. 211 – 214, Apr., 1990.
[46]. Malay K. Ghosh and K. L. Mittal, “Polyimides: fundamentals and applications,” CRC Press, 1996.
[47]. J. Pope, R. Woodburn, J. Watkins, R. Lachenbruch, and G. Viloria, "Manufacturing Integration of Real-Time Laser Interferometry to Etch Silicon Dioxide Films for Contacts and Vias," Proc. SPIE Conference on Microelec. Processing, vol. 2091, 1993.
[48]. D. Chan, B. Swedek, and M. Birang, “Process control and monitoring with laser interferometry basedendpoint detection in chemical mechanical planarization,” Adv. Semi. Manuf. vol. 23-25, pp. 377 – 384, Sep., 1998.
[49]. www.appliedmaterials.com/products (Accessed April 22, 2008).
[50]. Electronic Device Failure Analysis Society, “Microelectronics failure analysis: desk Reference,” ASM International, 2004.
[51]. S. Bhardwaj and K. Saraswat, “Process monitoring techniques using acoustic waves,” Ultrasonics Symposium, vol.1, pp. 367 – 369, 1990.
[52]. Robert Doering and Yoshio Nishi, “Handbook of semiconductor manufacturing Technology,” CRC Press Pub., 2007.
[53]. M. Veysoglu and C. Cooke, “Acoustic time-domain reflectometry for irregular surface Recognition,” J. Acoust. Soc. Am., vol. 99, Iss. 1, pp. 444-454, Jan. 1996.
[54]. S. Hong and G. May, “Neural-Network-Based Sensor Fusion of Optical Emission and Mass Spectroscopy Data for Real-Time Fault Detection in Reactive Ion Etching,” IEEE Trans. Industrial Electronics, vol. 52, Iss. 4, pp. 1063 – 1072, Aug. 2005.
[55]. M. Baker, C. Himmel and G. May, “Time series modeling of reactive ion etching using neural networks,” IEEE Trans. Semi Manuf., vol. 8, Iss. 1, pp. 62-71, 1995.
[56]. K. Gantz, L. Renaghan and M Agah, “Development of a comprehensive model for RIE-lag-based three-dimensional microchannel fabrication,” J. Micromech. Microeng., vol.

18, 2008.
[57]. N. de Rooij, "Current Status and Future Trends of Si Microsensors," IEEE Spectrum, 1991.
[58]. P. Rai-Choudhury, "Handbook of Micromachining and Microfabrication: Volume 2" IET Pub., 1997.
[59]. R. Johnstone and M. Parameswaran, "An introduction to surface-micromachining," Springer Pub., 2004.
[60]. S. Senturia, " Microsystem Design," Springer Pub., 2005.
[61]. S. Yurish, M. Teresa, and S. Gomes, "Smart sensors and MEMS," Springer Pub., 2004.
[62]. V. K. Varadan, K. Jose, "RF MEMS and their applications," John Wiley and Sons Pub., 2003.
[63]. H. de los Santos, " RF MEMS circuit design for wireless communications," Artech House Pub., 2002.
[64]. K. Iniewski, "Wireless technologies: circuits, systems, and devices," CRC Press Pub., 2007.
[65]. D. Satchell and J. Greenwood, "A Thermally Excited Silicon Accelerometer," Sensors and Actuators, A 17, pp. 241 – 245, 1989.
[66]. C. Lemaire, "Surface Micromachined Sensors for Vehicle and Personal Navigational Systems," IEEE Conf. Intelligent Transportation System, pp. 1068 – 1072, Nov., 1997.
[67]. G. Stemme, "A Balanced Resonant Pressure Sensor," Sensors and Actuators, vol. A 21, pp. 336 – 341, 1989.
[68]. R. Howe and R. Muller, "Resonant Microbridge Vapor Sensor," IEEE Trans. Electron Devices, vol. 33, pp. 499 – 506, 1986.
[69]. F. Blom, S. Bouwstra, and M. Elwenspoek, "Resonating Silicon Beam Force Sensor," Sensors and Actuators, A 17, pp. 513 – 519, 1989.
[70]. S. Bouwstra, R. Legtenberg, H. Tilmans, "Resonating Micro-bridge Mass Flow Sensor," Sensors and Actuators, A 21, pp. 332 – 335, 1990.
[71]. K. Thornton, D. Uttamchandani and B. Culshaw, "A Sensitive Optically Excited Resonator Pressure Sensor," Sensors and Actuators, A 24, pp. 15 – 19, 1990.
[72]. C. Chang, M. Putty, D. Hicks, and R. Howe, "Resonant-bridge Two-axis Microaccelerometer," Sensors and Actuators, A 21-23, pp. 342 – 345, 1990.
[73]. W. Benecke, L. Csepregi, A. Heuberger, K. Kuhl and H. Seidel, "A Frequency-selective Piezoresistive Silicon Vibration Sensor," 3rd Inter. Conf. Solid-State Sensors and Actuators, Technical Digest, pp. 105 – 108, 1995.
[74]. T. Plum, V. Saxena, and R. Jessing, "Design of a MEMS Capacitive Chemical Sensor Based on Polymer Swelling," IEEE Microelec. Electron Devices, April, 2006.
[75]. K. Ekinci, et al., **"**Ultimate limits to inertial mass sensing based upon NEMS," Applied Physics Letters, vol. 84, no. 22, pp. 4469-4471, 2004.
[76]. J. Verd et al., "Design, fabrication and characterization of a sub-microelectromechanical resonator with monolithically integrated CMOS readout circuit." IEEE J. MEMS, vol. 14, no. 3, 2005.
[77]. N. Lavrik et al., "Cantilever transducers as a platform for chemical and biological sensors," Review of Scientific Instr., vol. 75, no. 7, pp. 2229-2253, 2004.
[78]. G. Abadal et al., **"**Electromechanical model of a resonating nano-cantilever based sensor for high resolution and high sensitivity mass detection," Nanotechnology. Vol. 12, pp. 100-104, 2001.

[79]. J. Verd et al., "CMOS circuitry for on-chip read-out of a resonating nanometer-scale cantilever," DCIS´2002 Conf. Proc., pp. 207-212, 2002.
[80]. Baltes et al. "CMOS-MEMS" Wiley-VCH. Nov. 2004.
[81]. X. Jin, I. Ladabaum, L. Degertekin, et al., "Fabrication and characterization of surface micromachined capacitive ultrasonic immersion transducers," IEEE J. Micro. Syst., vol. 8, pp.100-114, 1999.
[82]. M. Haller and B. Khuri-Yakub, "A surface micromachined electrostatic ultrasonic air transducer," IEEE Trans. UFFC, vol. 43, pp. 1-6, 1996.
[83]. S. Soloman, "Sensors Handbook," McGraw-Hill Professional Pub., 1998.
[84]. P. Sheng-Yu, M. Qureshi, A. Basu, P. Hasler, and F. Degertekin, "A Floating-gate Based Low-Power Capacitive Sensing Interface Circuit," IEEE Custom Integr. Circuits, Issue, 10-13 Sept., pp. 257 – 260, 2006.
[85]. P. Hasler and T. Lande, "Overview of Floating-gate Device Circuits and Systems," IEEE Trans.Circuits and Systems II: Analog and Digital Signal Processing, vol.,48, no.1, Jan., 2001.
[86]. P. Hasler, B. Minch, and C. Diorio, "Floating-gate Devices: They Are Not Just For Digital Memories Anymore," Proc. 1999 IEEE Inter. Symp. Circuits and Systems, vol. 2, pp. 388 – 391, 1999.
[87]. P. Hasler, "Continuous-Time Feedback in Floating-Gate MOS Circuits," IEEE Trans. Circuits Systems, vol. 48, no. 1 pp. 56 – 64, Jan. 2001.
[88]. P. Hasler, B. Minch, C. Diorio, and C. Mead , "An Autozeoring Amplifier using Hot-Electron Injection," 1996 IEEE Inter. Symp. Circuits and Systems, vol. 3, pp. 325 – 328, May 1996.
[89]. P. Hasler, B. Minch, and C. Diorio, "An Autozeroing Floating-Gate Amplifier," IEEE Trans. Circuits and Systems, vol. 48, no. 1, pp. 74 – 82, Jan. 2001.
[90]. P. Sheng-Yu, M. Qureshi, A. Basu, P. Hasler, and F. Degertekin, "A Charge-based High-SNR Low-Power Capacitive Sensing Interface Circuit," IEEE Trans. Circ. Syst., vol. 55, pp. 1863–1872, 2008.
[91]. C. Moldovan, F. Babarada, and R. Moldovan, "Determination of Resonance Frequency and Sensitivity of Resonance Microsensors with Electrostatic Excitation and Capacitive Detection," pp. 485-489, 1995.
[92]. S. Psoma and D. Jenkins, "Comparative Assessment of Different Sacrificial Materials for Releasing SU-8 Structures," Adv. Mater. Sci., vol. 10, pp. 149 – 155, 2005.
[93]. Z. Cui and R. Lawes, "A New Sacrificial Process for the Fabrication of Micromechanical Systems," J. Micromech. Microeng., vol. 7, pp. 128 – 130, 1997.
[94]. A. Holmes and S. Saidam, "Sacrificial Layer Process with Laser-Driven Release for Batch Assembly Operations," J. Micromech. Microeng., vol. 7, no. 4, Dec. 1998.
[95]. H. Kazuyuki and T. Yamashita, "Photosensitive Polyimides," Technomic, 1995.
[96]. S. Hall and C. Schuckert, "Single Mask Wafer Overcoat Process Using Photodefinable Polyimide," J. Solid State Tech., pp. 95 – 96, Oct., 1999.
[97]. S. Frederico, C. Hibert, R. Fritschi, et al., "Silicon Sacrificial Layer Dry Etching (SSLDE) for Free-Standing RF MEMS Architectures," Micro Electro Mech. Sys., pp. 570 – 573, Jan., 2003.
[98]. T. Burg and S. Manalis, "Suspended Microchannel Resonators for Biomedical Detection," J. App. Physics Lett., vol. 83, no. 13, pp. 2698 – 2700, Sept., 2003.